AEROSOL COMBUSTION SYNTHESIS OF NANOPOWDERS AND PROCESSING TO FUNCTIONAL THIN FILMS

by

Eongyu Yi

A dissertation submitted in partial fulfillment
of the requirements of the degree of
Doctor of Philosophy
(Materials Science and Engineering)
in the University of Michigan
2017

Doctoral Committee:

Professor Richard M. Laine, Chair
Assistant Professor John T. Heron
Professor John Kieffer
Professor Levi T. Thompson

© Eongyu Yi

2017

Dedication

To my family and friends.

Acknowledgements

I would first like to thank my advisor, Richard M Laine. I would not be where I am now had it not been for his guidance, support, encouragement and patience during my doctoral studies. I would also like to thank Professors John Kieffer, Levi T. Thompson, and John T. Heron for serving on my committee.

I want to thank the Laine group colleagues, including Dr. Nathan J. Taylor, Dr. Joseph Furgal, and Dr. Jae-Hwan Jung for their guidance and fellowship. I would also like to thank the visiting scholars, post-doctoral researchers and undergraduate student researchers including Dr. Yongseok Kim, Dr. Ayako Nakao, Natalia Granados, Kanji Saito, Eitaro Nakatani, Yuki Makanae, Clare Hyde, Catherine Haslam, Sandra Molo and Sahil Dagli for making my research experience fruitful as well as entertaining. I also thank Weimin Wang, Changyup Seo, and Dr. Kai Sun for their help with characterization as well as collaborative work.

I would like to acknowledge the financial support from National Science Foundation, Office of Naval Research, Quallion and University of Michigan (MTRAC, UMEI).

Table of contents

List of Figures

List of Tables

List of Schemes

Abstract

In this dissertation, the advantages of liquid-feed flame spray pyrolysis (LF-FSP) process in producing nanoparticles (NPs) as well as processing the produced NPs to ceramic/polymer nanocomposite films and high density polycrystalline ceramic films are demonstrated. The LF-FSP process aerosolizes alcohol solutions of metalloorganic precursors by O_2 and combusts them at > 1500 °C. The combustion products are rapidly quenched (~10s of ms) to < 400 °C, producing NPs with the same compositions as those of the precursor solutions. The high specific surface areas of NPs enable formulation of ceramic/polymer/interface(phase) ternary nanocomposites in which the interphase can be the determining factor of the final net properties. In ceramic processing, NPs show increased sinterability and provide access to small average grain sizes with fine control of microstructures, compared to when micron sized powders are used. Therefore, synthesis, processing, and characterization of NPs, NP derived nanocomposites and ceramic monoliths are of great interest.

We first compare the LF-FSP to commercial FSP process by producing fumed silica. Combusting spirocyclic alkoxysilanes or $Si(OEt)_4$ by LF-FSP process produced fumed silica very similar to $SiCl_4$ derived products. Given LF-FSP approach does not require the containment constraints of the $SiCl_4$ process and precursors are synthesized from rice hull ash, the reported approach represents a sustainable, green and potentially lower cost alternative.

We then show the versatility of NPs in formulating flexible ceramic/polymer nanocomposites ($BaTiO_3$/epoxy) with superior properties. Volume fractions of the $BaTiO_3$ filler and composite

film thicknesses were controlled to adjust the net dielectric constant and the capacitance. Measured net dielectric constants further deviated from theory, with increasing solids loadings, due to NP agglomeration. Wound nanocomposite capacitors showed ten times higher capacitance compared to the commercial counterpart.

Following series of studies explore the use of flame made NPs in processing Li^+ conducting membranes. Systematic doping studies were conducted in the $LiTi_2(PO_4)_3$ system to modify the lattice constant, conduction channel width, and sintering behavior by introducing Al^{3+} and Si^{4+} dopants. Excess Li_2O content was also adjusted to observe its effect on final microstructures and phase compositions. Improved densification rates were found in $Li_{1.7}Al_{0.3}Ti_{1.7}Si_{0.4}P_{2.6}O_{12}$ composition and thin films (52±1 μm) with conductivities of 0.3-0.5 mS cm^{-1} were achieved.

$Li_{6.25}M_{0.25}La_3Zr_2O_{12}$ (M = Al^{3+}, Ga^{3+}) thin films (25-28 μm) with conductivities of 0.2-1.3 mS cm^{-1} were also successfully processed using flame made NPs, overcoming processing challenges extant, resulting in significantly reduced energy input required for densification. Heating schedules, sintering atmospheres, and types of substrates were controlled to observe their effect on the sintering behavior. Furthermore, green film thicknesses were found to be a crucial variable determining the final microstructures and phase compositions due to the varying Li_2O loss rates with change in thicknesses (surface/volume ratios). Using fully decomposed NP mixtures (Li_2CO_3/off-stoichiometric $La_2Zr_2O_7$), as obtained by LF-FSP, provides an ideal approach to use high surface/reaction energy and liquid phase sintering to drive densification.

Chapter 1

Introduction

Nanoparticles (NPs, <100 nm) often show physical and chemical properties different from their bulk form due to the high fraction of atoms at or near the surface. The high specific surface areas (m^2 g^{-1}) due to the small sizes also result in high reactivity. For example, melting points are depressed by 100s of degrees (e.g. In, Pb, Au),[1,2] magnetic properties change as the tetragonality (c/a ratio) decreases (e.g. $BaTiO_3$, $PbTiO_3$),[3,4] band gaps become size dependent (e.g. CdS, CdSe, CdTe),[5] catalytic activities increase due to higher number of reaction sites per unit volume, and etc.

NP/polymer nanocomposites also show novel/improved properties compared to the conventional micron sized powder filled composites. A number of material properties of ceramic/polymer nanocomposites are often manipulated by adjusting the fractions and the sizes of the fillers, wherein NP filled nanocomposites result in NP/polymer/interphase ternary nanocomposites due to the high NP/polymer interfacial area. In some instances, the interphase can be the dominating factor determining the final properties. Optical, electrical, electrochemical, mechanical, and magnetic properties of nanocomposites are commonly modified for applications ranging from abrasion resistant coatings, wave guides, ion conductors, to capacitors.[6-8]

Using NPs in the ceramic processing to sinter films, tubes, and monoliths, provides optimum control of the final microstructure. The high surface free energy and small initial particle sizes

offer potential to sinter at lower temperatures as well as to access smaller final grain sizes compared to when traditional micron sized powders are used.[9] Improved mechanical properties including higher hardness, mechanical strength, and toughness can be achieved with fully dense small grained ceramic monoliths.[10]

Liquid-feed flame spray pyrolysis (LF-FSP), as discussed below, offers easy access to NPs with fine control of average particle sizes and chemical compositions, providing flexibility to tailor material properties over a range of compositions and sizes. Sol-gel and co-precipitation syntheses are commonly used for producing NPs but are limited by the disparate hydrolysis and precipitation rates leading to lower degree of mixing which often requires calcination to reach target compositions.

Therefore, using LF-FSP synthesized NPs is an ideal starting point to investigate the novel properties of the NPs themselves, or the NP/polymer interfaces. The processing of said powders are also useful in investigating the size effect on the sintering behavior as well as accessing microstructures not easily obtainable when micron sized powder are used.

1.1. Liquid-feed flame spray pyrolysis synthesis of metal oxide nanopowders

Liquid-feed flame spray pyrolysis (LF-FSP), as invented in the Laine group at the University of Michigan, is a single step continuous synthesis method for producing ceramic nanopowders (NPs).[11-19] Metalloorganic precursors, typically metal-carboxylate or metal-atrane compounds, as shown in Figure **1.1**, are dissolved in alcohol, usually EtOH, at 1-10 wt % solids loadings which are then aerosolized into a quartz chamber where they are ignited using methane/oxygen pilot torches in an oxygen rich environment. Initial combustion takes place producing temperatures of > 1500 °C followed by a quenching to 300-500 °C over 1.5 m, equivalent to a 1000 °C quench in

<100 ms, to produce NPs. Powders are collected downstream in rod-in-tube electrostatic precipitators (ESP) operating at 10 kV.

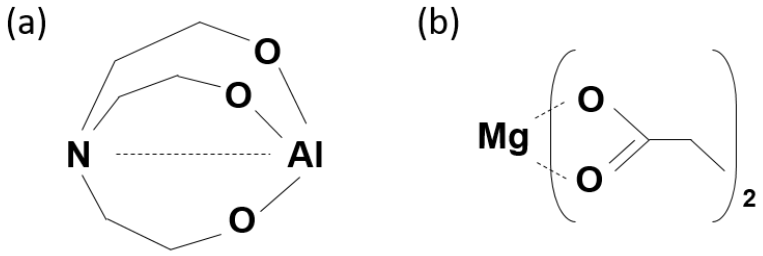

Figure 1.1. Examples of typical precursors used in LF-FSP.
(a) Alumatrane, (b) Magnesium propionate.

Typical NPs produced by LF-FSP have specific surface areas (SSAs) of 30-230 m^2 g^{-1} with corresponding average particle sizes (APSs) of 100-20 nm. Various single- and mixed-metal oxide NPs have been synthesized in the Laine group including but not limited to $Na_{1.67}Al_{10.67}Li_{0.33}O_{17}$, Al_2O_3, TiO_2, Al_2O_3-SiO_2, TiO_2-Al_2O_3, and Y_2O_3, for applications ranging from ion conductors, catalysts, prosthetic implants, to transparent armor.[11-19]

It is also possible to access phases outside the thermodynamic phase diagram as quenching produces metastable, kinetic phases. For example, single phase off-stoichiometric spinels of $MO:3Al_2O_3$ (M = Mg, Ni, Co) are produced rather than a mixture of $MO:Al_2O_3$ and Al_2O_3.[11,12]

One can also synthesize core@shell structured NPs in a single step by selective precursor solution design that includes two oxides with large differences in vaporization temperatures. For example, $ZrO_2@Al_2O_3$ and $Ce_xZr_{1-x}O_2@Al_2O_3$ have been produced.[13,14]

1.1.1. Advantages of LF-FSP compared to commercial FSP

The LF-FSP process overcomes the drawbacks of commercial FSP used to produce Al_2O_3, TiO_2, and SiO_2. These NPs are produced in 1000 tons/yr quantities by combusting MCl_x in H_2/O_2 flames.[20,21]

Fumed silica, in particular, is mass produced by combusting $SiCl_4$ in H_2/O_2 flames for multiple applications ranging from fillers to extend polymers/rubbers, as the insulating core in vacuum insulation panels, as a mild abrasive for polishing, as a thickening agent in food processing, etc.[22-24] Given that both $SiCl_4$ and the combustion byproduct HCl are corrosive, toxic and polluting; this route to fumed silica requires extensive safeguards that may be obviated if an alternate route were found. Silica, including rice hull ash (RHA) can be directly depolymerized using hindered diols to generate distillable spirocyclic alkoxysilanes or $Si(OEt)_4$.[25] In Chapter 3, we use LF-FSP to combust these precursors to produce fumed silica very similar to $SiCl_4$ derived products. The resulting powders are amorphous, necked, <50 nm APSs, with specific surface areas of 140-230 m^2/g. The LF-FSP approach does not require the containment constraints of the $SiCl_4$ process and given that RHA silica source is produced in million ton/yr quantities worldwide, the LF-FSP approach represents a sustainable, green and potentially lower cost alternative. Similarly, for LF-FSP, extensive safeguards are not necessary when producing other oxides as well since no toxic chemical are used nor formed during the process.

Furthermore, fairly uniform combustion rates of the precursors used in the LF-FSP synthesis generally result in atomically mixed NPs, whereas it is difficult to produce mixed-metal oxides with high homogeneity with commercial FSP due to the disparate hydrolysis rates of different MCl_x.

1.2. Ceramic/polymer nanocomposites and polycrystalline ceramic thin films for energy storage applications

The excellent compositional control, narrow particle size distribution, and high SSAs achieved by LF-FSP makes it an ideal starting point for producing NPs for formulating homogeneous, agglomerate free, ceramic/polymer nanocomposite thin films, which are converted to polycrystalline ceramic thin films if sintered.

1.2.1. Ceramic/polymer nanocomposites

Ceramic NPs or nanofibers are commonly introduced to polymeric matrices to enhance the overall electrical, electrochemical, or mechanical properties by combining the superior attributes of each component and/or inducing interfaces that contribute to target properties.[26-32] Types of fillers and polymeric hosts, filler morphologies, sizes, wt. (vol.) fractions, ceramic/polymer interface properties, mixing methods, and etc. are carefully controlled to explore structure-property relationships to achieve optimal properties.

In the energy storage sector, various active and passive ceramic fillers, in which active fillers possess target properties whereas passive fillers don't, at nanoscale are often used. For example, Li^+ conducting $Li_{0.33}La_{0.557}TiO_3$ (σ = 1 mS cm^{-1}) nanofibers or non-conducting Al_2O_3, SiO_2 and TiO_2 NPs at 5-15 wt % have been incorporated into Li^+ conducting polyacrylonitrile-$LiClO_4$ or polyethylene oxide-$LiClO_4$ complexes (σ = 10^{-4} mS cm^{-1}) to result in two to three orders of magnitude increase in Li^+ conductivities (σ = 0.01-0.1 mS cm^{-1}).[27-29] Similarly, three- to ten-fold higher dielectric constants (ε_r = 6-40) were achieved by mixing high dielectric constant (ε_r = 2000-3000) ceramic fillers such as $BaTiO_3$ or $SrTiO_3$ at 20-50 vol % with epoxy resin or polyvinylidene fluoride matrices (ε_r = 2-10).[30-32]

For these nanocomposites, the experimentally measured net properties largely deviate from the approximations based on the rule of mixtures as the ceramic/polymer interaction at the interface becomes significant due to the high SSAs of the nano-fillers. Indeed, the net Li^+ conductivities and dielectric constants obtained in the examples discussed above are notably higher and lower than the approximations based on the rule of mixtures, respectively. Addition of ceramic nano-fillers to Li^+ conducting complexes induces novel conduction mechanisms at the interface and lowers the crystallinity of the polymeric host[27-29] whereas for the nanocomposite capacitors, ionizable species at the interface, e.g. hydroxyl groups on NP surfaces, deteriorate the permittivity.[30,31] The permittivity of the ceramic fillers also drop to 50-200 at nanoscale as discussed in detail in Chapter 4. Hence, nanocomposites are often regarded as ceramic/polymer/interphase ternary composites, and theoretical models estimating the net properties generally include variables such as filler-polymer interaction strength, interphase volume fraction, and etc.[32] Overall, the interface phenomena are clearly the dominating factors in ceramic/polymer nanocomposites, and must be thoroughly investigated to understand the structure-property relationships.

Combining our expertise in NP synthesis and silsesquioxane (SQs)/cage silicate components, we investigate the effect of NP dispersion, ceramic/polymer interface quality, and NP volume fraction on the overall microstructures and net properties, using nano-$BaTiO_3$/epoxy resin nanocomposites as model systems to identify the correlations of each variables, targeting high dielectric constant, flexible nanocomposites to form wound capacitors for pulsed power application capacitor banks.

1.2.1.1. Wound ceramic/polymer nanocomposite capacitors

In pulsed power applications such as medical defibrillators, naval artillery (rail guns), or radars, stored energy must be released instantaneously in a fraction of a second.[33-35] Polymer films are

used widely for these applications owing to their high breakdown voltages and ease of processing.[34] However, the low dielectric constants (2-5) limit the attainable energy densities. Hence, high dielectric constant (2000-3000) ceramics such as $BaTiO_3$ or $SrTiO_3$ in powder form can be mixed in the polymeric matrix to obtain composites that counterbalance their drawbacks, realizing superior energy and power densities compared to the individual components while still offering ease of processing.

In Chapter 4, we mix commercial and LF-FSP processed nano-$BaTiO_3$ with APSs of 50 nm with [glycidyl$SiMe_2OSiO_{1.5}]_8$ (OG, Q cage epoxy) and diaminodiphenylmethane (DDM) at 30, 40 and 50 vol % (60, 70 and 80 wt %) solids loadings to form nanocomposites. Processing of flexible films at 10-13 µm thicknesses on a variety of substrates but especially 40 µm thick aluminum foil is shown. The octafunctional glycidyl silica cage epoxy resin combines very high flexibility needed for rolling with the potential to impart good-to-excellent breakdown voltages and hence higher energy densities.[36-38]

1.2.2. Processing flame made nanopowders to ceramic thin films

Colloidal processing of flame made NPs provide opportunities to combine the advantages of both processing approaches, in particular, in sintering as discussed below.

Briefly, sintering of green bodies to dense polycrystalline monoliths takes place in three stages.[39] In the initial stage, surface diffusion leads to neck formation in the area where particles are in contact. In the intermediate stage, continuous porous network forms along the grain edges as the majority of densification occurs, reaching ~90 % relative densities. In the final stage, continued densification results in closure of the porous network, leaving isolated pores. Further sintering reduces porosity but with concomitant grain growth.

Pore type and size distribution are crucial variables affecting the densification behavior.[40] Agglomerates and aggregates are common inhomogeneities present in the green bodies as local powder packing is different from their surroundings. This leads to density variation and distribution of pore sizes that lower densification rates and increase microstructural flaw sizes during sintering, compared to when green bodies with higher homogeneity are sintered.[41,42] Aggregate pores are particularly difficult to remove as they are surrounded by partially sintered (necked) particles from the beginning.

Provided LF-FSP generally produces agglomerated but unaggregated NPs, colloidal processing of such NPs is an ideal method to prepare highly homogeneous green bodies. Agglomerates are broken down to free flowing NPs during wet ball-milling, and high surface free energies of NPs drive densification at lower temperatures compared to micron sized powders,[43,44] suggesting potential to accomplish lower energy sintering as well as small AGSs, submicron to nano, providing superior mechanical properties such and higher hardness and toughness.

Colloidal processing are conducted in five distinct steps of powder synthesis, suspension formulation, shape forming (e.g. casting), solvent removal, and sintering. It is crucial to adjust processing parameters to achieve high solids loading (50-60 vol %) and homogeneity while maintaining microstructural integrity as any defect present in the green state may result in pin holes or cracks on sintering when producing thin films. Extra step of thermo-compression may be included to increase the compaction rate of the green films and/or to alleviate inhomogeneity prior to sintering.

Work by Yeh et al.[45] clearly demonstrates the importance of preparing green bodies with microstructural homogeneity. In their studies, microstructural evolution of slip cast Al_2O_3 compacts made by well-stabilized and flocculated suspensions are traced from green to sintered

states. When subject to identical sintering condition, the relative density of the compact made from flocculated suspension was 10 % lower, suggesting that initial microstructural inhomogeneity retards densification.

Majority of the sintering studies conducted in the Laine group so far dry compacted LF-FSP synthesized NPs to form green pellets, which microstructural evolution were traced along the sintering steps.[11-19] The novel thin film processing procedure established here can be used to compare the sintering behavior with dry compacted counterparts to elucidate the effects of agglomerates present. Combining the increased driving force from the two attributes, our initial interest was in resolving one of the shared challenges in the realization of all solid state batteries where we survey microstructure-property-processing relationships of selected Li^+ conducting oxides.

1.2.2.1. Oxide Li^+ conductors

Ceramic Li^+ conductors are the key component in the realization of all-solid-state batteries that outperform conventional Li-ion batteries as well as offer inherent safety by removing flammable liquid electrolytes.[46,47]

The advantages of all-solid-state Li batteries were first demonstrated in the 1990s with thin film batteries produced by sequential deposition of $Li/LiPON/LiCoO_2$.[48,49] Low ionic conductivities of LiPON (10^{-3} mS cm^{-1}) limit their applications to thin film batteries to power microelectronic devices. Yet, the glimpses of inherent safety, long cycle life, and high energy densities of thin film all-solid-state batteries have continued to motivate the research community to explore and design suitable materials for bulk solid-state Li batteries.[46,47,50] In terms of electrolytes, identifying materials with ionic conductivities similar to the liquid counterpart has been the main focus for the past several decades. $LiTi_2(PO_4)_3$ (LTP) and $Li_7La_3Zr_2O_{12}$ (LLZO)

doped with selected aliovalent ions have been down-selected as promising candidates in the oxide family, which show optimal electrochemical, microstructural, and mechanical properties when processed to high density monoliths.[51-57] LLZO in particular provides chemical stability to Li metal.[58] A plethora of experimental and computational results regarding both material's crystal chemistry and processing are available and further discussed in Chapters 5-7.[46-60] In contrast, successful processing of dense, thin films (< 50 μm) to promote rapid ion transport has yet to be reported despite the obvious need.

Given ceramics must be sintered to high temperatures to achieve ideal microstructures, often > 1000 °C where Li_2O volatilizes, it has been difficult to replicate the bulk properties in thin film forms at thicknesses < 50 μm, the required form factor for actual application.[61] Hence, successful examples of processing Li^+ conducting membranes are scarce. Furthermore, the production must involve low-cost, easily-scaled processes readily translatable to mass-production.

The improved densification rates obtainable with flame made NPs are crucial when one component volatilizes during high temperature sintering as discussed above. The increased surface/volume ratios of thin films (< 50 μm) compared to pellets (1-2 mm) translates to faster Li_2O loss during sintering, resulting in Li short secondary phases commonly electrochemically inactive.[62,63] Hence, shorter sintering times or lower temperatures achieved by using NPs aid in obtaining single phase, fully dense, polycrystalline ion conducting membranes with optimal properties. Furthermore, small AGSs improve mechanical strength, permitting easier handling compared to large grained thin films, as the crack propagates through a tortuous path, absorbing the energy driving propagation.

In Chapters 5-7, easily scalable, low energy, NP paths to free standing, dense and flexible thin film membranes of both materials, overcoming said challenges, is presented. LF-FSP synthesized

NPs enable colloidal processing, an industry proven low-cost, mass-production method, suggesting facile scalability.[64,65]

1.2.2.1.1. $LiTi_2(PO_4)_3$

Superionic conductivities (> 1 mS cm^{-1}) are typical for $Li_{1.3}Al_{0.3}Ti_{1.7}(PO_4)_3$ made by glass-ceramic processing. However, the thicknesses of sheets made this way (1-2 mm) limit gravimetric/volumetric energy densities and are not applicable to actual devices. In order to process thin films (<50 μm), glass sheets are crushed and high energy ball milled to produce powders with properties acceptable for tape casting, and thereafter sintered.

The motivation for the current work was to synthesize lithium conducting NPs in a single step using liquid-feed flame spray pyrolysis (LF-FSP) thereby eliminating the glass forming, crushing, and ball milling steps.

In Chapter 5, processing of LF-FSP synthesized Al^{3+}/Si^{4+} co-doped $LiTi_2(PO_4)_3$ NPs to pellets and free standing films are demonstrated. It is shown that LF-FSP processing provides non-aggregated NPs that can be used immediately to tape cast, producing thin films of Li^+ conducting membranes when sintered. $Li_{1+x+y}Al_xTi_{2-x}Si_yP_{3-y}O_{12}$ (x = 0.1, 0.3/y = 0.2, 0.4) NPs were prepared by LF-FSP with a primary focus on the effects of $Al_{0.3}/Si_{0.4}$ doping on conductivities. $Li_{1.7}Al_{0.3}Ti_{1.7}Si_{0.4}P_{2.6}O_{12}$ pellets sintered to 93-94 % relative densities and samples with varying excess Li_2O contents all show superionic conductivities of 2-3 mS cm^{-1} at room temperature. Total conductivities range from 2-50 mS cm^{-1} in the temperature span of 25-125 °C. Small grain sizes of 600±200 nm were produced consistently. Initial attempts to make sturdy, free-standing thin films gave films with thicknesses of 52±1 μm on sintering just to 1000°C. Measured conductivities were 0.3-0.5 mS cm^{-1}; attributed to final densities of only ≈ 88 %.

1.2.2.1.2. Cubic-$Li_7La_3Zr_2O_{12}$

Cubic-LLZO offers multiple desirable properties: high ionic conductivities (0.1-1 mS cm^{-1}), Li stability, a wide electrochemical operating window (~ 6 V) and pH stability (7-11.5). Processing dense, thin films matching bulk counterpart properties remains a very difficult target arising from energy and/or equipment intensive sintering, Li volatilization, and contamination from substrates. As a reference, conventional sintering of micron sized c-LLZO powders requires 10-40 h of dwell at temperatures above 1100 °C where Li_2O volatilizes.

Numerous attempts to minimize processing conditions of c-LLZO by introducing sintering aids or using micron- to nano-particles have met with little success. In contrast, hot-pressing provides access to ≈ fully dense pellets with superior bulk ionic conductivities. However, such an approach may be problematic from a commercialization standpoint. Hence, there remains considerable need to first, develop routes to c-LLZO thin films, and second, in a practical and economical way.

In Chapter 6, LF-FSP made NPs are processed to free standing thin films of cubic-$Li_7La_3Zr_2O_{12}$ (c-LLZO), overcoming processing challenges extant, resulting in significantly reduced energy input required for densification as evidenced by 10-40 fold shorter dwell time at sintering temperatures compared to common solid state reaction derived c-LLZO. Through careful control of the processing variable, 10-15 grains thick, dense (94±1 %) c-LLZO thin (< 30 μm), flexible films with high ambient ionic conductivities (0.2±0.03 mS cm^{-1}) are achieved using conventional casting-sintering of flame made NPs.

In Chapter 7, key parameters dictating LLZO densification are elucidated by tracing the compositional and structural change during processing calcined and ball-milled Al^{3+} doped LLZO powders. We find that the powders undergo ion (Li^+/H^+) exchange during room temperature

processing, such that on heating, protonated LLZO lattice collapses and crystallizes to its constituent oxides, leading to reaction driven densification at < 1000 °C, prior to sintering of LLZO grains at higher temperatures. It is shown that small particle sizes and protonation cannot be decoupled, and actually aids densification. We conclude that using fully decomposed NP mixtures, as obtained by LF-FSP, provides an ideal approach to use high surface and reaction energy to drive densification, resulting in pressureless sintering of Ga^{3+} doped LLZO thin films (25 µm) at 1130 °C/0.3 h to ideal microstructures (95±1 % density, 1.2±0.2 µm AGSs) normally accessible only by pressure-assisted sintering. Such films offer both high ionic conductivity (1.3±0.1 mS cm^{-1}) and record low ionic area specific resistance (2 Ω·cm^2).

Reference

1. P. Buffat and J.-P. Borel, *Phys. Rev. A*, 1976, **13**, 2287-2298.

2. C. J. Coombes, *J. Phys. F: Metal Phys.*, 1972, **2**, 441-449.

3. W. L. Zhong, B. Jiang, P. L. Zhang, J. M. Ma, H. M. Cheng, Z. H. Yang, and L. X. Li, *J. Phys.: Condens. Matter*, 1993, **5**, 2619-2624.

4. T. Hoshina, H. Kakemoto, T. Tsurumi, S. Wada and M. Yahima, *J. Appl. Phys.*, 2006, **99**, 054311.

5. A. P. Alivisatos, *Science*, 1996, **271**, 933-937.

6. G. Carotenuto, L. Nicolais, X. Kuang and Z. Zhu, *Appl. Compos. Mater.*, 1995, **2**, 385-393.

7. J. L. H. Chau, Y.-M. Lin, A.-K. Li, W.-F. Su, K.-S. Chang, S. L.-C. Hsu and T.-L. Li, *Mater. Lett.*, 2007, **61**, 2908-2910.

8. Y. Rao, S. Ogitani, P. Kohl and C. P. Wong, *J. Appl. Polym. Sci.*, 2001, **83**, 1084-1090.

9. X.-H. Wang, P.-L. Chen and I.-W. Chem, *J. Am. Ceram. Soc.*, 2006, **89**, 431-437.

10. Z.-H. Chen, J.-T. Li, J.-J. Xu and Z.-G. Hu, *Ceram. Int.*, 2008, **34**, 1709-1712.

11. T. R. Hinklin, J. Azurdia, M. Kim, J. C. Marchal, S. Kumar and R. M. Laine, *Adv. Mater.*, 2008, **20**, 1373-1375.

12. N. J. Taylor, A. J. Pottebaum, V. Uz and R. M. Laine, *J. Am. Ceram. Soc.*, 2014, **97**, 3442-3451.

13. M. Kim and R. M. Laine, *J. Am. Ceram. Soc.*, 2010, **93**, 709-715.

14. M. Kim and R. M. Laine, *J. Am. Chem. Soc.*, 2009, **131**, 9220-9229.

15. A. C. Sutorik, S. S. Neo, D. R. Treadwell and R. M. Laine, *J. Am. Ceram. Soc.*, 1998, **81**, 1477-1486.

16. T. Hinklin, B. Toury, C. Gervais, F. Babonneau, J. J. Gislason, R. W. Morton and R. M. Laine, *Chem. Mater.*, 2004, **16**, 21-30.

17. C. R. Bickmore, K. F. Waldner, R. Baranwal, T. Hinklin, D. R. Treadwell and R. M. Laine, *J. Eur. Ceram. Soc.*, 1998, **18**, 287-297.

18. N. J. Taylor and R. M. Laine, *Adv. Funct. Mater.*, 2014, **24**, 1125-1132.

19. E. Yi, W. Wang, S. Mohanty, J. Kieffer, R. Tamaki and R. M. Laine, *J. Power Sources*, 2014, **269**, 577-588.

20. S. Li, Y. Ren, P. Biswas and S. D. Tse, *Prog. Energy Combust. Sci*., 2016, **55**, 1-59.

21. W. Y. Teoh, R. Amal and L. Madler, *Nanoscale*, 2010, **2**, 1324-1347.

22. K. H. Brodt, and G. C. J. Bart, *J. Therm. Insul. Build. Env.*, 1994, **17**, 238-248.

23. R. Caps and J. Fricke, *Int. J. Thermophys.*, 2000, **21**, 445-452.

24. S. Brunner and H. Simmler, *Vacuum*, 2008, **82**, 700-707.

25. R. M. Laine, J. C. Furgal, P. Doan, D. Pan, V. Popova and X. Zhang, *Angew. Chem. Int. Ed.*, 2015, **128**, 1077-1081.

26. P. P. Vijayan, J. Pionteck, A. Huczko, D. Puglia, J. M. Kenny and S. Thomas, *Compos. Sci. Technol.*, 2014, **102**, 65-73.

27. W. Liu, N. Liu, J. Sun, P.-C. Hsu, Y. Li, H.-W. Lee and Y. Cui, *Nano Lett*., 2015, **15**, 2740-2745.

28. X. Qian, N. Gu, Z. Cheng, X. Yang, E. Wang and S. Dong, *Electrochim. Acta*, 2001, **46**, 1829-1836.

29. B. Scrosati, F. Croce and L. Persi, *J. Electrochem. Soc.*, 2000, **147**, 1718-1721.

30. P. Kim, N. M. Doss, J. P. Tillotson, P. J. Hotchkiss, M.-J. Pan, S. R. Marder, J. Li, J. P. Calame and J. W. Perry, *ACS Nano*, 2009, **3**, 2581-2592.

31. P. Kim, S. C. Jones, P. J. Hotchkiss, J. N. Haddock, B. Kippelen, S. R. Marder and J. W. Perry, *Adv. Mater.*, 2007, **19**, 1001-1005.

32. P. Barber, S. Balasubramanian, Y. Anguchamy, S. Gong, A. Wibowo, H. Gao, H. J. Ploehn and H.-C. Zur Loye, *Materials*, 2009, **2**, 1697-1733.

33. F. W. MacDougall, J. B. Ennis, R. A. Cooper, J. Bates and K. Seal, *Digest of technical papers, 14th IEEE International Pulsed Power Conference*, ed. M. Giesselmann and A. Neuber, IEEE, Dallas, 2003, pp. 513-517.

34. H. Tang and H. A. Sodano, *Nano Lett*., 2013, **13**, 1373-1379.

35. B. Chu, X. Zhou, K. Ren, B. Neese, M. Lin, Q. Wang, F. Bauer and Q. M. Zhang, *Science*, 2006, **5785**, 334-336.

36. K. Takahashi, S. Sulaiman, J. M. Katzenstein, S. Snoblen and R. M. Laine, *Australian J. Chem*., 2006, **59**, 564-570.

37. S. Sulaiman, C. M. Brick, C. M. D. Sana, J. M. Katzenstein, R. M. Laine and R. A. Basheer, *Macromolecules*, 2006, **39**, 5167-5169.

38. J. Choi, S. G. Kim and R. M. Laine, *Macromolecules*, 2004, **37**, 99-109.

39. R. L. Coble, *J. Appl. Phys.*, 1961, **32**, 787-792.

40. F. J. T. Lin, L. C. De Jonghe and M. N. Rahaman, *J. Am. Ceram. Soc.*, 1997, **80**, 2269-2277.

41. A. G. Evans, *J. Am. Ceram. Soc*., 1982, **65**, 497-501.

42. W. H. Rhodes, *J. Am. Ceram. Soc*., 1981, **64**, 19-22.

43. H. Hahn, J. Logas and R. S. Averback, *J. Mater. Res.*, 1990, **5**, 609-614.

44. Y. C. Zhou and M. N. Rahaman, *J. Mater. Res.*, 1993, **8**, 1680-1686.

45. T.-S. Yeh and M. D. Sacks, *Ceramic Trans.*, 1990, **7**, 309-331.

46. Y. Ren, K. Chen, R. Chen, T. Liu, Y. Zhang and C.-W. Nan, *J. Am. Ceram. Soc*., 2015, **98**, 3603-3623.

47. P. Knauth, *Solid State Ionics*, 2009, **180**, 911-916.

48. B. Wang, J. B. Bates, F. X. Hart, B. C. Sales, R. A. Zuhr and J. D. Robertson, *J. Electrochem. Soc.*, 1996, **143**, 3203-3213.

49. N. J. Dudney and B. J. Neudecker, *Curr. Opin. Solid State Mater. Sci*., 1999, **4**, 479-482.

50. J. C. Bachman, S. Muy, A. Grimaud, H.-H. Chang, N. Pour, S. F. Lux, O. Paschos, F. Maglia, S. Lupart, P. Lamp. L. Giordano and Y. Shao-Horn, *Chem. Rev*., 2016, **116**, 140-162.

51. N. Imanishi, S. Hasegawa, T. Zhang, A. Hirano, Y. Takeda and O. Yamamoto, *J. Power Sources*, 2008, **185**, 1392-1397.

52. M. Zhang, Z. Huang, J. Cheng, O. Yamamoto, N. Imanishi, B. Chi, J. Pu and J. Li, *J. Alloys Compd*., 2014, **590**, 147-152.

53. H. Aono, E. Sugimoto, Y. Sadaoka, N. Imanaka and G.-Y. Adachi, *J. Electrochem. Soc*., 1990, **137**, 1023-1027.

54. H. Imagawa, S. Ohta, Y. Kihira and T. Asaoka, *Solid State Ionics*, 2014, **262**, 609-612.

55. Y. Jin and P. J. McGinn, *J. Power Sources*, 2011, **196**, 8683-8687.

56. J. Sakamoto, E. Rangasamy, H. Kim, Y. Kim and J. Wolfenstine, *Nanotechnology*, 2013, **24**, 424005.

57. E. Rangasamy, J. Wolfenstine and J. Sakamoto, *Solid State Ionics*, 2012, **206**, 28-32.

58. M. Kotobuki, K. Kanamura, Y. Sato and T. Yoshida, *J. Power Sources*, 2011, **196**, 7750-7754.

59. K. Meier, T. Laino and A. Curioni, *J. Phys. Chem. C*, 2014, **118**, 6668-6679.

60. R. Jalem, Y. Yamamoto, H. Shiiba, M. Nakayama, H. Munakata, T. Kasuga and K. Kanamura, *Chem. Mater.*, 2013, **25**, 425-430.

61. B. D. McCloskey, *J. Phys. Chem. Lett.*, 2015, **6**, 4581-4588.

62. K. Tadanaga, H. Egawa, A. Hayashi, M. Tatsumisago, J. Mosa, M. Aparicio and A. Duran, *J. Power Sources*, 2015, **273**, 844-847.

63. E. Yi, W. Wang, J. Kieffer and R. M. Laine, *J. Mater. Chem. A.*, 2016, **4**, 12947-12954.

64. J. A. Lewis, *J. Am. Ceram. Soc*., 2000, **83**, 2341-2359.

65. D. Hotza and P. Greil, *Mater. Sci. Eng., A*, 1995, **202**, 206-217.

Chapter 2

Experimental

2.1. Introduction

This chapter summarizes the experimental methods and characterization tools used in this dissertation. Detailed descriptions can be found in each chapter.

2.2. Nanopowder synthesis

Nanopowders were synthesized by the liquid feed-flame spray pyrolysis (LF-FSP) method. Precursor synthesis as well as nanopowder production by LF-FSP method are described briefly below.

2.2.1. Precursor synthesis

Typical precursors used in this dissertation include metal carboxylates and metal-atrane compounds. Metal carboxylates are synthesized by reacting metal oxides, hydroxides, or carbonates with two to three fold excess of a carboxylic acid, typically propionic or isobutyric acid, in N_2 at 120-140 °C for 2-10 h. During the reaction, byproduct water and part of excess acid are distilled off. Clear solutions are obtained when the reaction is complete. On cooling to room temperature, metal carboxylates precipitate out and can be filtered off. Metal-atrane compounds are synthesized by reacting metal alkoxides or hydroxides with triethanolamine at selected molar ratios. Two representative examples are described below.

2.2.1.1. Lanthanum isobutyrate {La[$O_2CCH(CH_3)_2]_3$}

{La[$O_2CCH(CH_3)_2]_3$} was synthesized by reacting lanthanum oxide (130 g, 0.4 mole) with isobutyric acid (530 g, 6 mole) in a 1 L round bottom flask equipped with a still head at 140 °C in N_2. Reaction byproduct water and excess acid are distilled off (50-150 ml) as the reaction proceeds. Once transparent liquid was obtained, heat was removed and lanthanum isobutyrate crystallized on cooling and was filtered out.

2.2.1.2. Alumatrane [$Al(OCH_2CH_2)_3N$]

[{Al[$OCH(CH_3)CH_2CH_3]_3$}, 1700 ml, 6.7 mole] was reacted with [$N(CH_2CH_2OH)_3$, 885 ml, 6.7 mole] at a molar ratio of 1 to 1, in a 4 L vessel under N_2 flow. [$N(CH_2CH_2OH)_3$] was added slowly via addition funnel while the mixture was stirred constantly over a 4 h period. The reaction is exothermic such that [$N(CH_2CH_2OH)_3$] drop rate was controlled to keep the temperature < 80 °C. On completion, transparent, viscous, yellow liquid is obtained.

2.2.2. Nanopowder synthesis

Metalloorganic precursors as discussed above are dissolved in alcohol, usually ethanol, at 1-10 wt. % solids loading. The solution is fed (30-80 ml min^{-1}) into an atomizing nozzle (BETE XA-PR, Greenfield, MA) and aerosolized with oxygen (80 psi, 40 ml min^{-1}) into a quartz chamber where it is ignited with methane/oxygen (40 ml min^{-1}/30 ml min^{-1}) pilot torches. Oxygen shield gas (150 ml min^{-1}) provides oxygen rich environment to minimize carbon residues. Initial combustion takes place producing temperatures of > 1500 °C followed by a quenching step that drops the temperature to 300-500 °C over 1.5 m, equivalent to a 1000 °C quench in <100 ms, to produce nanopowders. Powders are collected downstream in rod-in-tube electrostatic precipitators (ESP) operating at 10 kV. Figure **2.1** shows a schematic of the LF-FSP apparatus.

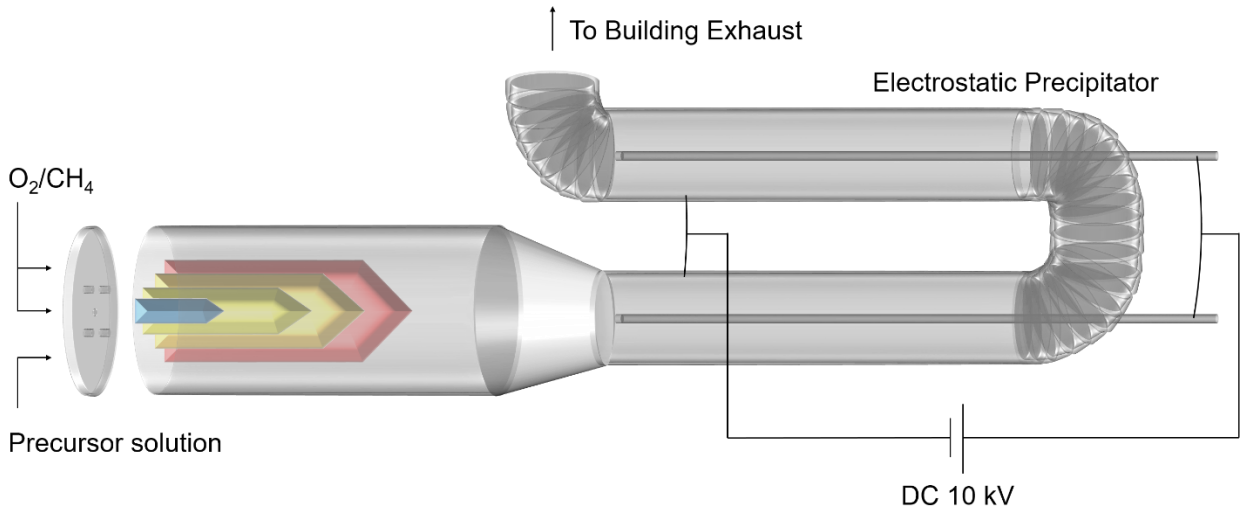

Figure 2.1. Schematic of the LF-FSP apparatus.

2.3. Powder processing

2.3.1. Powder treatment

As-produced nanopowders (10-15 g) were dispersed in ethanol (300-400 ml) with an ultrasonic horn (Vibra cell VC-505, Sonics and Materials, Inc.) at 100 W for 15 min and left for 12-24 h to allow larger particles to settle. Selected dispersants, such as polyacrylic acid (M_w = 2,000), at 1 to 3 wt. % were used as detailed in each chapter. The suspension was decanted and dried. Nanopowders at this stage were used for thin film formulation studies.

For pellet compaction studies, dried nanopowders with dispersants (10-15 g) were, re-dispersed (100W, 15 min) in ethanol (300-400 ml) with addition of 4 wt %, in respect to powder mass, of polyethylene glycol (PEG, M_n = 3,400), and dried again. PEG acts as a binder during pellet compaction. The resulting powders were ground in an alumina mortar and pestle, and subsequently sieved through an 80 μm nylon mesh.

2.3.2. Pellet compaction

The granulated nanopowders (300-500 mg) were pressed in a dual action 14.2 mm WC die, followed by cold isostatic pressing (Autoclave engineers, Erie, PA) at 200 MPa for 30 min.

2.3.3. Thin film casting

Two types of ceramic-polymer composite films were processed in this dissertation based on the end product/application. Generally, LF-FSP synthesized nanopowders were mixed with polymeric additives such as binder, plasticizer, curing agent, and dispersant, in a selected solvent system through a ball-milling (Rotary Tumbler Model B, Tru-Square Metal Products) process using 3.0 mm diameter spherical Al_2O_3 or ZrO_2 beads (Figure **2.2**). One fifth of the container (20 ml) was filled with the milling media.

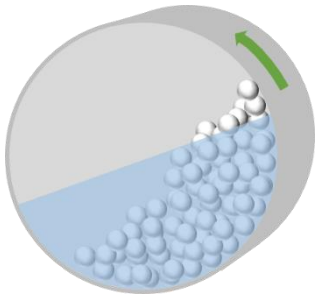

Figure 2.2. Schematic of a ball-milling process.

After 12-36 h of mixing, well dispersed suspensions were cast onto a substrate such as ITO coated glass, Al foil, or Mylar sheet, using a wire wound rod coater (Automatic Film Applicator-1137, Sheen Instrument, Ltd.) (Figure **2.3**). Film thicknesses were controlled either by changing the wound wire thickness (10-30 µm) or by adjusting the gap between the rod and the substrate using a spacer (80-400 µm). The wound wire thicknesses control the depth of the grooves between

the wound wires which determine the final thicknesses of the cast films. Ceramic-polymer nanocomposite films were obtained after solvent evaporation.

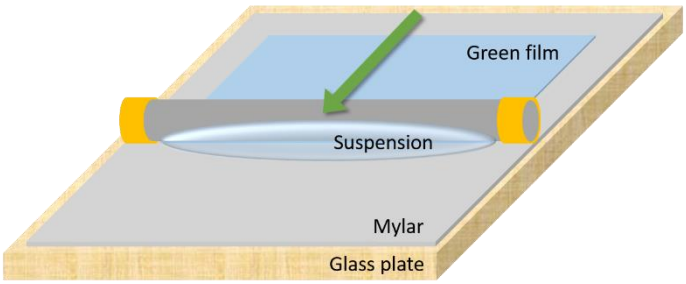

Figure 2.3. Schematic of a casting process.

Tables **2.1** and **2.2** list typical suspension formulations for nanocomposite capacitor fabrication (Chapter 4) and green film formulation (Chapters 5-7). For nanocomposite capacitors, after allowing the solvent to evaporate, the nanocomposite films were cured at 150 °C/6 h under N_2.

Table 2.1. Starting materials and composition for nanocomposite capacitor film casting.

	Role	wt. %
$BaTiO_3$	Filler	26
[(glycidyl)$Me_2SiOSiO_{1.5})_8$]	Binder	11
4,4‘-Diaminodiphenylmethane	Curing agent/Binder	1
Ethanol	Solvent	62

For green film formulations, the dried green films were manually peeled off the Mylar substrate, and cut to 2.5 × 2.5 cm using a razor blade. Green films were uniaxially pressed in between stainless steel dies at 80-100 °C with a pressure of 50-70 Mpa for 5-10 minutes using a bench top press equipped with a heater (Carver, Inc) to improve packing density. Further details can be found in each chapter.

Table 2.2. Starting materials and composition for green film formulation.

	Role	Wt.%
LLZO with 2 wt.% polyacrylic acid	Powder/dispersant	37
Benzyl butyl phthalate	Plasticizer	3
Polyvinyl butyral	Binder	3
Ethanol	Solvent	29
Acetone	Solvent	29

2.4. Binder burnout and sintering

Heat treatments were conducted in a single zone tube furnace (Lindberg/Blue M tube furnace). Films and pellets (14 mm diameter) were subject to binder burnout process prior to sintering by heating them to 500-700 °C for 1-4 h in dry grade synthetic air or extra dry grade O_2 (60 ml min^{-1}). Subsequently, they were sintered to 1000-1200 °C at 5-10 °C min^{-1} under a constant gas (N_2, O_2, or air) flow of 60 ml min^{-1}.

2.5. Characterization

2.5.1. X-ray diffraction (XRD)

XRD measurements were carried out using a Rigaku Rotating Anode Goniometer (Rigaku Denki., LTD.). Scans were made from 10 to 70° 2θ, using a scan rate of 1-5° min^{-1} in 0.01° increments and Cu Kα radiation (1.541 Å) operating at 40 kV and 100 mA. The Jade program 2010 (Version 1.1.5 from Materials Data, Inc.) was used to determine the presence of crystallographic phases, wt. fractions, and to refine lattice constants.

2.5.2. Scanning electron microscopy (SEM)

Micrographs were taken using a FEI NOVA Nanolab system (FEI company) at mode 2. Samples were sputter coated with 5-10 nm gold/palladium using a Technics Hummer IV DC sputtering system (Anatech, Ltd.) to prevent charging.

2.5.3. Transmission electron microscopy (TEM)

High resolution TEM (JEOL 3011) was used to measure the particle sizes and morphologies of as-produced powders. Samples were prepared by dipping a holey carbon grid in a vial containing nanopowder dispersed in ethanol. The specimen was held in a Gatan double tilt goniometer. An operating voltage of 300 kV was used.

2.5.4. Surface area analysis

Specific surface areas (SSAs) were obtained using a Micromeritics ASAP 2020 sorption analyzer. Samples (400 mg) were degassed at 300 °C/5 h. Each analysis was run at −196 °C (77 K) with N_2. The SSAs were determined by the BET multipoint method using ten data points at relative pressures of 0.05−0.30. SSA was converted to average particle sizes (APS) using the equation $APS = 6/(SSA \times \rho)$.

2.5.5. Thermogravimetric analyses - Differential Scanning Calorimetry (TGA-DSC)

Q600 simultaneous TGA/DSC (TA Instruments, Inc.) was used to observe thermal activities of powders and composite films on heating. Samples (15–25 mg) were loaded in alumina pans and ramped to 1000 °C at 10 °C min^{-1} under constant air flow at 60 ml min^{-1}.

2.5.6. Dilatometry

Dilatometry studies were conducting using a Dilatronic II single pushrod dilatometer (Theta Industries). Cylindrical samples (4.7 mm diameter × 7-9 mm height) were prepared by compacting powders using a 4.7 mm stainless steel die. Linear displacement was traced by a linear variable differential transformer (LVDT). Constant heating rate experiments were conducted from room temperature to 1050 °C at a ramp rate of 10 °C min^{-1}.

2.5.7. Fourier transform Infrared spectroscopy (FTIR)

FTIR spectra were taken using a Nicolet 6700 Series FTIR spectrometer (Thermo Fisher Scientific, Inc.). Optical grade, random cuttings of KBr (International Crystal Laboratories) were ground, with 1 wt. % of the sample to be analyzed. The sample chamber was purged with N_2 prior to data acquisition in the range 4000–400 cm^{-1} with a precision of ±4 cm^{-1}.

2.5.8. Inductance, capacitance, and resistance (LCR) measurements

The capacitance and dielectric losses of nanocomposite capacitor films were measured using an HP LCR 4284A meter connected with a 16451B dielectric test fixture. Measurements were made at five frequencies of 0.1, 1, 10, 100 K, and 1 MHz at 1 V_{rms}. ITO served as a bottom electrode by grounding to the LCR meter using a colloidal silver paint (Pelco® Colloidal Silver, Ted Pella, Inc.,). Circular gold/palladium top electrodes (7.4 mm dia.), were deposited onto nanocomposite films by sputter coating using a Technics Hummer IV DC sputtering system. A spring loaded probe was contacted with the top electrode to eliminate physical damage during measurements. For dielectric constant calculations, film thicknesses were determined by SEM fracture surface imaging.

2.5.9. Electrochemical impedance spectroscopy (EIS)

AC impedance data were collected with broadband spectrometer (Novocontrol technologies) in a frequency range of 10 MHz to 0.1 Hz at -35 to 85 °C in increments of 10 °C. Concentric gold electrodes, 3 mm in diameter, were deposited using a SPI sputter coater on both surfaces of the films using a deposition mask. “EIS spectrum analyser” software was used for extracting total resistance. Equivalent circuit consisting of $(R_{total}Q_{total})(Q_{electrode})$ was used. R and Q denote resistance and constant phase element, respectively. SEM fracture surface images were taken to measure sample thicknesses.

Chapter 3

Flame synthesis of fumed silica using sustainable, green sources

3.1. Introduction

Fumed silica is used in multiple applications ranging from fillers to extend polymers/rubbers, as the insulating core in vacuum insulation panels, as a mild abrasive for polishing, as a thickening agent in food production, etc.[1-5] and hence is produced in 1000 ton per year quantities throughout the world.[6-9] Traditionally, much of the fumed silica used today comes from a sequence of reactions that actually starts with silica as illustrated in Scheme **3.1**.

$$SiO_2 + 2C \xrightarrow{1900°C} 2CO + Si_{met}\ (\text{met} = \text{metallurgical grade}, \approx 98\ \%\ \text{purity}) \quad (1)$$

$$Si_{met} + HCl \longrightarrow HSiCl_3\ \text{and/or}\ SiCl_4 \quad (2)$$

$$SiCl_4 + 2H_2/O_2 \xrightarrow{>900°C} SiO_2\ (\text{fumed silica}) + 4HCl \quad (3)$$

Scheme 3.1. Sequence of conventional procedures of fumed silica production.

Thus, any silica source can be reacted with any carbon source in an electric arc furnace at approximately 1900 °C undergoing carbothermal reduction to metallurgical grade silicon or Si_{met} which is then treated with HCl to produce $SiCl_4$ which in turn is combusted in a H_2/O_2 flame to

produce fumed silica plus byproduct HCl. The HCl is recycled with little loss. Nonetheless, because all chlorosilanes and HCl gas are corrosive, toxic and polluting, such production processes require expensive and extensive safeguards adding to the overall cost of the final products. Furthermore, because the fumed silica+HCl products must be cooled in a sealed tube that can be 100 m long, the resulting products are typically highly necked nanoparticles in chain-like manner, which was recently suggested to result in it exhibiting toxic behavior akin to asbestos due to strained three-membered rings, chain-like aggregation, and hydroxyl content, although this observation appears to be controversial.[10-13]

$SiCl_4$ is a byproduct of the manufacture of solar and electronics grade silicon, [Eqs. (4) and (5) in Scheme **3.2**]; therefore, the cost of building or running the plant to produce it is not considered in the cost of producing fumed silica. Consequently, the cost of fumed silica is artificially low.

$$4HSiCl_3 \xrightarrow{\text{disproportionation catalyst}} SiH_4 + 3SiCl_4 \quad (4)$$

$$H_2 + HSiCl_3/SiCl_4 \text{ (or } SiH_4) \xrightarrow{\text{hot wire/rod}} Si_{pv}/Si_{eg} \text{ (6-9 9s purity)} + HCl \quad (5)$$

Scheme 3.2. Sequence of procedures of solar/electronic grade silicon production.[14]

Thus, current commercial fumed silica production involves reduction of SiO_2 to the metal (e.g., Si_{met}), re-oxidation back to $SiCl_4$, and subsequent burning to regenerate SiO_2. This process requires two high-temperature equipment and energy-intensive steps not to mention the safeguards needed to handle $SiCl_4$ and HCl. This approach is unreasonably costly and certainly illogical.

A more reasonable approach would be simply to depolymerize SiO_2 to produce volatile compounds that can be purified by distillation and/or combusted to generate fumed silica directly. However, until recently no such depolymerization chemistry was known. We recently described

the first successful depolymerization of silica to produce volatile compounds, spirocyclic alkoxysilanes, that can be distilled directly from the original silica source as demonstrated by Equations (6) and (7) in Scheme **3.3**, as well as a method of producing $Si(OEt)_4$ or TEOS from related intermediates.[15]

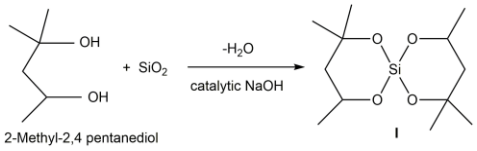

(6)

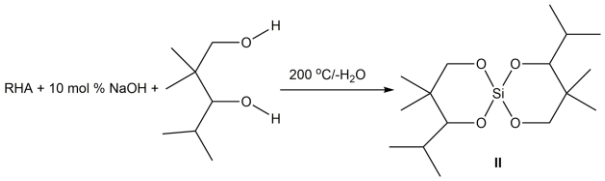

(7)

Scheme 3.3. Depolymerization of silica. Any silica source, for example, RHA can be directly depolymerized using hindered diols to generate distillable spirocyclic alkoxysilanes.

On another note, since immediate shift from $SiCl_4$ to alkoxysilane combustion to produce fumed silica would result in generating an enormous amount of $SiCl_4$ waste, it would be ideal to migrate in accordance with solar/electronic grade silicon production methods switching to metallurgical route which does not require or generate $SiCl_4$ during the process.[14]

We report here the use of liquid-feed flame spray pyrolysis (LF-FSP) to combust the aforementioned precursors to produce fumed silica very similar to $SiCl_4$-derived products. The resulting powders are amorphous, necked, <50 nm average particle sizes, with specific surface areas (SSAs) of 140-230 $m^2 g^{-1}$. The LF-FSP approach does not require the containment constraints of the $SiCl_4$ process and given that the RHA silica source is produced in million ton per year quantities worldwide, the reported approach represents a sustainable, green and potentially lower-cost alternative.

3.2. Experimental

3.2.1. Precursor synthesis and powder production

Spirocyclic alkoxysilanes **I** and TEOS were synthesized using methods described in our recent paper.[15] Methanol, ethanol, and propanol were purchased from Decon Labs (King of Prussia, PA). Aerosil 300 was purchased from Evonik.

Methanol, ethanol or propanol solutions of **I** and TEOS were obtained by dissolving sufficient **I** and TEOS to make a 1, 3 or 5 wt % silica ceramic yield solution. **II** was not tested due to similarity with **I**, to avoid redundancy. The general methods for conducting LF-FSP have been described in previous papers.[16-23]

3.2.2. Characterization

Thermal stabilities of materials under synthetic air were measured on a Q600 simultaneous TGA-DSC Instrument (TA Instruments, Inc., New Castle, DE). Samples (15-25 mg) were placed into alumina pans and then ramped from 25 to 1000 °C (10 °C min^{-1}). The air-flow rate was 60 mL min^{-1}.

XRD analyses were run using a Rigaku rotating anode goniometer (Rigaku Denki, Ltd., Tokyo, Japan). XRD scans were made from 10° to 70° 2θ, using a scan rate of 2° min^{-1} in 0.01° increments and $Cu_{K\alpha}$ radiation (1.541 Å) operating at 40 kV and 100 mA.

SEM micrographs were taken using a FEI NOVA Nanolab system (FEI company, Hillsboro, OR). The powders were sputter coated with gold/palladium using a Technics Hummer IV DC sputtering system (Anatech, Ltd., Alexandria, VA).

High resolution TEM (JEOL 3011, Osaka, Japan) was used to measure the particle sizes and morphologies of as-produced powders. Samples were prepared by dipping a holey carbon grid in

a vial of dispersion with fumed silica powder. The specimen was held in a Gatan double tilt goniometer. An operating voltage of 300 kV was used.

Specific surface areas were obtained using a Micromeritics ASAP 2020 sorption analyzer. Samples (400 mg) were degassed at 400 °C/5 h. Each analysis was run at -196 °C (77 K) with N_2. The SSAs were determined by the BET multipoint method using ten data points at relative pressures of 0.05-0.30.

3.3. Results and Discussion

We now report the direct combustion of compound **I** and TEOS to produce fumed silica using liquid-feed flame spray pyrolysis or LF-FSP. LF-FSP, as practiced at the University of Michigan, aerosolizes metalloorganics dissolved in an alcohol fuel using O_2.[16--23] The aerosol is ignited using methane pilot torches and combustion occurs in a 1 m long quartz chamber *open to air*. The resulting "soot" is quenched to 300-400 °C over a distance of about 1.5 m, *rather than 100 m*, at cooling rates of approximately 1000 °C 100 ms^{-1}. The nanoparticles are then collected downstream in electrostatic precipitators operated at approximately 10 kV DC. Details on LF-FSP processing of nanopowders have been presented elsewhere.[16-23]

The goal of the work reported here is simply to demonstrate the potential utility of direct depolymerization of SiO_2 to volatile spirocyclic alkoxysilanes or TEOS as a green and sustainable alternative to the $SiCl_4$ route to fumed silica.

We have not optimized the LF-FSP process and indeed recognize that it is likely not the optimal synthesis method given that **I** and TEOS are quite volatile and their vapors should combust easily in H_2/O_2 flames without need for a solvent/fuel as used in LF-FSP. However, our extensive familiarity with LF-FSP provides the simplest test available to us for demonstration purposes. This

process has potential to be competitive with the current route at commercial scales given the economic issues noted above. Below, we compare LF-FSP produced fumed silica using **I** and TEOS with Aerosil® fumed silica.

Figure **3.1** and Figure **3.2** provide SEM and TEM images of LF-FSP made fumed silica and Aerosil®. TEM images, especially, reveal aggregation for all samples, typical of flame made silicas.[24,25]

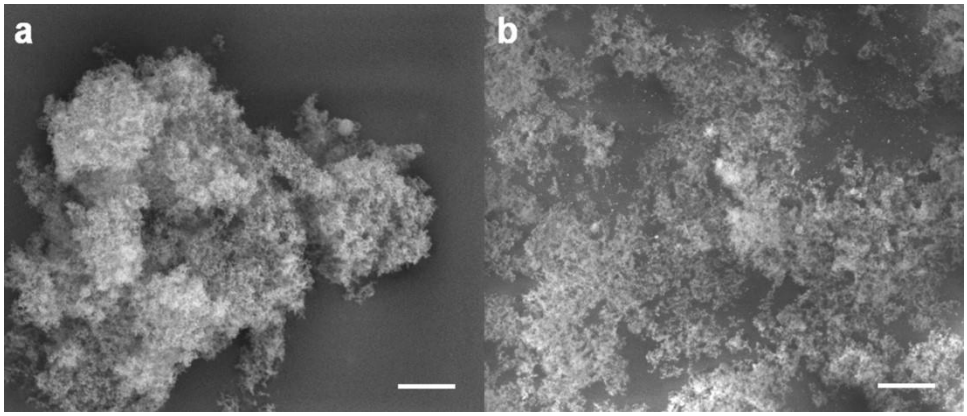

Figure 3.1. SEM images of fumed SiO_2. a. LF-FSP of I, b. commercial Aerosil. Scale bar, 1 µm

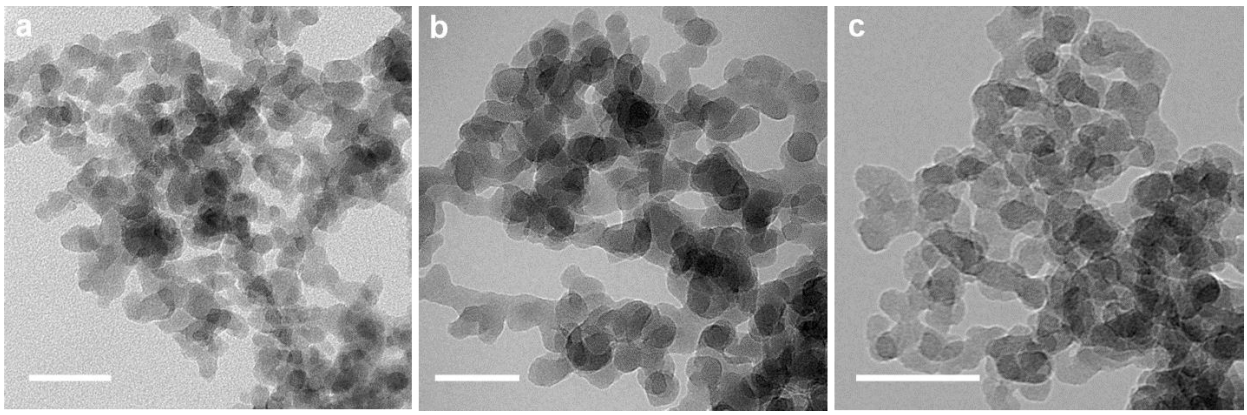

Figure 3.2. TEM images of fumed SiO_2. a. LF-FSP of I, b. LF-FSP of TEOS, c. Aerosil. Scale bar, 50 nm.

Comparative XRDs, FTIRs, TGA and BET data presented in Figure **3.3**, Figure **3.4** and Table **3.1** indicate that the powders are essentially identical from an analytical perspective.

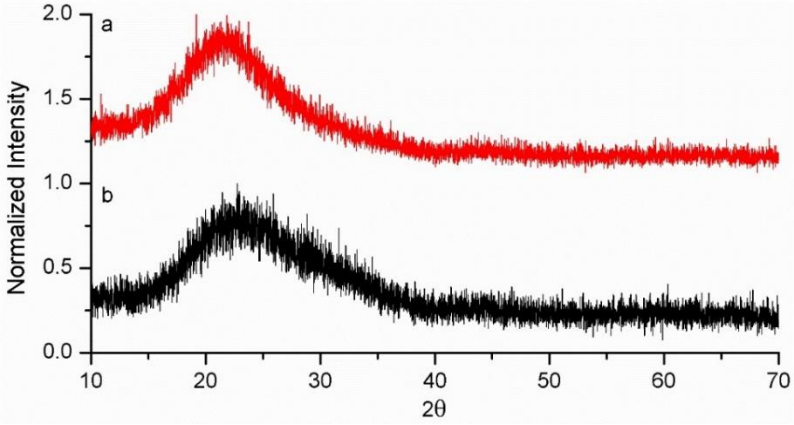

Figure 3.3. XRDs of fumed SiO_2. a. LF-FSP of I, b. Aerosil.

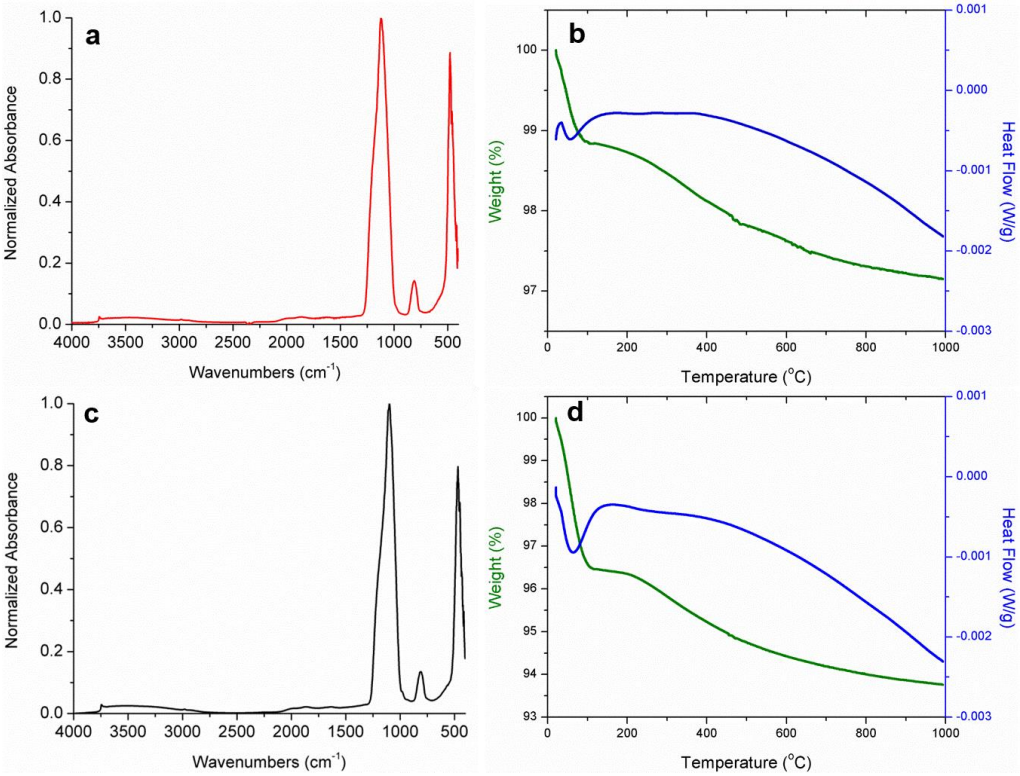

Figure 3.4. FTIR and TGA of fumed SiO_2. **a**.**b**. LF-FSP of **I**, **c.d.** Aerosil.

Table 3.1. SSA of LF-FSP produced silica.

Precursor	Solvent/Fuel	Precursor concentration (wt %)	SSA (m^2 g^{-1})
I	MeOH	1	230
		3	190
	EtOH	1	220
		3	190
		5	140
	PrOH	1	210
TEOS	EtOH	1	230
		3	180
		5	150

Thus, the Figure **3.3** XRDs of as-produced fumed silica made from I and from $SiCl_4$ consist solely of a broad hump centered at 21° 2θ, typical of amorphous materials and as expected.

The Figure **3.4** FTIRs and TGAs look very similar. For TGA, the initial mass loss accompanied by a broad endotherm is ascribed to the removal of physi-sorbed water. The intermediate plateau at >100 °C marks the end of physi-sorbed water loss. The following mass loss is from chemi-sorbed water, surface hydroxyl group, removal.[26] The higher mass loss of Aerosil is merely due to higher surface area, 300 versus 190 m^2 g^{-1}, compared to selected LF-FSP silica.

N_2 adsorption analyses show typical SSAs of 140-230 m^2 g^{-1} for fumed silica derived from **I** and TEOS as shown in Table **3.1** whereas that from $SiCl_4$ runs 50-400 m^2 g^{-1}. However, it should be noted that fumed silica from $SiCl_4$ is produced in a long optimized, mature process. Also, note that lower precursor concentration and lower molecular weight alcohol fuel give higher SSAs for LF-FSP while the former has a stronger effect.

These variables can be adjusted to produce silica at selected SSAs; however, the option of using H_2/O_2 flames likely offers a cleaner and lower cost mechanism to produce "green" fumed silica.

No noticeable difference is observed for fumed silica derived from **I** and TEOS. Hence, combustion of **I** would be preferred for fumed silica production since TEOS involves two synthetic steps whereas **I** is direct depolymerization of SiO_2.[15]

3.4. Conclusions

Based on the above results, we believe that we have developed a green and sustainable route to fumed silica that offers the same if not better properties when compared with fumed silica currently produced from $SiCl_4$. Also, given that there are no hazardous byproducts when combusting compound **I** or TEOS, all the safety mechanisms necessary when combusting $SiCl_4$, including a 100 m long tube, can be avoided, resulting in much lower overall cost, and greatly improving the space efficiency of the combustion apparatus. As a comparison, the LF-FSP apparatus is approximately 3 m long. The only true test will be to determine if it will be cost effective at scale.

A further comment is necessary. The source of the silica is rice hull ash. Rice hulls are frequently burned to produce electricity and RHA coincidentally. The actual energy generated can run to 0.6 GWh per ton.[27] Thus, the energy required to transform RHA into fumed silica is likely to be much less than the output of electrical power on a per kg basis of fumed silica than required to produce fumed silica from $SiCl_4$. Furthermore, the energy gained by burning rice hulls comes from burning carbon. The rice plant has fixed this carbon by photosynthesis using CO_2 as the

source. Consequently, the carbon footprint for the process demonstrated is likely near zero. Likewise the energy output will be more than the energy required to produce the fumed silica.

References

1. V. Dosaj, M. Kroupa and R. Bittar, *Silicon and Silicon Alloys, Chemical and Metallurgical*, *Kirk-Othmer Encyclopedia of Chemical Technology*, Wiley, online, 2005.

2. *Kirk-Othmer Encyclopedia of Chemical Technology*, 5th ed., Vol. 22, Wiley, 2007, pp. 365-547.

3. K. H. Brodt, and G. C. J. Bart, *J. Therm. Insul. Build. Env.*, 1994, **17**, 238-248.

4. R. Caps and J. Fricke, *Int. J. Thermophys.*, 2000, **21**, 445-452.

5. S. Brunner and H. Simmler, *Vacuum*, 2008, **82**, 700-707.

6. G. D. Ulrich, *Chem. Eng. News*, 1984, **62**, 22.

7. A. Gurav, T. Kodas, T. Pluym and Y. Xiong, *Aerosol Sci. Technol*., 1993, **19**, 411-452.

8. T. T. T. Kodas and M. J. Hampden-Smith, *Aerosol Processing Of Materials*, Wiley, New York, 2007.

9. D. E. Rosner, *Ind. Eng. Chem. Res.*, 2005, **44**, 6045-6055.

10. H. Zhang, D. R. Dunphy, X. Jiang, H. Meng, B. Sun, D. Tarn, M. Xue, X. Wang, S. Lin, Z. Ji, R. Li, F. L. Garcia, J. Yang, M. L. Kirk, T. Xia, J. I. Zink, A. Nel and C. J. Brinker, *J. Am. Chem. Soc.*, 2012, **134**, 15790-15804.

11. A. D. Maynard, *Nat. Nanotechnol.*, 2014, **9**, 658-659.

12. L. Petrick, M. Rosenblat, N. Paland and M. Aviram, *Environ. Toxicol,*. **2014**, DOI: 10.1002/tox.22084.

13. T. J. Brunner, P. Wick, P. Manser, P. Spohn, R. N. Grass, L. K. Limbach, A. Bruinink and W. J. Stark, *Environ. Sci. Technol.*, 2006, **40**, 4374-4381.

14. A. F. B. Braga, S. P. Moreira, P. R. Zampieri, J. M. G. Bacchin and P. R. Mei, *Sol. Energy Mater. Sol. Cells*, 2008, **92**, 418-424.

15. R. M. Laine, J. C. Furgal, P. Doan, D. Pan, V. Popova and X. Zhang, *Angew. Chem. Int. Ed.*, 2015, **128**, 1077-1081.

16. R. M. Laine, K. Waldner, C. Bickmore and D. R. Treadwell, US Patent 5,958,361, Sept. 28, 1999.

17. J. Marchal, T. Hinklin, R. Baranwal, T. Johns and R. M. Laine, *Chem. Mater.*, 2004, **16**, 822-831.

18. T. Hinklin, B. Toury, C. Gervais, F. Babonneau, J. J. Gislason, R. W. Morton and R. M. Laine, *Chem. Mater.*, 2004, **16**, 21-30.

19. R. M. Laine, J. Marchal, H. J. Sun and X. Q. Pan, *Adv. Mater.*, 2005, **17**, 830-833.

20. J. A. Azurdia, J. C. Marchal, P. Shea, H. Sun, X. Q. Pan and R. M. Laine, *Chem. Mater.*, 2006, **18**, 731-739.

21. N. J. Taylor and R. M. Laine, *Adv. Funct. Mater.*, 2014, **24**, 1125-1132.

22. E. Yi, J. Furgal, J. Azurdia and R. M. Laine, *J. Mater.Chem. A*, 2014, ***2***, 3766-3775.

23. E. Yi, W. Wang, S. Mohanty, J. Kieffer, R. Tamaki and R. M. Laine, *J. Power Sources*, 2014, **269**, 577-588.

24. X.-J. Wu, Y. Wang, W. Yang, B.-H. Xie, M.-B. Yang and W. Dan, *Soft Matter* 2012, **8**, 10457-10463.

25. A. J. Hurd and W. L. Flower, *J. Colloid Interface Sci*., 1988, **122**, 178-192.

26. R. Mueller, H. K. Kammler, K. Wegner, and S. E. Pratsinis, *Langmuir*, 2003, **19**, 160-165.

27. S. M. Shafie, T. M. I. Mahlia, H. H. Masjuki and A. Andriyana, *Renewable Sustainable Energy Rev.*, 2011, **15**, 4370-4377.

Chapter 4

Processing $BaTiO_3$/epoxy nanocomposite wound capacitors

4.1. Introduction

Capacitors play a key role in storing and controlling electrical energy in electronic components and electric power systems.[1,2] In particular, for pulsed power applications such as medical defibrillators, naval artillery (rail guns), radar, or surgical lasers, accumulated energy has to be delivered instantaneously in a fraction of a second.[3-5]

The recent successful commercialization of supercapacitors might suggest that they would find application in pulsed power production; however, to date their energy outputs per unit time do not yet meet the needs of such applications whereas electrostatic capacitors offer rapid discharge times of μs to ms and high power densities of over 10 KW kg^{-1}.[6] Traditional electrostatic capacitors store electrical energy as charge within a concentrated electric field between two conductive electrodes separated by a dielectric material. In contrast, supercapacitors store charge in electric double layers or in faradic reactions. They offer high energy densities of 1-10 Wh Kg^{-1} but exhibit discharge times of only 1-30 s which can be directly ascribed to ion mass transport and/or redox reaction rate limitations resulting in low power densities of 1-2 KW kg^{-1}.[6,7] Consequently there remains a critical need for new, higher performance electrostatic capacitors for pulsed power applications.

The continuing demand for ever increasing performance levels mandates the development of

capacitor systems that offer superior properties simply on a unit volume basis. These demands coincide with miniaturization trends in every aspect of electronic device manufacture. The higher the energy density, the smaller and lighter a capacitor can be which may also result in lowering the cost involved. Higher energy densities can be obtained when permittivity and/or breakdown voltages are increased, as evidenced by relation between aforementioned variables, $U_{max} = CV_B^2/2v$. $U_{max,}$ C, V_B, and v corresponds to maximum energy density, capacitance, breakdown voltage, and volume, respectively.

Polymer films are widely used for pulsed power applications owing to their high breakdown voltages and ease of processing.[2] However, the dielectric constants are of the order of 2-5, limiting their practical energy densities. For example, biaxially oriented polypropylene (BOPP), commonly used for commercial capacitors, offers energy densities of 1.2 J cc^{-1} arising from a dielectric constant of 2.2.[8] At the other extreme, ceramic dielectrics such as $BaTiO_3$ (BTO) or $SrTiO_3$ (STO) have permittivities of several thousand but have low breakdown voltages.[2] Combinations of the two have been pursued to obtain composites that counterbalance their drawbacks, (although the strengths of each are compromised as well) realizing superior energy and power densities compared to the individual components. The permittivity of composites increases in direct relation to the vol % of ceramic filler but comes at the price of diminishing breakdown voltages. Thus, a range of vol % should be investigated for a given system to identify at what vol % maximum energy densities are obtained. An additional benefit offered by composites is that wet processing is possible for making final forms, greatly reducing costs compared to ceramic dielectrics, as sintering at high temperatures is not needed.

Polyvinylidene fluoride (PVDF) and its copolymers have been widely investigated as a host polymer for composite dielectrics.[2,4,9] PVDF has a dielectric constant of 12,[8] resulting in

ceramic/polymer composites with higher net permittivities and energy densities. For example, Kim et al.[9] have demonstrated a composite of nano-BTO filler and PVDF copolymer matrix with a relative permittivity of 37 and a maximum energy density of 6.1 J cc^{-1} at 50 vol % BTO loading. Although the composite of ceramic filler and PVDF or its copolymer matrix seems to be an answer to next generation of commercial capacitors, realization of practical systems is limited by their cost, non-linearity of capacitance with voltage, poor adhesion, and loss of flexibility at high solids loadings.[4,8,10]

For actual application, wound forms are most desirable due to compactness and ease of processing. Layers are stacked in the order of metal/dielectric/metal/dielectric and rolled around a mandrel. When complete, the bottom metal layer is in contact with the top dielectric layer, resulting in an effective circuit equivalent to two parallel plate capacitors connected in parallel. With a reduction of footprint area and resulting in extra capacitor set when rolled, capacitance per footprint area increases dramatically compared to its unwound counterpart, with the effect being more pronounced as the rolling length increases. Accordingly, most capacitor banks, either stationary or mobile, adopt wound capacitor configurations. To this end, the U.S. Navy and Air Force have supported significant programs to develop superior wound capacitors.[11-24]

Although the literature to date does describe processing of ceramic/polymer nanocomposite films for capacitor applications, there are yet no reports that demonstrate such films can be sufficiently flexible to be rolled especially with high vol % of nanoceramic particles. The potential to realize wound capacitors with much higher energy densities is likely to greatly change energy storage device manufacture, at least in some high-end applications.

While this is an exciting prospect, there are actually multiple challenges to developing such a flexible system: (1) the loading of the ceramic must be optimized to ensure the highest energy

density; (2) the ceramic filler must be evenly dispersed in the polymer even after curing; (3) the ceramic/polymer composite must remain flexible on curing even at high loadings of ceramic powder, and the resulting polymer film must be stable (greatly resist fatigue) to cycling between charge and discharge states. Further issues involve the effects of particle size on the dielectric constant of the filler and of course on flexibility and therefore the design/processing of the dielectric layer.

Both, miniaturization of power systems and inverse proportionality between dielectric layer thickness and capacitance mandate reduction of dielectric thickness. If a composite film were to be of the order of 2-5 μm in thickness, it is impossible to use ceramic powders that are micron sized. Indeed, even submicron size particles, e.g. 500 nm average particle sizes (APSs) dispersed in a polymer matrix would not be amenable to processing to uniform, flexible thin films, especially with smooth surfaces. However, one can envision the use of nanopowders of the order of 30-40 nm with the implication that surface roughness would be < 30 nm assuming that the polymer matrix would fill interstices between particles.

The ceramic filler used in current study is BTO, which has long been investigated and used as an electro-ceramic material due to its inherent dipole moment in the tetragonal phase. Some examples include multilayer ceramic capacitors,[25] holographic memory,[26] and gate dielectrics.[27] As mentioned earlier, miniaturization drives efforts to examine/improve the dielectric properties of sub 100 nm BTO particles or grains.[9,28,29] There is a continuing controversy about the critical size at which BTO becomes cubic at room temperature with the concomitant loss of dielectric properties.[30,31]

We have developed a method of producing a wide variety of single and mixed-metal oxide nanopowders using liquid feed flame spray pyrolysis or LF-FSP. Furthermore, we have also

explored the development of nanocomposite systems and their processing into a wide variety of monolithic and thin film structures focusing on silsesquioxane (SQs) and cage silicate components, especially epoxy resin nanocomposites.[32-35] This paper combines expertise in both areas to explore the use of cage silicate epoxy nanocomposite resins as matrices for nano-BTO. We note that a number of other groups have successfully produced nanocomposite films of BTO.[9,36-38] however, studies on flexibility or processing rolled capacitors have not been reported.

For these types of applications, sub 100 nm particles offer optimal potential for making flexible BTO/polymer nanocomposite films with high loadings while still maintaining flexibility especially using the OG system, which imparts flexibility even in crosslinked epoxy resins.[39] The BTO nanopowders used here appear to be primarily tetragonal despite literature suggestions to the contrary. Past studies on BTO relied heavily on the c/a ratios of the resultant powders to ascertain the degree of tetragonality. Unfortunately, in nano-sized powders, the XRD patterns broaden significantly such that accurate measurement of c/a ratios is not possible. We find that it is simply better to measure the dielectric constants of the powders to determine their properties.

Furthermore, several studies discuss the fact that addition of SQs at 1-10 wt %, either in liquid or solid form, to epoxy resin results in increases in dielectric breakdown voltages, reaching >60 kV mm^{-1}.[40,41] Higher breakdown voltages lead to higher maximum energy densities as discussed above.

BTO/epoxy composite films are generally used as embedded planar capacitors due to their compatibility with printed circuit boards.[36,42] However, our ability to combine good flexibility and breakdown strength with high dielectric BTO suggests the potential to produce rolled capacitors with much higher energy densities than found with traditional, commercial polymer capacitors[2,8] for the reasons noted above. As briefly noted above nano-BTO powders do not reach the

traditionally accepted bulk dielectric constant values.[43] A further point is that the effective composite dielectric constant is strongly affected by the matrix. Thus, despite the much lower dielectric constants achieved with nano-BTO, as we show below, the composite systems are still much superior to commercially used polymer dielectrics.

4.2. Experimental

4.2.1. Materials

Barium hydroxide monohydrate [$Ba(OH)_2 \cdot H_2O$], triethanolamine [$N(CH_2CH_2OH)_3$], and propionic acid [CH_3CH_2COOH] were purchased from Sigma-Aldrich (Milwaukee, WI). Titanium isopropoxide [$Ti(OiPr)_4$] was purchased from Fischer Scientific (Pittsburgh, PA), and 200 proof ethanol from Decon Labs (King of Prussia, PA). Barium titanate [$BaTiO_3$, 50 nm] was purchased from Inframat Corp. (Manchester, CT). Octaglycidyldimethyl-siloxyoctasilsesquioxane [$(glycidyl)Me_2SiOSiO_{1.5})_8$] (OG) was received from Mayaterials Inc. (Ann Arbor, MI) as a gift. 4,4‘-Diaminodiphenylmethane (DDM) was purchased from Alfa Aesar (Ward Hill, MA). All chemicals were used as received.

4.2.2. Precursor synthesis

Barium Propionate [$Ba(O_2CCH_2CH_3)_2$]. [$Ba(OH)_2 \cdot H_2O$, 320 g, 1.69 mole] was reacted with excess [CH_3CH_2COOH, 500 ml, 6.75 mole] in a 1 L flask equipped with a still head. N_2 was sparged directly into the solution as the solution was heated at 130 °C for 2 h with magnetic stirring to distill off ~100 ml of byproduct water and excess propionic acid. The resulting transparent viscous liquid was cooled to room temperature and poured into a 500 ml Nalgene® bottle, and left overnight to crystallize. Crystallized solid barium propionate was pulverized with a mortar and pestle to facilitate its dissolution in ethanol.

Titanatrane {$Ti(OCH_2CH_2)_3N[OCH_2CH_2N(CH_2CH_2OH)_2]$}. [$Ti(OiPr)_4$, 1150 ml, 3.80 mole] was reacted with [$N(CH_2CH_2OH)_3$, 1010 ml, 7.60 mole] at a molar ratio of 1 to 2, in a 4 L vessel under N_2 flow. Triethanolamine was added slowly with an addition funnel while the mixture was stirred constantly over a 4 h period.

4.2.3. Liquid Feed – Flame Spray Pyrolysis

Details of the LF-FSP process are described elsewhere.[44-51] Briefly, metalloorganic precursors such as metal alkoxides, carboxylates, or β-diketonates are dissolved in alcohol, usually ethanol, at 1-10 wt % loading of ceramic as precursors. The resulting solution is subsequently aerosolized with oxygen into a quartz chamber where it is ignited with methane/oxygen pilot torches. Initial combustion takes place producing temperatures of 1500-2000 °C followed by a quenching step which drops the temperature to 300-500 °C over 1.5 m, equivalent to a quench rate of >500 °C sec^{-1}, to produce nano-oxide powders. Powders are collected downstream in rod-in-tube electrostatic precipitators (ESP) operating at 10 kV. Due to the rapid quenching, particles formed are not aggregated but lightly agglomerated and break up easily on ultrasonication or ball-milling. Also, we do not observe phase separation within each particle or compositional variance between particles, as the entire process is so rapid that atomically mixed nano-oxide particles form.

In this study, barium propionate and titanatrane synthesized as described above were dissolved in ethanol at a 1:1 molar ratio to give a 3 wt % ceramic yield solution.

4.2.4. Thin film processing

OG, DDM, and ethanol were added to a 20 ml vial. The mixture was stirred manually until all the DDM dissolved, and $BaTiO_3$ nanopowders were subsequently introduced. The resulting mixture was ball-milled with spherical 99 % alumina beads with 3.0 mm diameter for 36 h to obtain a stable suspension. A ball tumbler (Rotary Tumbler Model B, Tru-Square Metal Products,

Auburn, WA) was used for milling. One fourth of the container was filled with the milling media.

The ball-milled suspension was cast on to indium tin oxide (ITO) coated glass substrates (CB-50IN-S107, Delta Technologies, Ltd., Loveland, CO) via wire wound bar coating (Automatic Film Applicator-1137, Sheen Instrument, Ltd, UK). After allowing the ethanol to evaporate, the nanocomposite films were cured at 150 °C for 6 h under N_2. Films were prepared at $BaTiO_3$ loadings of 0 (0), 30 (69), 40 (77), and 50 (83) vol % (wt %). For example, 410 mg (0.21 mmol) of OG (1.15 g cc^{-1}, 1931 g mol^{-1}), 42 mg (0.21 mmol) of DDM (1.15 g cc^{-1}, 198.26 g mol^{-1}), 3 ml of ethanol, and 1 g of $BaTiO_3$ (6.02 g cc^{-1}) powder were used for a 30 vol % suspension. For complete cross-linking, OG and DDM have to be reacted at a molar ratio of 1:2, however, for the sake of flexibility, 1:1 ratio was adopted.

4.2.5. Rolled capacitor fabrication

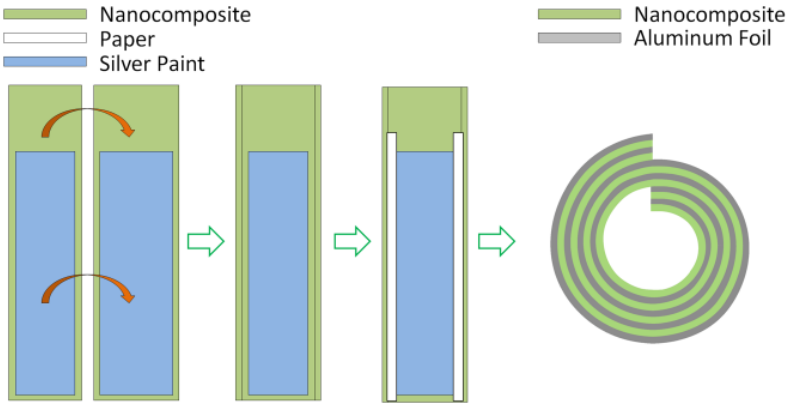

Figure 4.1. Schematic diagram of the fabrication flow of rolled capacitor.

Slurries prepared in the aforementioned method were cast on Al foil, cured, and cut into strips in dimensions of 13 cm × 3.5 cm and 13 cm × 3 cm. Colloidal silver paint was applied on the dielectric layer in dimensions of 10 cm × 3 cm to allow complete contact between electrode (Al

foil) and dielectric layers when stacked. Initial attempts of rolling were done without applying colloidal silver paint which resulted in capacitance of 10 % of what is expected. Contact was determined to be a key element in obtaining close to expected values of capacitance. Strip with narrower width was placed on top of the other. Paper strips were placed on the edges where two Al foil strips met, in order to prevent shorting when rolled. The stack was subsequently rolled using a 4.75 mm diameter rod. Once 10 cm was rolled, the cylinder was secured with tape and the remaining length was left to be used as electrode contacts.

4.2.6. Characterization

X-Ray Powder Diffraction Analyses (XRD) were run using a Rigaku Rotating Anode Goniometer (Rigaku Denki., LTD., Tokyo, Japan). The powder sample was packed on a glass specimen holder. XRD scans were made from 10° to 70° 2θ, using a scan rate of 2° min^{-1} in 0.01° increments and Cu Kα radiation (1.541 Å) operating at 40 kV and 100 mA. The Jade program 2010 (Version 1.1.5 from Materials Data, Inc., Livermore CA) was used to determine the presence of any crystallographic phases.

Specific Surface Area (SSA) Analyses were obtained using a Micromeritics ASAP 2020 sorption analyzer. Samples (400 mg) were degassed at 400 °C/5 h. Each analysis was run at −196 °C (77 K) with N_2. The SSAs were determined by the BET multipoint method using ten data points at relative pressures of 0.05−0.30.

Inductance, capacitance, and resistance (LCR) measurements. The capacitance and dielectric loss of nanocomposite films processed as above were measured using an HP LCR 4284A meter connected with a 16451B dielectric test fixture. Values were measured at five frequencies: 0.1, 1, 10, 100 K, and 1 MHz at 1 V_{rms}. Two samples of each vol % were measured twice on two different days. The average values are reported here. ITO served as a bottom electrode by

grounding to the LCR meter using a colloidal silver paint (Pelco® Colloidal Silver, Ted Pella, Inc., Redding, CA). Circular gold/palladium top electrode (7.4 mm dia.), were deposited onto nanocomposite films by sputter coating using a Technics Hummer IV DC sputtering system (Anatech, Ltd., Alexandria, VA). A spring loaded probe was contacted with the top electrode to eliminate physical damage during measurement. For dielectric constant calculations, film thicknesses were determined by direct SEM imaging of the cross-sections. Four locations were measured and averaged. Cross-sections were found by fracturing the film and substrate. Measurements on rolled capacitors were performed at 100 KHz. We report average values from three measurements. Jump wires were used to clamp electrodes and Al strips on each side.

Scanning electron microscopy (SEM). Micrographs were taken using a FEI NOVA Nanolab system (FEI company, Hillsboro, OR) at mode 2. Samples were sputter coated with gold/palladium using a Technics Hummer IV DC sputtering system (Anatech, Ltd., Alexandria, VA) to prevent charging. Cross-sectional images were obtained by fracturing the films.

Thermogravimetric analyses (TGA). The solid loadings of cured films were confirmed using a 2960 simultaneous DTA-TGA (TA Instruments, Inc., New Castle, DE). Samples (15–25 mg) were loaded in alumina pans and ramped to 1000 °C while heating at 10 °C min^{-1} under constant air flow at 60 ml min^{-1}.

Diffuse reflectance Fourier transform (DRIFT) spectra were recorded on a Nicolet 6700 Series FTIR spectrometer (Thermo Fisher Scientific, Inc., Madison, WI). Optical grade, random cuttings of KBr (International Crystal Laboratories, Garfield, NJ) were ground, with 1.0 wt % of the sample to be analyzed. Samples were scraped off the substrate with a razor blade. For DRIFT analyses, samples were packed firmly and leveled off at the upper edge to provide a smooth surface. The FTIR sample chamber was flushed continuously with N_2 prior to data acquisition in

the range 4000–400 cm^{-1} with a precision of ±4 cm^{-1}.

4.3. Results and Discussion

The general objectives of this research are to assemble high energy density, rolled capacitors using a nanocomposite dielectric layer consisting of a polymeric matrix coupled with ceramic nano-filler. The OG/DDM polymeric matrix itself is a nanocomposite system consisting of a Q silicate (four Si-O bonds per corner) cage decorated with eight glycidyl groups. Both Q cages and many silsesquioxane [$(RSiO_{1.5})_n$] or SQ analogs are quite robust, exhibiting sufficiently high dielectric breakdown strengths to warrant their incorporation in multiple types of devices,[40,41,52,53] and in principle, leading to capacitors with high energy densities, as discussed just below.

Several literature reports describe the addition of SQ fillers (1-10 wt %) in other polymeric hosts as a means of improving breakdown voltages.[40,41] For example Takala et al.[40] report that mixing 1 wt % OG [$(glycidylSiO_{1.5})_8$] with the diglycidylether of bisphenol A (DGEBA) increased breakdown voltages from 61 to 66 kV mm^{-1}. Horwath et al.[41] disperse 5 wt % of trisilanolphenyl SQ [$(C_6H_5)_7(SiO_{1.5})_6Si(OH)_3$] in EPON 828 epoxy resin (DGEBA equivalent) thereby increasing breakdown voltages from 18 to 24 kV when compared to the pure resin. Although the voltage per unit thickness is unknown as the thickness of the sample is not provided, the percent increase in breakdown voltage is significant. While the exact rationale for this behavior is not presented, it is suggested that silica cage allows localized charge movement thereby preventing bulk charge build-up, thus improving dielectric strength.[41]

In the current study, OG serves as the epoxy component of the resin. The silica cage was anticipated to provide improved breakdown resistance whereas the glycidyl units provide flexibility at the nanometer length scale which translates to flexibility at macroscopic length

scales,[33-35] enabling rolled capacitor fabrication. We have previously shown that OG/DDM epoxy resins offer very high flexibility in studies on the mechanical properties of cage silicate epoxy resins.[35]

In the following sections, we begin by characterizing the OG/DDM matrix and the BTO nanopowders separately. Thereafter, we follow with sections on dielectric properties, surface morphologies, and thermogravimetric analyses of BTO/polymer composite films. Analyses of rolled capacitors follow.

4.3.1. OG/DDM Matrix Characterization

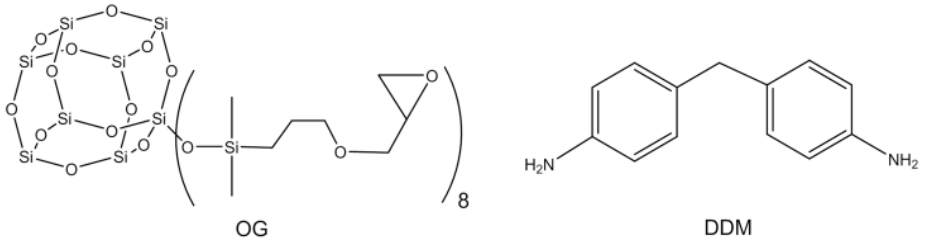

Figure 4.2. Chemical structure of OG and DDM.

As a general background, SQs (3 Si-O bonds per corner) contain silica cores with 8 vertices (body diagonal ≈ 0.5 nm) with an organic functional group in each octant in Cartesian space. Q-cages have 4 Si-O bonds per corner with identical geometries. Figure **4.2** shows the chemical structure of OG and DDM.

One common application of SQ and Q cages is as interlayer dielectrics in electronics due to their typically low dielectric constants ($\varepsilon_r < 3$).[54] In contrast, the dielectric constant of the OG/DDM system is 5.6 at 1 MHz, more than double the typical low-k dielectric SQ/Q systems. Figure **4.3** displays dielectric constants and loss tangents for OG/DDM at selected frequencies. Although it contains a silica core, OG can also be seen as an epoxy, and considering epoxy

dielectric constants are generally between 3 and 6, the observed value is at the higher end.[55]

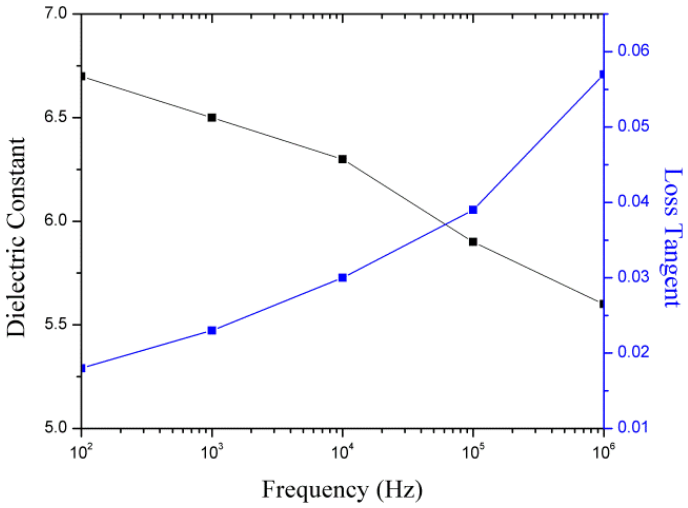

Figure 4.3. Dielectric constant and loss tangent vs. frequency plot of OG/DDM.

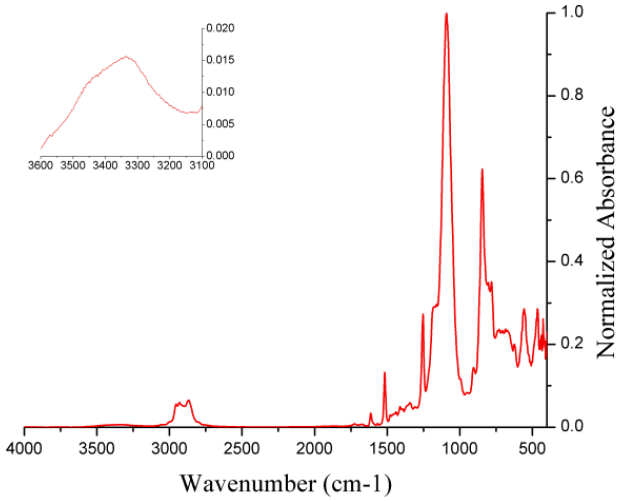

Figure 4.4. FTIR spectrum of a 1:1 OG/DDM film cured at 150 °C/6 h in N_2.

Figure **4.4** shows the FTIR spectrum of a cured OG/DDM film. The FTIR was run to determine if any adsorbed water might be present as water has dielectric constant of 80 and epoxy resins are prone to absorb water.[55] The inset is a zoom in the 3100-3600 cm^{-1} region where νOH for water or

alcohols is present. The observed band is simply that of the epoxy resin, which consists of a combination of νOH and νNH from the curing reaction. There does not appear to be a contribution from water.

4.3.2. $BaTiO_3$ (BTO) Powder Characterization

Figure **4.5** provides XRD patterns of LF-FSP and Inframat BTO. Both powders appear to be the cubic phase since no peak splitting is observed; however, this is a consequence of line broadening which prevents a clear estimation of c/a ratios of the tetragonal phase using XRD alone.

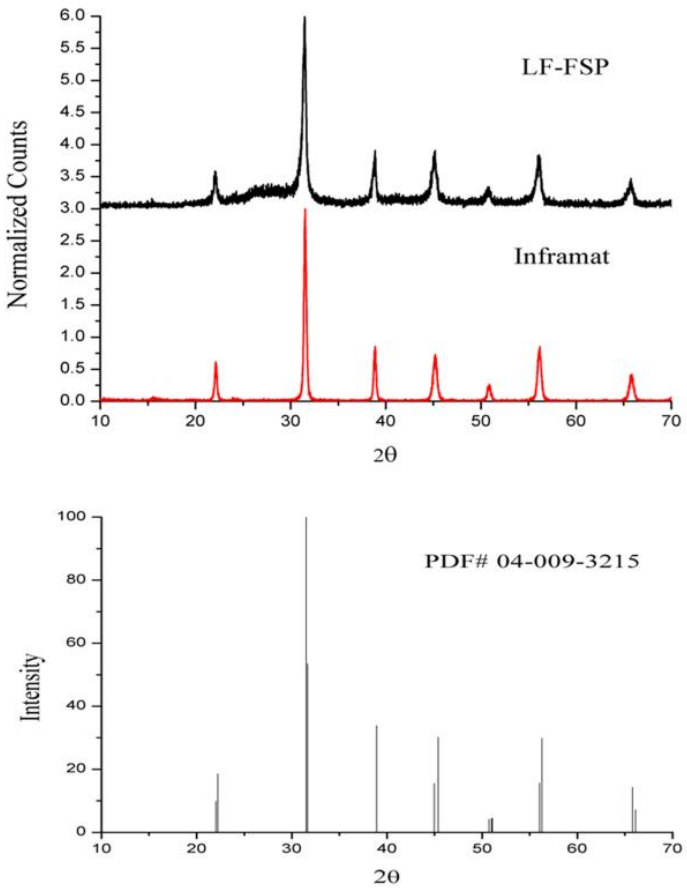

Figure 4.5. XRD pattern of LF-FSP and Inframat BTO.

As the particle size gets smaller, the Curie temperature (T_c) where the tetragonal to cubic phase transition takes place drops below 120 °C, the value of the bulk material, and eventually reaches room temperature.[56] While different arguments are made as to the size at which BTO becomes cubic at room temperature, the tetragonal phase has been observed in 9 nm nanocrystals via Raman spectroscopy and PDF (pair distribution function) analysis.[57] Although XRD fails to detect the tetragonal phase in BTO nanopowders, Raman spectroscopy,[56,57] extended X-ray absorption fine structure (EXAFS),[58] X-ray absorption near-edge structure (XANES)[58] and PDF analysis[57] have all been used to demonstrate the existence of the tetragonal phase in nano BTO particles. Although the tetragonal phase is often observed at very small particle sizes, the observed dielectric constant decreases.[43,59]

The inherent BTO dipole will be greatly diminished as average particle sizes (APSs) are reduced because more material will be at or near the particle surface where high surface energies will cause crystallographic disorder. Thus, the exponential increase in surface area that occurs as APSs get smaller results in higher disorder and thus lower dielectric constants.

The LF-FSP and Inframat BTO powders were found to have BET SSAs of 18 $m^2 g^{-1}$ (APS = 55 nm) and 20 $m^2 g^{-1}$ (APS = 50 nm), respectively. The Figure **4.6** SEMs corroborate these results showing that both powders are spherical and have uniform size distributions.

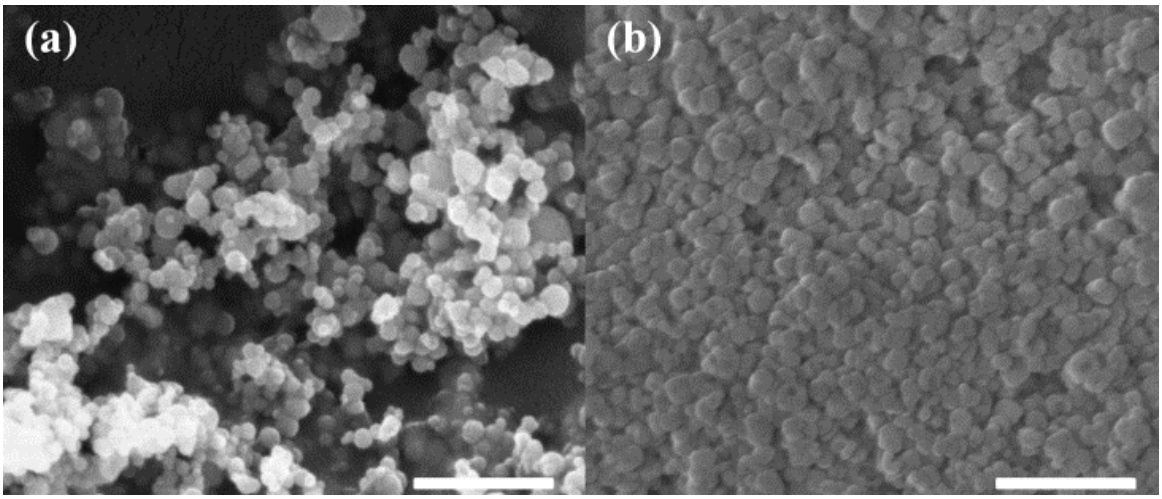

Figure 4.6. SEMs of (a) LF-FSP and (b) Inframat BTO powders. Both scale bars are 500 nm.

4.3.3. Nanocomposite Film Characterization

Having analyzed the individual components, we now compare the dielectric properties of 30 vol % films. Figure **4.7** shows the dielectric constants of 30 vol % films at selected frequencies. Film thicknesses were determined from cross-sectional SEM imaging and found to average ≈ 11 and 10 μm for Inframat and LF-FSP BTO, respectively. Although cast with the same wire round bar, viscosities will differ based on BTO surface chemistries and/or solids loading, thus film thicknesses vary for different samples.

Nanocomposite films with Inframat BTO as filler offer higher dielectric constants than that with LF-FSP BTO at all points. The theoretical equation derived by Jayasundere and Smith,[60] allows us to estimate dielectric constants of 170 and 50 for Inframat BTO and LF-FSP BTO, respectively. Referring to 30 vol % loading SEM images of Figure **4.8**, the lower dielectric constants measured for the LF-FSP BTO films do not seem to arise from voids in the films as the particles are well dispersed in the polymeric matrix except in the 50 vol % films discussed below.

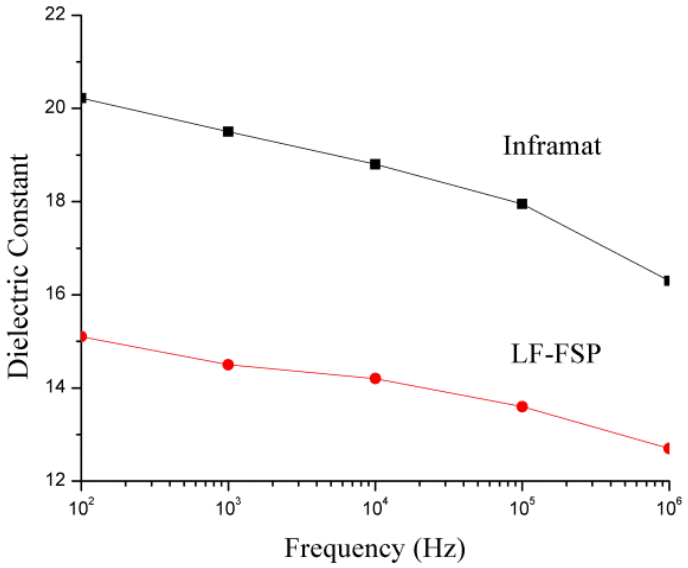

Figure 4.7. Dielectric constant vs. frequency plot of 30 vol % films.

These results suggest that BTO tetragonality is a function of particle size and synthetic method. For the same reason, the critical size at which BTO becomes cubic is controversial as it depends on the preparation method. In LF-FSP process, flame temperature can be varied by using different types of alcohol such as methanol, propanol, or n-butanol instead of ethanol, which was used in current studies.[42] Further studies are necessary to investigate what effects flame temperature has on tetragonality of LF-FSP derived BTO.

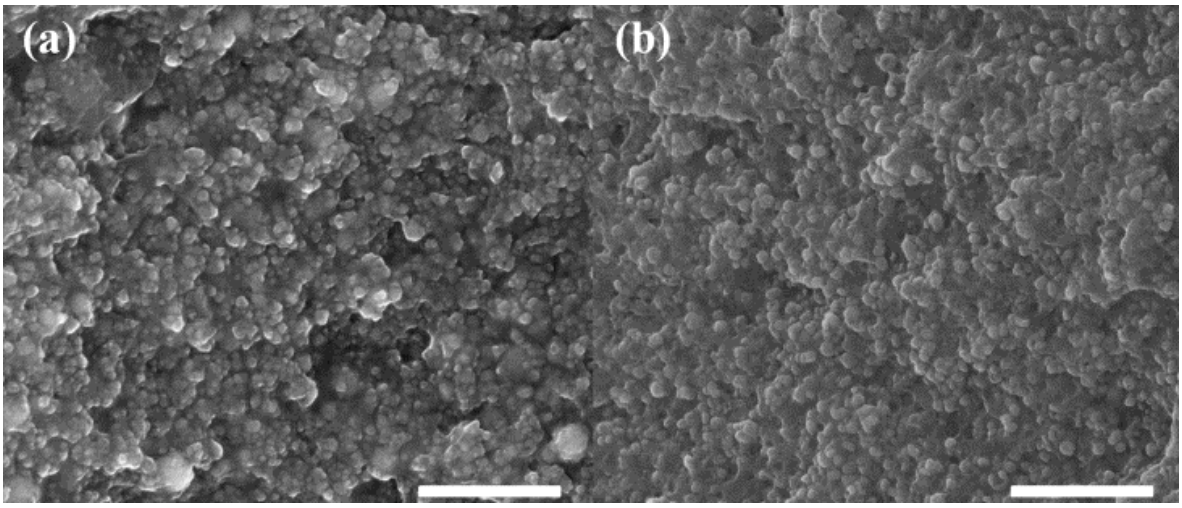

Figure 4.8. Fracture surfaces of 30 vol % (a) LF-FSP BTO and (b) Inframat BTO. Scale bar, 1 μm.

In a similar manner, Terashi et al.[28] report increases in BTO tetragonality for powders made via flame-assisted spray pyrolysis when urea was added to control the heat generated. Two sets of experiments were conducted where urea and precursor concentrations were varied. For both cases, increases in the respective variable correspond directly with increase in particle size of roughly 10 nm and tetragonality. Comparing the data points from urea addition experiments and precursor concentration experiments that produce similar particle sizes, urea addition provides higher degrees of tetragonality. Analogously, for our LF-FSP process, extra heat or higher temperature can be obtained by using propanol or n-butanol[61] and it is expected to increase the tetragonality of BTO powder resulting in higher c/a ratio.

Based on the 30 vol % film properties, only Inframat BTO was used for further studies on 40 and 50 vol % films. Corresponding film thicknesses were 12.5 and 9 μm for 40 and 50 vol % films, respectively. Figure **4.9** records the dielectric constants of nanocomposites at various frequencies. The recorded dielectric constants are 18, 21, and 16 for 30, 40, and 50 vol % films at 100 KHz. These correspond to capacitances per footprint area of 1.4, 1.5, and 1.6 nF cm^{-2}, in the same order.

The value of 50 vol % is higher due to lower thickness although the dielectric constant is found to be less than in the 30 and 40 vol % films. The dielectric constant of the 50 vol % film is below that of the lower solids loadings due to the formation of pores/voids, as seen in Figure **4.10**. Not as significant, but similar regions are observed in 40 vol % film as well. These defects deteriorate the dielectric properties when present even at small fractions[61,62] and indicate actual values would be higher if their formation were prevented; suggesting that improved processing methods would provide still better properties.

The main causes for pore formation are solvent evaporation and powder agglomeration. Ethanol evaporates sufficiently rapidly that powder reorganization may not occur while the net film volume shrinks, resulting in pores. Also, during the course of curing/processing, the powders must remain well dispersed to minimize agglomeration. One obvious future experiment is to use a less volatile solvent together with dispersant or surface modifier. For improved dispersion, not only electrosteric dispersants but also grafting of surface modifiers to powder surfaces have been shown to be effective. Phosphonic acids and silanes have been investigated for this purpose by Kim et al.[9] and Ramesh et al.,[38] respectively. Surface modified powders disperse better than powders dispersed with electrosteric dispersants and also have reduced number of ionizable surface hydroxyls,[63] thereby efficiently passivating the surface.

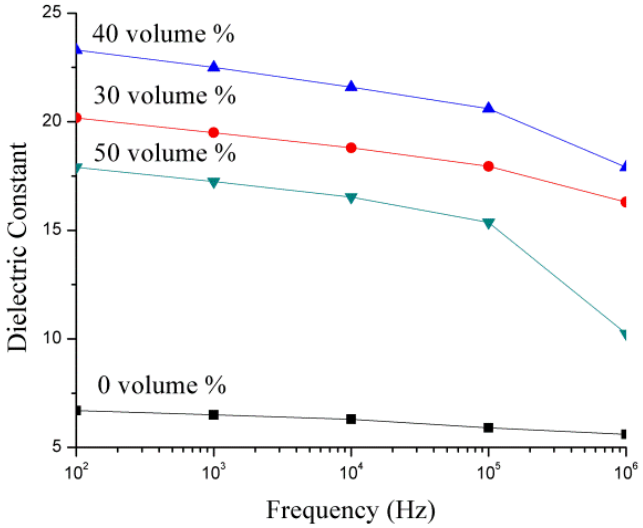

Figure 4.9. Plot of dielectric constant vs. frequency for nanocomposites with different solids loadings.

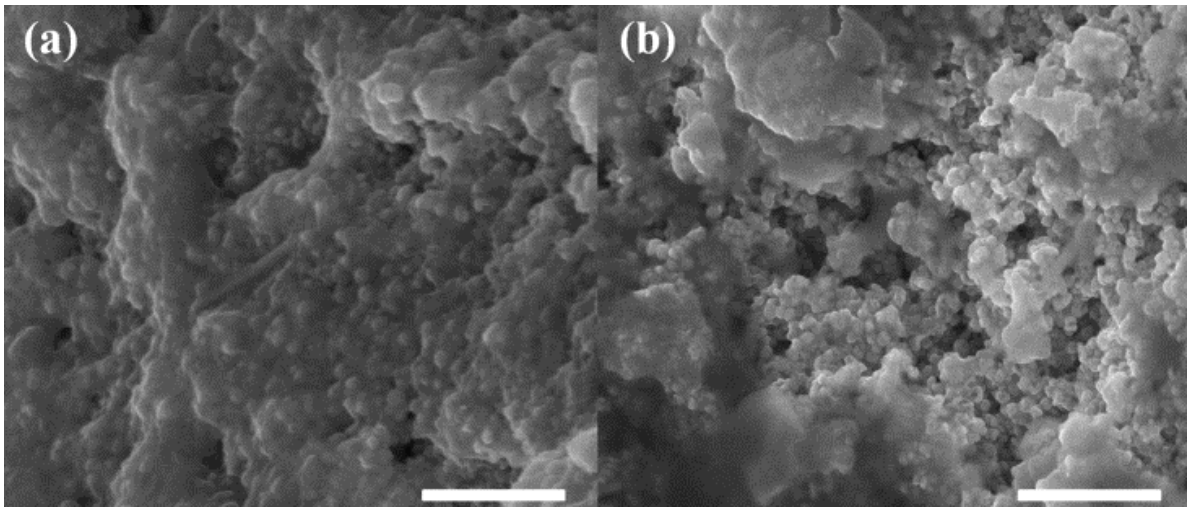

Figure 4.10. Fracture surfaces of (a) 40 vol % and (b) 50 vol % Inframat BTO. Scale bar, 1 µm.

50 vol % films show dramatic drops in dielectric constant as the probe frequency changes from 100 KHz to 1 MHz. We ascribed these changes to agglomeration of BTO filler with the effect emerging at higher frequencies. When the solids loading is low, each particle can maintain a

distinct distance from other particles in a matrix. However, as the volume fraction of particles increases, the chance of particles contacting each other increases greatly. These contacted particles form percolative pathways that aid current leakage.[64] Figure **4.11** clearly shows the loss tangents increase with BTO vol % at higher frequencies.

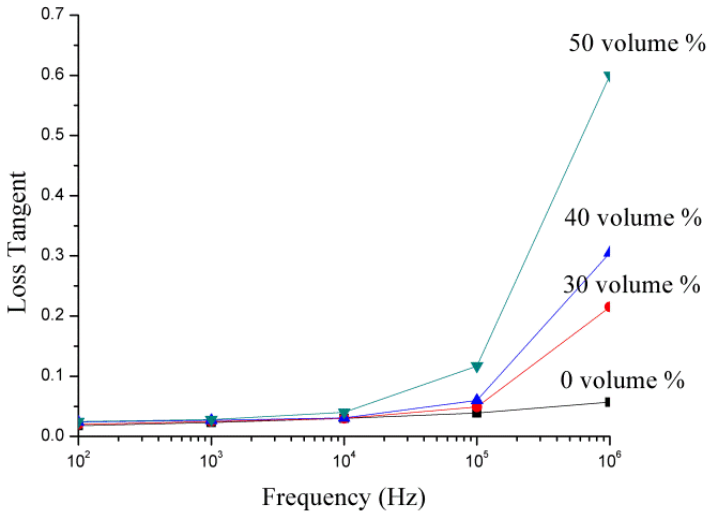

Figure 4.11. Plot of loss tangent vs. frequency for nanocomposites with different solids loadings.

Numerous theoretical models have been proposed to calculate the expected effective dielectric constants of composite films when the volume fraction and dielectric constant of each component is known.[60,65,66] The Jayasundere and Smith[60] equation is useful for estimating the properties of the BTO/epoxy system:[36,67]

$$\varepsilon_{eff.} = \frac{\varepsilon_1 v_1 + \varepsilon_2 v_2 [3\varepsilon_1/(\varepsilon_2 + 2\varepsilon_1)][1 + 3v_2 (\varepsilon_2 - \varepsilon_1)/(\varepsilon_2 + 2\varepsilon_1)]}{v_1 + v_2 [(3\varepsilon_1)/(\varepsilon_2 + 2\varepsilon_1)][1 + 3v_2 (\varepsilon_2 - \varepsilon_1)/(\varepsilon_2 + 2\varepsilon_1)]}$$

Here the subscript "1" and "2" correspond to epoxy and BTO, respectively. "ε" and "v" denote dielectric constant and volume fraction. Films with 30 vol % BTO were chosen as a baseline as

they have no observable defects. Also, 100 KHz was selected as the film exhibits some degree of loss at 1 MHz. At 100 KHz, a dielectric constant of 170 is calculated for the Inframat BTO filler. Using estimated ε_2 with measured ε_1 (=5.9), $\varepsilon_{eff.}$ values up to 60 vol % BTO were generated in Figure **4.12**. Measured data are represented as dots.

For 40 and 50 vol % films, expected dielectric constants are 25 and 36 respectively. These values are higher than the observed dielectric constants as it assumes the films are defect free. Also note that theoretical models provide a rough estimate. One can argue that the dielectric constants of 40 and 50 vol % would be higher if defect formation is prevented through the use of better, less volatile solvents and dispersants.

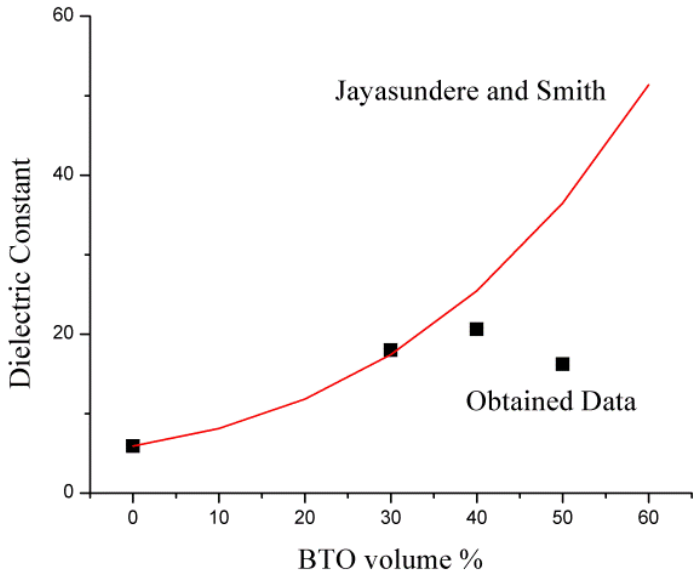

Figure 4.12. Dielectric constant vs. BTO vol % at 100 KHz.

4.3.4. Thermal stability and solids loading analyses

TGAs of the BTO composite films were run to confirm the solids loadings. Figure **4.13** shows the mass loss for each film on heating in air. Matrix decomposition starts at 250 °C and ends at 700 °C. Since OG decomposition produces SiO_2 on heating, the final ceramic yields are higher than typical BTO/polymer composite films. The observed ceramic yields at 1000 °C are 91, 88, 82 wt % for 50, 40, 30 vol % films, respectively. Within the error limits of the method of measurement, the ceramic yields are close to the theoretical values of 90, 88, 83 wt %. Corresponding SiO_2 contents are 15, 11, and 7 wt % in same order.

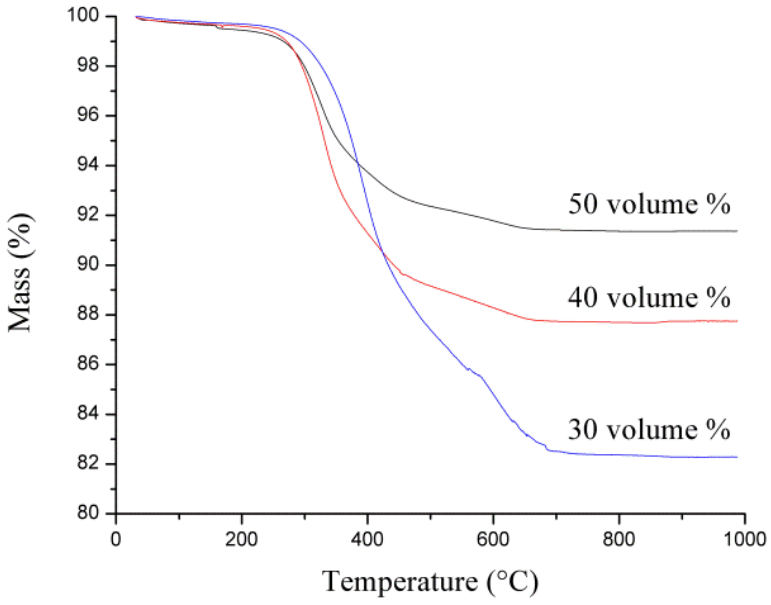

Figure 4.13. TGA of nanocomposite films.

4.3.5. Rolled Capacitor Analyses

Only 30 and 40 vol % films were used for rolled capacitor assembly as 50 vol % films were far from optimal as noted above. Films cast on Al foil had average thicknesses of 11 and 13 μm

for 30 and 40 vol % films, respectively. The rolled capacitor's effective circuit can be visualized as two parallel plate capacitors connected in parallel. Using the dielectric constant obtained from measurements on films cast on ITO, capacitance of 87 and 84 nF were expected for 30 and 40 vol % films. The expected capacitance of the 40 vol % film is lower than that of 30 vol % film due to its greater thickness. Measured capacitances were 84 and 80 nF, close to expected capacitance, in same order at 100 KHz. Corresponding capacitances per footprint area are 34 and 33 nF cm^{-2}, about 22 times their flat counterparts, 1.5 nF cm^{-2}. This is due to a reduction in the footprint area from 35 cm^2 to 2.5 cm^2 and the bottom Al foil contacting the top dielectric layer on winding, resulting in another capacitor layer. It must be pointed out that since the potential application of the studied capacitor is not for microelectronics and the dimensions are in μm scale, capacitance per footprint area may not be apropos; however this perspective is presented only to demonstrate the compactness of a wound configuration. Deviations between expected and measured capacitance may arise from slight differences in actual capacitor area since the silver paint was applied manually.

The films show sufficient flexibility to permit rolling a nanocomposite capacitor. Figure **4.14** provides representative optical images of a rolled capacitor. The cylinder had a height of 3.5 cm and a diameter of 0.7 cm. Wires can be attached on each electrode to fully roll the strips but were not done in this study as the objective was to identify whether the nanocomposite films are flexible enough for rolled capacitor fabrication. Further modification of the design should permit further reductions in the capacitance per unit volume, for example, using a thinner Al foil or casting a thinner nanocomposite film with a smaller diameter wire wound bar.

As a comparison, if BOPP, which has a dielectric constant of 2.2,[8] were used as a dielectric layer with an identical thickness with the case of 30 vol % example, and fabricated in same manner,

the resulting capacitance would be 11 nF (4.5 nF cm^{-2}), about 13 % of the capacitance of 30 vol % nanocomposite film. Thus, the higher dielectric constant of the nanocomposite film leads to much higher capacitance per unit volume at selected voltage (1 V_{rms}). However, in order to calculate maximum energy densities, breakdown strengths must be factored in but were not measured in the current studies.

This first study details the investigation of the BTO/Q-cage epoxy system. Although the exact value of maximum energy density was not derived, several facts such as incorporation of Q components leading to higher breakdown strengths and the composite film maintaining flexibility even at high solids loading proves the system to be worthy of further optimization.

Figure 4.14. Rolled nanocomposite capacitor.

4.4. Conclusions

BTO was synthesized *via* LF-FSP process but had a lower dielectric constant than that of Inframat BTO despite offering similar particle sizes. This suggests the tetragonality of BTO is affected by not only particle size but also the synthesis environment. In LF-FSP, flame temperature can be controlled by using different solvents and the effect of flame temperature on BTO

tetragonality needs to be investigated as extra heat leads to higher tetragonality. The dielectric properties of BTO, OG/DDM nanocomposite films were investigated. Starting at 40 vol %, defects were observed in SEM images and were more pronounced at 50 vol %. 40 and 50 vol % films' observed dielectric constants were lower than predictions from the theoretical model which is likely a consequence of pore/void defects. Further studies with different solvents and the addition of dispersants or surface modifiers are necessary to optimize the system. The use of OG to produce nanocomposite films filled with nano-BTO provides sufficient flexibility to allow processing rolled capacitors.

The maximum energy densities accessible from the system studied were not derived as the breakdown strength has not been measured. However, SQ or Q-cage based polymers are known to have high breakdown voltages leading, in principle, higher energy densities. While the BTO nanopowder dielectric properties and their surface chemistries need further optimization, flexibility at high solids loadings composites proves the system offers considerable potential as a substitute for current polymer film capacitors especially for use in pulse power applications.

We would like to finish by pointing out that Schmidt et al[22,60] describe a novel approach to making wound capacitors at much smaller length scales that takes advantage of the fact that metal foils of very fine dimensions will actually roll up on their own. Their membranes processed by high vacuum atomic layer deposition techniques produce self-rolled capacitors where Al_2O_3 is the insulator, to produce capacitors that are 13 μm in diameter with ≈ 15 layers and 0.2 mm in height, with capacitance per footprint area of ≈ 200 μF cm^{-2}. Unfortunately, the manufacturing techniques appear to be too costly to scale for pulse power applications; although they could offer considerable potential for microelectronic applications.

References

1. W. J. Sarjeant, J. Zirnheld, F. W. MacDougall, J. S. Bowers, N. Clark, I. W. Clelland, R. A. Price, M. Hudis, I. Kohlberg, G. McDuff, I. McNab, S. G. Parler Jr. and J. Prymak, *Handbook of Low and High Dielectric Constant Materials and Their Applications*, *ed.* H. S. Nalwa, Academic Press, San Diego, 1999, vol. 2, ch. 9, pp. 423-491.

2. P. Barber, S. Balasubramanian, Y. Anguchamy, S. Gong, A. Wibowo, H. Gao, H. J. Ploehn and H.-C. Zur Loye, *Materials*, 2009, **2**, 1697-1733.

3. F. W. MacDougall, J. B. Ennis, R. A. Cooper, J. Bates and K. Seal, *Digest of technical papers, 14th IEEE International Pulsed Power Conference*, ed. M. Giesselmann and A. Neuber, IEEE, Dallas, 2003, pp. 513-517.

4. H. Tang and H. A. Sodano, *Nano Lett*., 2013, **13**, 1373-1379.

5. B. Chu, X. Zhou, K. Ren, B. Neese, M. Lin, Q. Wang, F. Bauer and Q. M. Zhang, *Science*, 2006, **5785**, 334-336.

6. X. Zhao, B. M. Sanchez, P. J. Dobson and P. S. Grant, *Nanoscale*, 2011, **3**, 839-855.

7. A. Burke, *J. Power Sources*, 2000, **91**, 37-50.

8. M. Rabuffi and G. Picci, *IEEE Trans. Plasma Sci.*, 2002, **30**, 1939-1942.

9. P. Kim, S. C. Jones, P. J. Hotchkiss, J. N. Haddock, B. Kippelen, S. R. Marder and J. W. Perry, *Adv. Mater.*, 2007, **19**, 1001-1005.

10. L. F. Brown, *IEEE Trans. Ultrason. Ferroelectr. Freq. Control*, 2000, **47**, 1377-1394.

11. D. J. O'Brien, D. M. Baechle and E. D. Wetzel, *J. Compos. Mater.*, 2011, **45**, 2797-2809.

12. J. R. MacDonald, M. A. Schneider, M. C. Schalnat and J. B. Ennis, *Proceedings of the 2012 IEEE International Power Modulator and High Voltage Conference*, ed. F. Hegeler, IEEE, San Diego, 2012, pp. 256-259.

13. J. R. MacDonald, J. B. Ennis, M. A. Schneider, M. C. Schalnat, T. R. Jow and J. Ho, *Proceedings of the 2012 IEEE International Power Modulator and High Voltage Conference*, ed. F. Hegeler, IEEE, San Diego, 2012, pp. 801-804.

14. E. J. Barshaw, J. White, M. J. Chait, J. B. Cornette, J. Bustamante, F. Folli, D. Biltchick, G. Borelli, G. Picci and M. Rabuffi, *IEEE Trans. Magn.*, 2007, **43**, 223-225.

15. G. Sethi, R. Sahul, C. Min, P. Tewari, E. Furman, M. W. Horn and M. T. Lanagan, *IEEE Trans. Compon. Packag. Technol.*, 2009, **32**, 915-925.

16. M. Mackey, A. Hiltner, E. Baer, L. Flandin, M. A. Wolak and J. S. Shirk, *J. Phys. D: Appl. Phys*., 2009, **42**, 175303.

17. C. Zou, Q. Zhang, S. Zhang, D. Kushner, X. Zhou, B. Richard and R. J. Orchard, *J. Vac. Sci. Technol. B: Microelectron. Nanometer. Struct. Process. Meas. Phenom.*, 2011, **29**, 061401.

18. P. Kim, N. M. Doss, J. P. Tillotson, P. J. Hotchkiss, M.-J. Pan, S. R. Marder, J. Li, J. P. Calame and J. W. Perry, *ACS Nano*, 2009, **3**, 2581-2592.

19. J. K. Nunes, M. Ertas, L. Du and J. M. DeSimone, *Chem. Mater*., 2010, **22**, 4069-4075.

20. J. Li, J. Claude, L. E. Norena-Franco, S. I. Seok and Q. Wang, *Chem. Mater*., 2008, **20**, 6304-6306.

21. N. Venkat, T. D. Dang, Z. Bai, V. K. McNier, J. N. DeCerbo, B.-H. Tsao and J. T. Stricker, *Materials Science and Engineering B*, 2010, **168**, 16-21.

22. C. C. B. Bufon, J. D. C. Gonzalez, D. J. Thurmer, D. Grimm, M. Bauer and O. G. Schmidt, *Nano Lett*., 2010, **10**, 2506-2510.

23. C. A. Grabowski, S. P. Fillery, N. M. Westing, C. Chi, J. S. Meth, M. F. Durstock and R. A. Vaia, *ACS Appl. Mater. Interfaces*, 2013, **5**, 5486-5492.

24. S. P. Fillery, H. Koerner, L. Drummy, E. Dunkerley, M. F. Durstock, D. F. Schmidt and R. A. Vaia, *ACS Appl. Mater. Interfaces*, 2012, **4**, 1388-1396.

25. S. F. Wang and G. O. Dayton, *J. Am. Ceram. Soc*., 1999, **82**, 2677-2682.

26. H. Funakoshi, A. Okamoto and K. J. Sato, *Mod. Opt*., 2005, **52**, 1511-1527.

27. F. A. Yildirim, C. Ucurum, R. R. Schliewe, W. Bauhofer, R. M. Meixner, H. Goebel and W. Krautschneider, *Appl. Phys. Lett*., 2007, **90**, 083501-083503.

28. Y. Terashi, A. Purwanto, W.-N. Wang, F. Iskandar and K. Okuyama, *J. Eur. Ceram. Soc*., 2008, **28**, 2573-2580.

29. P. Badheka, L. Qi and B. I. Lee, *J. Eur. Ceram. Soc*., 2006, **26**, 1393-1400.

30. T. Tsurumi, T. Sekine, H. Kakemoto, T. Hoshina, S.-M. Nam, H. Yasuno and S. Wada, *J. Am. Ceram. Soc*., 2006, **89**, 1337-1341.

31. B. D. Begg, E. R. Vance and J. Nowotny, *J. Am. Ceram. Soc*., 1994, **77**, 3186-3192.

32. K. Takahashi, S. Sulaiman, J. M. Katzenstein, S. Snoblen and R. M. Laine, *Australian J. Chem*., 2006, **59**, 564-570.

33. S. Sulaiman, C. M. Brick, C. M. D. Sana, J. M. Katzenstein, R. M. Laine and R. A. Basheer, *Macromolecules*, 2006, **39**, 5167-5169.

34. J. Choi, S. G. Kim and R. M. Laine, *Macromolecules*, 2004, **37**, 99-109.

35. J. Choi, J. Harcup, A. F. Yee, Q. Zhu and R. M. Laine, *J. Am. Chem. Soc*., 2001, **123**, 11420-11430.

36. J. Xu, S. Bhattacharya, P. Pramanik and C. P. Wong, *J. Electron. Mater*., 2006, **35**, 2009-2015.

37. X. Huang, L. Xie, P. Jiang, G. Wang and F. Liu, *J. Phys. D: Appl. Phys*., 2009, **42**, 245407-245417.

38. S. Ramesh, B. A. Shutzberg, C. C. Huang, J. Gao and E. P. Giannelis, *IEEE Trans. Adv. Packaging*., 2003, **26**, 17-24.

39. J. Choi, A. F. Yee and R. M. Laine, *Macromolecules.*, 2003, **36**, 5666-5682.

40. M. Takala, M. Karttunen, P. Salovaara, S. Kortet, K. Kannus and T. Kalliohaka, *IEEE Trans. Dielectr. Electr. Insul.*, 2008**, 15**, 40-51.

41. J.C. Horwath, D.L. Schweickart, G. Garcia, D. Klosterman, M. Galaska, A. Schrand and L.C. Walko, *Conference record of the 2006 IEEE international power modulator conference*, IEEE, Arlington, 2006, pp. 189-891.

42. M. A. Alam, M. H. Azarian, M. Osterman and M. Pecht, *Microelectron. Reliab*., 2011, **51**, 946-952.

43. G. Arlt, D. Hennings, and G. de With, *J. Appl. Phys*., 1985, **58**, 1619-1625.

44. A. C. Sutorik, S. S. Neo, D. R. Treadwell and R. M. Laine, *J. Am. Ceram. Soc*., 1998, **81**, 1477-1486.

45. R. Baranwal, M. P. Villar, R. Garcia and R. M. Laine, *J. Am. Ceram. Soc*., 2001, **84**, 951-961.

46. C. R. Bickmore, K. F.; Waldner, R. Baranwal, T. Hinklin, D. R. Treadwell and R. M. Laine, *J. Eur. Ceram. Soc*., 1998, **18**, 287-297.

47. J. Marchal, T. Hinklin, R. Baranwal, T. Johns and R. M. Laine, *Chem. Mater*., 2004, **16**, 822-831.

48. T. Hinklin, B. Toury, C. Gervais, F. Babonneau, J. J. Gislason, R. W. Morton and R. M. Laine, *Chem. Mater*., 2004, **16**, 21-30.

49. S. Kim, J. J. Gislason, R. W. Morton, X. Q. Pan, H. P. Sun and R. M. Laine, *Chem. Mater*., 2004, **16**, 2336-2343.

50. J. A. Azurdia, J. Marchal, P. Shea, H. Sun, X. Q. Pan and R. M. Laine, *Chem. Mater*., 2006, **18**, 731-739.

51. R. M. Laine, *Ceramics Science and Technology*, ed. R. Riedel and I. W. Chen, Wiley, Weinheim, 2011, vol. 3, ch. 4, pp. 97-116.

52. J. Howarth and D. Schweickart, *Conference record of the 25th international power modulator symposium and 2002 high voltage workshop*, ed. L. Gordon, IEEE, Hollywood, 2002, pp. 644-647.

53. M. Takala, M. Karttunen, J. Pelto, P. Salovaara, T. Munter, M. Honkanen, T. Auletta and K. Kannus, *IEEE Trans. Dielectr. Electr. Insul.*, 2008, **15**, 1224-1235.

54. H. J. Lee, E. K. Lin, H. Wang, W. L. Wu, W. Chen and E. S. Moyer, *Chem. Mater*., 2002, **14**, 1845-1852.

55. M. S. Bhatnagarm, *Polymeric Materials Encyclopedia*, ed. J. C. Salamone, CRC Press Inc., Rochester, 1996, vol. 3, pp. 2233-2238.

56. M. B. Smith, K. Page, T. Siegrist, P. L. Redmond, E. C. Walter, R. Seshadri, L. E. Brus and M. L. Steigerwald, *J. Am. Chem. Soc*., 2008, **130**, 6955-6963.

57. F. A. Rabuffetti and R. L. Brutchey, *J. Am. Chem. Soc*., 2012, **134**, 9475-9487.

58. A. I. Frenkel, M. H. Frey and D. A. Payne, *J. Synchrotron Radiat.*, 1999, **6**, 515-517.

59. V. Buscaglia, M. T. Buscaglia, M. Viviani, L. Mitoseriu, P. Nanni, V. Trefiletti, P. Piaggio, I. Gregora, T. Ostapchuk, J. Pokorný and J. Petzelt, *J. Eur. Ceram. Soc.*, 2006, **26**, 2889-2898.

60. N. Jayasundere and B. V. Smith, *J. Appl. Phys*., 1993, **73**, 2462-2466.

61. Y. Bai, Z. Y. Cheng, V. Bharti, H. S. Xu and Q. M. Zhang, *Appl. Phys. Lett.*, 2000, **76**, 3804-3806.

62. H. Windlass, P. M. Raj, D. Balaraman, S. K. Bhattacharya and R. R. Tummala, *IEEE Trans. Electron. Packag. Manuf.*, 2003, **26**, 100-105.

63. P. H. Mutin, G. Guerrero and A. Vioux, *J. Mater. Chem.*, 2005, **15**, 3761-3768.

64. J. P. Calame, *J. Appl. Phys*., 2006, **99**, 084101.

65. T. Yamada, T. Ueda and S. T. Kitayama, *J. Appl. Phys*., 1982, **53**, 4328-4332.

66. A. Sihvola, *SSTA*., 2000, **1**, 393-415.

67. S. D. Cho, S. Y. Lee, J. G. Hyun and K. W. Paik, *J. Mater. Sci. Mater. Electron.*, 2005, **16**, 77-84.

68. C. Yan, W. Xi, W. Si, J. Deng and O. G. Schmidt, *Adv. Mater*,. 2013, **25**, 539-544.

Chapter 5

Optimizing dopant concentrations of Al^{3+}/Si^{4+} co-doped $LiTi_2(PO_4)_3$ Li^+ conductors and processing to free standing thin films

5.1. Introduction

Lithium ion batteries are of great interest due to their ability to offer high energy densities and excellent cycle life.[1-4] As such, they are now found extensively in commercial devices ranging from portable electronics to hybrid electric (HEV) and/or electric vehicles (EV).[5-8] Rapid growth of the lithium battery market is expected to continue given that HEV/EV applications are relatively young, and new potential applications are emerging such as energy storage systems (ESS) for harnessed renewable energies.[5,7,8]

Although lithium ion battery technology is now well established and has matured considerably over the past several decades;[2,3,5,7] even with current lithium batteries, safety concerns persist due to potential fire hazards especially those resulting from flammable liquid organic electrolytes used currently, mandating development of more reliable electrolytes.[9] Abuse or manufacturing defects can result in over-charge/discharge or internal shorts, causing electrolyte to decompose or to react exothermically with electrodes.[10-12] If the temperature exceeds the melting point of the separators

(130-150 °C) used to prevent contact between the cathode and anode, internal shorts can form with excessive heat output.[13] In some instances, more heat is generated than can be dissipated, resulting in thermal runaway, fires, smokes, and explosions in extreme cases.[14,15] Coincident pressure buildup within the battery pack can cause further mechanical failure within the cell and internal short circuits.[11,12,15] Larger fires or explosions can be envisioned when HEV/EV/ESS lithium batteries fail as the volumes are much greater compared to those of portable electronic devices.[7]

Granted, the likelihood of a lithium battery failure is very low due to strengthened safety regulations and improved safety mechanisms over the past decades.[12] However, concerns continue since lithium ion batteries are expected to serve as primary energy storage devices, replacing batteries based on different chemistries.[5,7,8] Thus, all solid state batteries are sought as alternatives. Both polymer[16-18] and ceramic[18,19] replacements for liquid electrolytes are under intense investigation with ceramic electrolytes considered to be the safest as they offer higher thermal stability and young's modulus. For high performance, solid electrolytes with conductivities comparable to organic electrolytes (> 1 mS cm^{-1}) are required.[20,21]

$LiTi_2(PO_4)_3$ (LTP), one of the most widely studied lithium conducting materials, has a NASICON (sodium super ionic conductor) type structure where corner sharing PO_4 tetrahedra and TiO_6 octahedra networks form the crystal structure framework.[22-24] Two interstitial sites, labeled M1 and M2 are considered for Li^+ ion conduction. For pure LTP, only M1 sites are fully occupied by Li^+ ions.[22,24] The conduction of Li^+ ions is a diffusional process wherein Li^+ ions hop from one site to a neighboring site.[22]

Pioneering studies by Aono et al.[25] explored doping of $LiTi_2(PO_4)_3$ by partially substituting Ti^{4+} or P^{5+} sites with other cations to reach higher total conductivities. Of the materials they studied, $Li_{1+x}M_xTi_{2-x}(PO_4)_3$ (M^{3+} = $A1^{3+}$, Sc^{3+}) had the highest conductivity, 0.7 mS cm^{-1} at 25 °C. The

dramatic increases observed from 2×10^{-3} mS cm^{-1} for undoped to 0.7 mS cm^{-1} in doped material were ascribed primarily to improved densification of the doped materials. Their work prompted many further studies on Al^{3+} doping of $LiTi_2(PO_4)$.[26-32] Other doping studies targeting higher conductivities include substitution of Ge^{4+} on Ti^{4+} sites, and V^{5+} or Nb^{5+} on P^{5+} sites.[29,33,34] The overall conclusion is that the final densities of sintered pellets,[25,29,31] the activation energies of Li^+ conduction,[28,33] the presence of secondary phases,[29,33] and the average grain sizes[31,32,35] influence Li^+ conductivities.

Superionic conductivities (> 1 mS cm^{-1}) are typical for $Li_{1.3}Al_{0.3}Ti_{1.7}(PO_4)_3$ or $Li_{1.5}Al_{0.5}Ge_{1.5}(PO_4)_3$ materials made by glass-ceramic processing.[28,36,37] However, the thicknesses of sheets made this way (1-2 mm) limit gravimetric/volumetric energy densities and are not applicable to actual devices. In order to process thin films (<100 μm), glass sheets are crushed and ball milled to produce powders with properties acceptable for tape casting, and thereafter sintered.[36,38,39]

The motivation for the current work was to synthesize lithium conducting nanopowders in a single step using liquid-feed flame spray pyrolysis (LF-FSP) thereby eliminating the glass forming, crushing, and ball milling steps. Furthermore, nanopowders offer potential access to finer final grain sizes potentially crucial to obtaining higher conductivities.[31,32,35]

We have investigated co-doping of Al^{3+} and Si^{4+} in $LiTi_2(PO_4)_3$ since examples of such materials are rare[40,41] despite Fu's[40] report showing superionic conductivities of 1.5 mS cm^{-1}. Most of the work reported here focuses on $Li_{1.7}Al_{0.3}Ti_{1.7}Si_{0.4}P_{2.6}O_{12}$, which showed the highest conductivities among compositions surveyed. Li_2O is introduced to $Li_{1.7}Al_{0.3}Ti_{1.7}Si_{0.4}P_{2.6}O_{12}$ as a sintering aid, which may cause liquid phase sintering.[42-44] In addition, based on our findings, initial

studies were undertaken to process thin films (50-70 μm) from these powders given that such thicknesses would be ideal for lithium batteries of all types.

5.2. Experimental

5.2.1. Materials

Lithium hydroxide monohydrate [$LiOH \cdot H_2O$], tetraethoxysilane [$Si(OC_2H_5)_4$], triethyl phosphate [$(C_2H_5O)_3PO$], triethanolamine [$N(CH_2CH_2OH)_3$], propionic acid [CH_3CH_2COOH], polyethylene glycol [$H(OCH_2CH_2)_nOH$, M_n=3,400], polyacrylic acid [$(C_3H_4O_2)_n$, M_n=2000], methyl ethyl ketone [$C_2H_5COCH_3$] and benzyl butyl phthalate {2-$[CH_3(CH_2)_3O_2C]C_6H_4CO_2CH_2C_6H_5$, 98%} were purchased from Sigma-Aldrich (Milwaukee, WI). Polyvinyl butyral [$(C_8H_{14}O_2)_n$, B-98, M_n=40,000-70,000] was purchased from Butvar (Avon, OH). Titanium isopropoxide [$Ti(OiPr)_4$] was purchased from Fischer Scientific (Pittsburgh, PA), aluminum tri-sec-butoxide {$Al[OCH(CH_3)CH_2CH_3]_3$} was purchased from Chattem Chemicals (Chattanooga, TN), and absolute ethanol from Decon Labs (King of Prussia, PA).

5.2.2. Precursor Synthesis

5.2.2.1. Lithium propionate [$LiO_2CCH_2CH_3$]

[$LiOH \cdot H_2O$, 113 g, 2.7 mole] was reacted with excess [CH_3CH_2COOH, 500 ml, 6.8 mole] in a 1 L flask equipped with a still head. The solution was heated at 130 °C for 2 h with magnetic stirring until transparent liquid was obtained. On cooling to room temperature, [$LiO_2CCH_2CH_3$] crystallized and was filtered out.

5.2.2.2. Alumatrane [$Al(OCH_2CH_2)_3N$]

[{$Al[OCH(CH_3)CH_2CH_3]_3$}, 1700 ml, 6.7 mole] was reacted with [$N(CH_2CH_2OH)_3$, 885 ml, 6.7 mole] at a molar ratio of 1 to 1, in a 4 L vessel under N_2 flow. [$N(CH_2CH_2OH)_3$] was added slowly via addition funnel while the mixture was stirred constantly over a 4 h period.

5.2.2.3. Titanatrane glycolate [$Ti(OCH_2CH_2)_3N[OCH_2CH_2N(CH_2CH_2OH)_2]$]

[$Ti(OiPr)_4$, 1150 ml, 3.80 mole] was reacted with [$N(CH_2CH_2OH)_3$, 1010 ml, 7.60 mole] at a molar ratio of 1 to 2, in identical method described above.

5.2.3. Powder Synthesis

In this study, lithium propionate, alumatrane, titanatrane glycolate, tetraethoxysilane, and triethyl phosphate were dissolved in ethanol at selected molar ratios to give a 3 wt. % ceramic yield solution. The resulting solution was subsequently aerosolized with oxygen into a quartz chamber where it was ignited with methane/oxygen pilot torches. Produced powders were collected downstream in rod-in-tube electrostatic precipitators (ESP) operated at 10 kV. Details of the LF-FSP process including particle formation mechanism and metalloorganic precursor studies can be found elsewhere.[45-49]

$Li_{1+x+y}Al_xTi_{2-x}Si_yP_{3-y}O_1$ (x = 0.1, 0.3 / y = 0.2, 0.4) were synthesized to determine which composition shows the highest potential to reach superionic conductivity. Once $Li_{1.7}Al_{0.3}Ti_{1.7}Si_{0.4}P_{2.6}O_{12}$ was shown to have the highest conductivity, another powder with 10 wt% excess lithium, in respect to stoichiometric amount of lithium, was produced by dissolving excess lithium propionate in precursor solution to investigate the effect of lithium content, hereafter referred to as LATSP and LATSP+10% respectively.

5.2.4. Powder processing and pellet compaction

The as-produced $Li_{1+x+y}Al_xTi_{2-x}Si_yP_{3-y}O_{12}$ (x = 0.1, 0.3 / y = 0.2, 0.4) powders which were used for preliminary experiments were pressed in a dual action 14.2 mm WC die and no treatment on powder or further pressing to improve green densities were performed.

Extra steps were adopted to enhance green densities of LATSP and LATSP+10% to optimize final, sintered densities and ionic conductivities. Selected amount of as-produced powders (18 g) were dispersed in ethanol (300 ml) with an ultrasonic horn (Vibra cell VC-505, Sonics and Materials, Inc., Newton, CT) at 100 W for 15 min and left for 24 h to allow larger particles to settle. The suspension was decanted, dried, re-dispersed (100W, 15 min) in ethanol (300 ml) with addition of 4 wt %, in respect to powder mass, of poly ethylene glycol, and dried again. The resulting powders were ground in an alumina mortar and pestle, and subsequently sieved through 80 μm nylon mesh. The granulated powders (350 mg) were pressed in a dual action 14.2 mm WC die, followed by cold isostatic pressing (Autoclave engineers, Erie, PA) at 200 MPa for 30 min.

$Li_{1.7}Al_{0.3}Ti_{1.7}Si_{0.4}P_{2.6}O_{12}$ with 5 % excess lithium (LATSP+5%) was formulated by mixing LATSP and LATSP+10% in a 1:1 wt. ratio by ultrasonication (100 W, 15 min). Identical procedures as above were done for pellet compaction.

5.2.5. Thin Film Preparation

Table **5.1** lists the components used to cast films. Powder, dispersant, and solvent were ball-milled with spherical 99 % alumina beads with 3.0 mm diameter for 6 h in a 20 ml vial to break up agglomerates and disperse powder. Subsequently, binder and plasticizer were introduced and the new mixture was ball-milled for additional 24 h to homogenize the suspension. A ball tumbler (Rotary Tumbler Model B, Tru-Square Metal Products, Auburn, WA) was used for milling. One fifth of the container was filled with the milling media.

Table 5.1. Starting materials and composition for film casting.

	Role	mass (g)	wt. %	vol. %
LATSP+5%	Powder	1.00	30	12
Benzyl butyl phthalate	Plasticizer	0.14	4	4
Polyvinyl butyral	Binder	0.14	4	4
Polyacrylic acid	Dispersant	0.03	1	1
Ethanol	Solvent	0.4	12	16
Methyl ethyl ketone	Solvent	1.6	49	64

Suspensions were cast using a wire wound rod coater (Automatic Film Applicator-1137, Sheen Instrument, Ltd, UK). Spacers were places between the rod and the substrate to maintain a gap of 400 µm. After solvent evaporation, resulting green films had thicknesses of ~75 µm. Dried green films were manually peeled off the Mylar substrate, and cut to 2.5 × 2.5 cm.

5.2.6. Crystallization and sintering

Heat treatments were conducted in a Lindberg/Blue M single zone tube furnace (Watertown, WI). For quick test of $Li_{1+x+y}Al_xTi_{2-x}Si_yP_{3-y}O_{12}$ (x = 0.1, 0.3 / y = 0.2, 0.4) samples, pellets were heated to 900, 1000, 1100, and 1200 °C at a ramp rate of 5 °C min^{-1} and held for 1 h. For LATSP with varying lithium content studies, green pellets were heated to 690°, 680°, and 660 °C at a ramp rate of 5 °C min^{-1} for LATSP, LATSP+5%, and LATSP+10 % respectively. The temperature was held for 1 h at constant air flow of 60 ml min^{-1}. Crystallized pellets of LATSP, LATSP+5% and LATSP+10 % were sintered at 1200°, 1180°, and 1140 °C respectively for 1 h under 60 ml min^{-1} air flow. The ramp rate was 5 °C min^{-1} to 700 °C and 1 °C min^{-1} to the target temperature. For film studies, green films were placed in between alumina plates and debindered/crystallized at 665 °C for 2 h at a ramp rate of 5 °C min^{-1} followed by sintering at 1000 °C for 1 h at a ramp rate of 1 °C min^{-1}. Alumina plates were used to prevent warping. Sintering temperatures were limited to 1000 °C as LATSP films sintered onto alumina plates at higher temperatures.

5.2.7. Polishing and Thermal etching of sintered pellets

For SEM imaging, sintered pellets were ground and polished using Leco Spectrum System 1000 Grinder/Polisher (St. Joseph, MI). The pellets were initially ground with 1200 grit SiC paper (LECO, St. Joseph, MI), and polished with 9, 3, and 1 μm diamond suspensions (Dexter, MI) subsequently. Polished samples were subject to thermal etching at 900°C for 3 h.

5.2.8. Characterization

Green pellet densities were calculated by geometrical methods. Diameter, thickness, and mass were measured. Densities of sintered pellets and films were determined using an Archimedes density determination kit (OHAUS Corp., Parsippany, NJ). Suspended and wet masses were measured with pellets and films boiled in ethanol for 1 h. Dry masses were measured after heating the samples at 90 °C for 3 h.

X-Ray powder diffraction (XRD) analyses were run using a Rigaku Rotating Anode Goniometer (Rigaku Denki., LTD., Tokyo, Japan). XRD scans were made from 10° to 70° 2θ, using a scan rate of 2° min^{-1} in 0.01° increments and Cu Kα radiation (1.541 Å) operating at 40 kV and 100 mA. As-produced powders, sintered pellets, and sintered films were XRD scanned. The sintered pellets and films were pulverized with agate mortar and pestle. Silicon powder was mixed with ground pellet powder in same fashion and used as an internal standard for lattice parameter calculations. The Jade program 2010 (Version 1.1.5 from Materials Data, Inc., Livermore CA) was used to refine lattice constants, and to determine the presence of crystallographic phases and their quantity in wt. fraction.

Specific surface areas (SSA) were obtained using a Micromeritics ASAP 2020 sorption analyzer. Samples (400 mg) were degassed at 400 °C/5 h. Each analysis was run at −196 °C (77

K) with N_2. The SSAs were determined by the BET multipoint method using ten data points at relative pressures of 0.05−0.30.

Micrographs were taken using a FEI NOVA Nanolab system (FEI company, Hillsboro, OR). Powder samples were used as is, sintered pellets were polished/etched, and thin films were fractured for imaging. All samples were sputter coated with gold/palladium using a Technics Hummer IV DC sputtering system (Anatech, Ltd., Alexandria, VA).

Crystallization points of as-produced, amorphous powders were confirmed using a Q600 simultaneous TGA/DSC (TA Instruments, Inc., New Castle, DE). Samples (15–25 mg) were loaded in alumina pans and ramped to 700 °C while heating at 10 °C min^{-1} to 600 °C and 1 °C min^{-1} to 700 °C, under constant air flow at 60 ml min^{-1}. The solids loadings of the green films were determined by the same method.

AC impedance data were collected with broadband spectrometer (Novocontrol technologies, Hundsangen, Germany) in a frequency range of 10 MHz to 1 Hz at 25° to 125 °C in increments of 20 °C. All measurements were done at root mean square voltage of 10 mV. Pellet and film surfaces were gently smoothened with 1200 grit SiC paper (LECO, St. Joseph, MI). Gold electrodes, 1 mm in diameter, were deposited using a SPI sputter coater (SPI Supplies, Inc., West Chester, PA) on one side of the surface whereas the other side was coated in full. Obtained Nyquist plots were fit using EIS spectrum analyzer software[50] to estimate total resistance of samples. Conductivities were calculated using the following equation. Here, d, A_e, and R denote pellet thickness, electrode area, and resistance, respectively.

$$\sigma = d/A_eR \quad (1)$$

Activation energies were calculated from Arrhenius plots using the equations below. Here, A, E_a, R_g, and T corresponds to pre-exponential factor, activation energy, gas constant, and absolute temperature, respectively.

$$\sigma = A \exp(-E_a/R_gT) \quad (2)$$

$$\log\sigma = \log A - (E_a/2.3R_gT) \quad (3)$$

5.3. Results and Discussion

The objectives of the work reported here were to identify nanopowder compositions in the $Li_{1+x+y}Al_xTi_{2-x}Si_yP_{3-y}O_{12}$ system made by LF-FSP that offer Li superionic conductivities in sintered bodies, and that permit processing thin films for membrane applications.

This section is separated into three parts. The first concerns the brief evaluation of $Li_{1+x+y}Al_xTi_{2-x}Si_yP_{3-y}O_{12}$ (x = 0.1, 0.3/y = 0.2, 0.4) samples to determine which sintered pellet compositions show the highest conductivities. Li^+ ionic conductivities and XRD studies of sintered pellets are discussed.

The second part pertains to composition optimization for conductivity. The effects of sintering temperatures and added excess Li_2O are also explored. Discussions on phase compositions, microstructures, and impedance measurements of sintered pellets are presented.

The third pertains to initial efforts to process thin films. Green and sintered films were characterized by TGA, SEM and XRD. The Li^+ ionic conductivities studies of sintered films follow.

Figure **5.1** is a schematic experimental flow chart, divided by three parts as aforementioned.

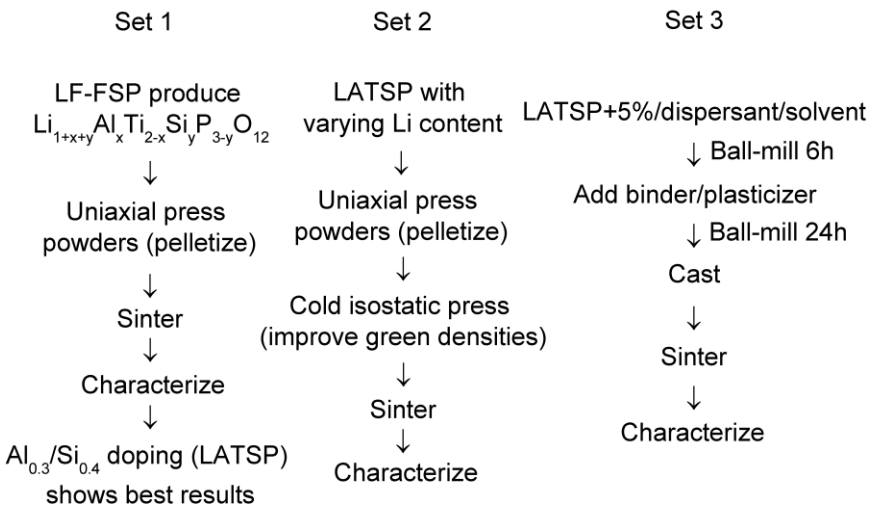

Figure 5.1. Schematic experimental flow chart.

5.3.1. $Li_{1+x+y}Al_xTi_{2-x}Si_yP_{3-y}O_{12}$ (x = 0.1, 0.3/y = 0.2, 0.4) compositions

We begin with a global characterization of the as-produced powders including XRD, BET and SEM.

5.3.1.1. As-produced powders

Figure **5.2** shows SEM micrographs of as-produced powders of all compositions. For all, spherical particles with APSs < 100 nm are observed.

Table **5.2** lists specific surface areas (SSAs) and average particle sizes (APSs) for as-produced $Li_{1+x+y}Al_xTi_{2-x}Si_yP_{3-y}O_{12}$ (x = 0.1, 0.3/y = 0.2, 0.4) nanopowders. The density of Li_2O-Al_2O_3-TiO_2-P_2O_5 glass, 2.69 g cm^{-3}, was used as an approximation to convert SSAs to APSs.[51] APSs of all powders are < 100 nm, consistent with Figure **5.2** SEMs.

Figure **5.3** provides XRD patterns of as-produced $Li_{1+x+y}Al_xTi_{2-x}Si_yP_{3-y}O_{12}$ (x = 0.1, 0.3/y = 0.2, 0.4) nanopowders. All are amorphous as evidenced by broad humps centered at ~24° 2θ.

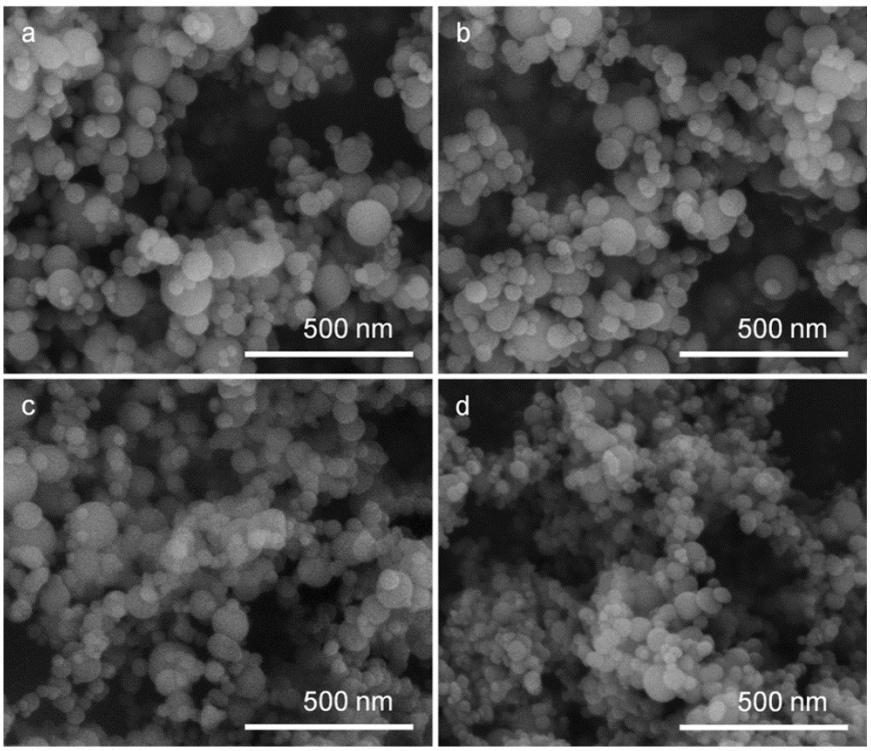

Figure 5.2. SEM micrographs of as-produced a. $Al_{0.1}/Si_{0.2}$, b. $Al_{0.1}/Si_{0.4}$, c. $Al_{0.3}/Si_{0.2}$, and d. $Al_{0.3}/Si_{0.4}$ nanopowders.

Table 5.2. SSAs and APSs of as-produced $Li_{1+x+y}Al_xTi_{2-x}Si_yP_{3-y}O_{12}$ (x = 0.1, 0.3/y = 0.2, 0.4).

	SSAs ($m^2\ g^{-1}$)	APSs (nm)
$Li_{1.3}Al_{0.1}Ti_{1.9}Si_{0.2}P_{2.8}O_{12}$	30	74
$Li_{1.5}Al_{0.1}Ti_{1.9}Si_{0.4}P_{2.6}O_{12}$	35	64
$Li_{1.5}Al_{0.3}Ti_{1.7}Si_{0.2}P_{2.8}O_{12}$	32	70
$Li_{1.7}Al_{0.3}Ti_{1.7}Si_{0.4}P_{2.6}O_{12}$	40	56

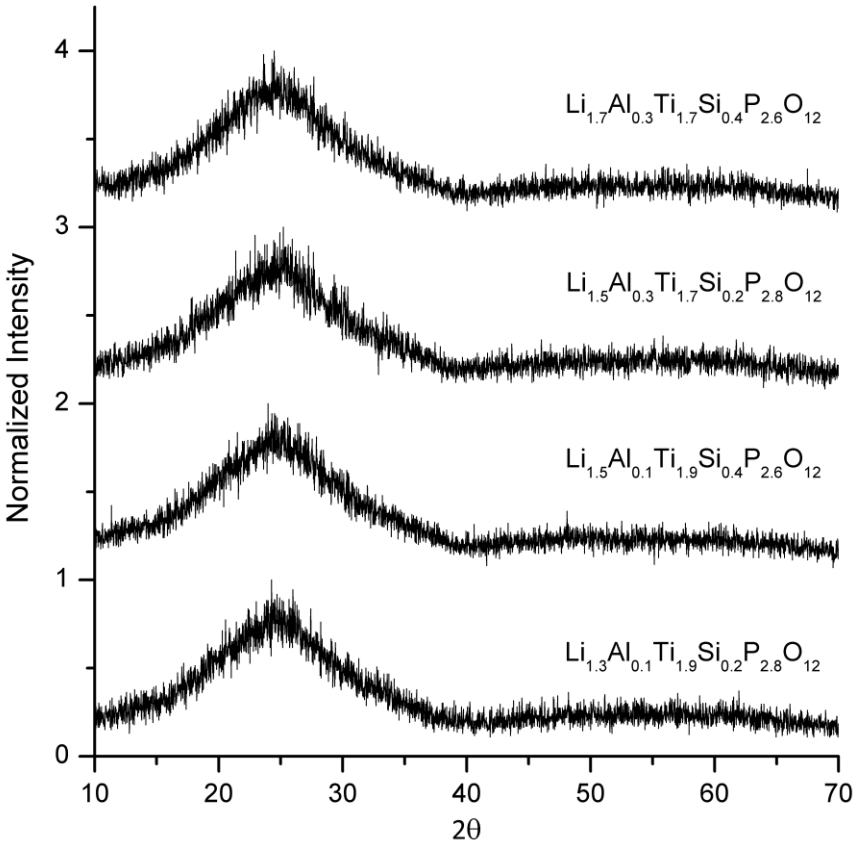

Figure 5.3. XRD patterns of as-produced $Li_{1+x+y}Al_xTi_{2-x}Si_yP_{3-y}O_{12}$ (x = 0.1, 0.3 / y = 0.2, 0.4).

5.3.1.2. Sintering and ionic conductivities

Pellets of $Li_{1+x+y}Al_xTi_{2-x}Si_yP_{3-y}O_{12}$ (x = 0.1, 0.3/y = 0.2, 0.4) were heated at 5 °C min^{-1}/air and sintered at 900°, 1000°, 1100°, and 1200 °C for 1 h. Figure **5.4** shows the XRD patterns of pellets sintered to 1100 °C for 1 h. All peaks correspond to those of $LiTi_2(PO_4)_3$ for the $Li_{1.3}Al_{0.1}Ti_{1.9}Si_{0.2}P_{2.8}O_{12}$ sample. Small quantities of $AlPO_4$ and TiO_2 are detected for samples with higher doping concentrations of either Al^{3+} or Si^{4+}. Phase separation/formation of $AlPO_4$ or TiO_2 is common for these types of material on sintering at > 900 °C.[40,41,52,53] No secondary phases related to Si^{4+} are observed.

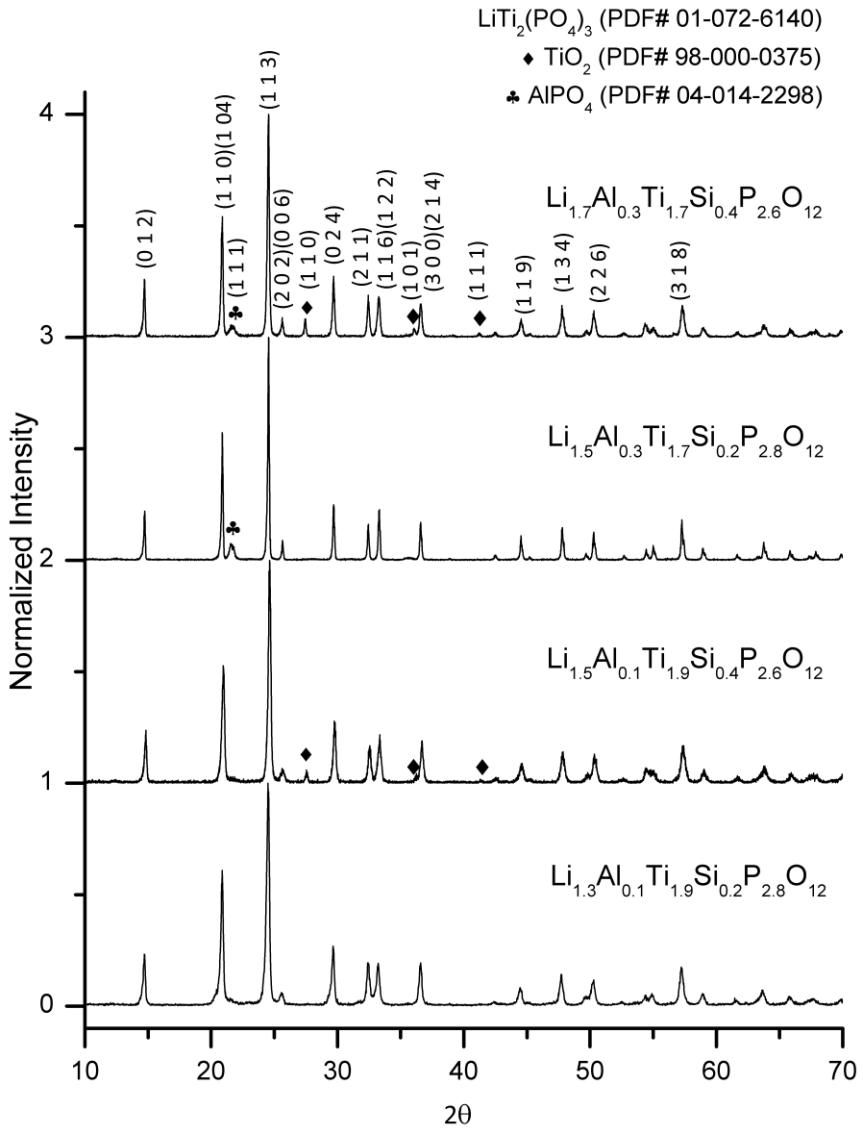

Figure 5.4. XRD patterns of $Li_{1+x+y}Al_xTi_{2-x}Si_yP_{3-y}O_{12}$ (x = 0.1, 0.3/y = 0.2, 0.4) pellets sintered at 1100 °C / 1 h. Peaks with no label correspond to $LiTi_2(PO_4)_3$.

Figure **5.5** presents XRD patterns for $Li_{1.3}Al_{0.3}Ti_{1.7}Si_{0.4}P_{2.6}O_{12}$ pellets sintered to selected temperatures. Pellets sintered at 900 °C are mostly phase pure $LiTi_2(PO_4)_3$ with small amounts of residual amorphous phase, as evidenced by a small, broad hump at ~24° 2θ. Pellets sintered at 1000 °C and above are highly crystalline, and $AlPO_4$ and TiO_2 secondary phases are present. For all $Li_{1+x+y}Al_xTi_{2-x}Si_yP_{3-y}O_{12}$ (x = 0.1, 0.3/y = 0.2, 0.4) samples, higher sintering temperatures resulted in gradual increases in secondary phase peak intensities indicating loss of Li_2O.

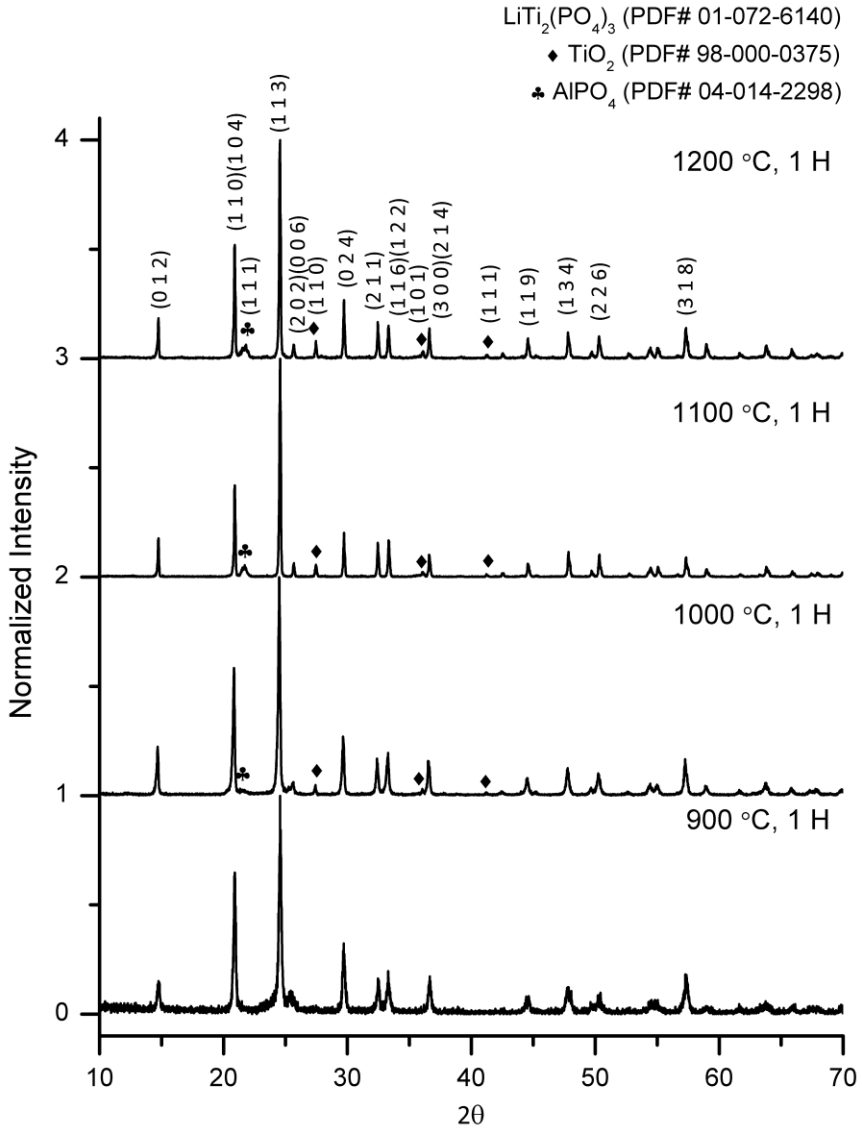

Figure 5.5. XRD patterns of $Li_{1.7}Al_{0.3}Ti_{1.7}Si_{0.4}P_{2.6}O_{12}$ pellets sintered at selected temperatures. Peaks with no label correspond to $LiTi_2(PO_4)_3$.

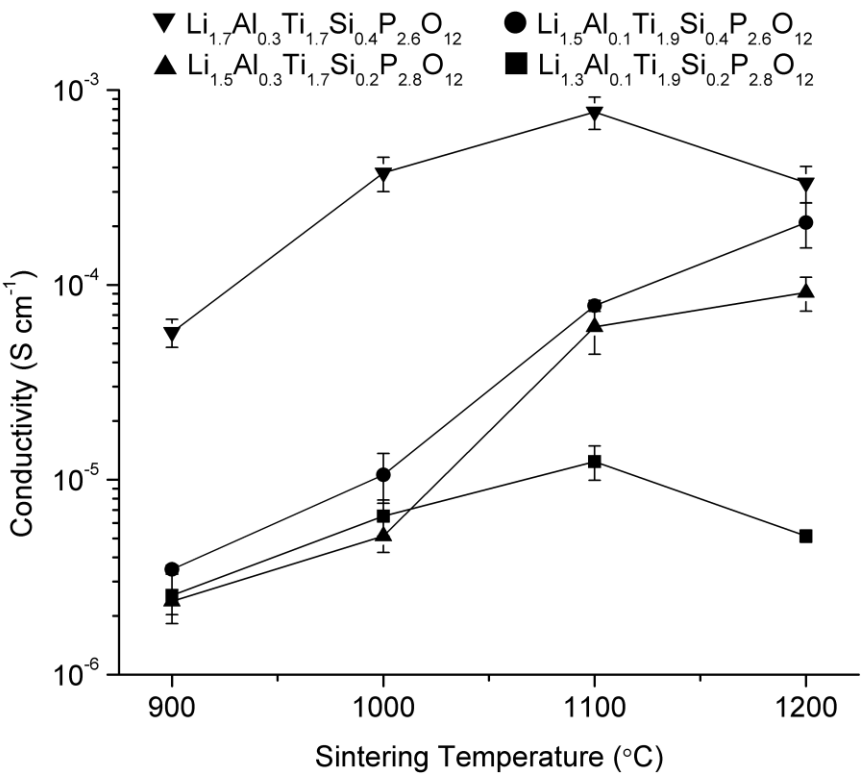

Figure 5.6. Room temperature conductivities of samples sintered at selected temperature for 1 h.

Figure **5.6** summarizes the room temperature conductivities for $Li_{1+x+y}Al_xTi_{2-x}Si_yP_{3-y}O_{12}$ (x = 0.1, 0.3/y = 0.2, 0.4) pellet samples. These initial samples provided a quick estimate of compositions that show the best potential to reach superionic conductivities. No efforts were made to optimize each composition in terms of densities and conductivities. Rather, all samples were simply pelletized by uni-axial pressing and sintered at selected temperatures and dwell times.

Figure **5.6** shows a general trend wherein room temperature conductivities increase with sintering temperature as pellets densify.[25] $Si_{0.4}$ doped samples offer higher conductivities compared to $Si_{0.2}$ doped samples. Also, higher doping concentrations result in higher conductivities. Thus $Li_{1.7}Al_{0.3}Ti_{1.7}Si_{0.4}P_{2.6}O_{12}$ shows the highest conductivity at all sintering temperatures. The highest value of 0.77 ($\pm$0.15) mS cm^{-1} is observed for pellets sintered at 1100 °C for 1 h.

The next step was to further optimize $Li_{1.7}Al_{0.3}Ti_{1.7}Si_{0.4}P_{2.6}O_{12}$ (LATSP). Thus, pelletized samples were cold isostatically pressed (CIPped) to improve green densities. CIPped pellets had 56% theoretical densities (TD), 10% higher than isostatically pressed pellets. Furthermore, the effects of excess lithium content on overall sintering behavior and conductivity were investigated.

The following section pertains to LATSP synthesized with excess lithium as Li_2O. LATSP+5% and LATSP+10% each denote 5 and 10 wt% excess lithium, respectively. LATSP+10% was synthesized by using 10 wt% extra lithium propionate compared to the stoichiometric amount, whereas LATSP+5% was made by mixing LATSP and LATSP+10% by ultrasonication. The excess lithium precursor is expected to form Li_2O on heating.

5.3.2. LATSP / LATSP+5% / LATSP+10%

5.3.2.1. As-produced powders

Figure **5.7** provides XRD patterns of as-produced powders. The broad humps centered at ~24° 2θ, observed for both LATSP and LATSP+10% are typical of amorphous samples. Table **5.3** lists SSAs with APSs determined by N_2 adsorption. Figure **5.8** SEMs of as-produced powders show spherical particles with APSs < 100 nm.

The Figure **5.9** DSC scans show the crystallization exotherms for LATSP, LATSP+5%, and LATSP+10%. In each sample, only one exotherm is observed for the $LiTi_2(PO_4)_3$ phase. The crystallization peak maxima shift from 667±1° to 662±1° and to 656±1 °C with increasing Li_2O content.

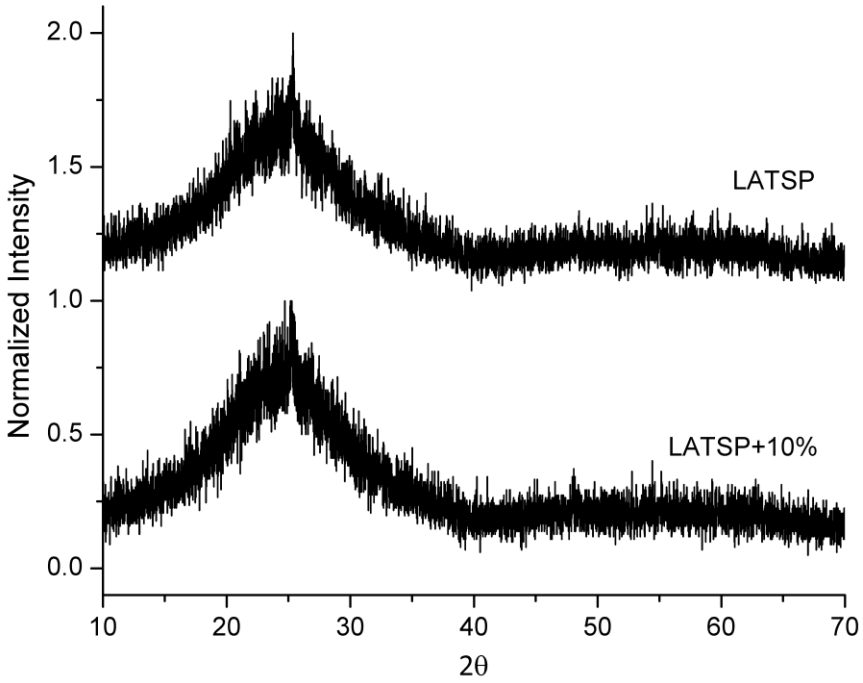

Figure 5.7. XRD patterns of as-produced LATSP and LATSP+10% nanopowders.

Table 5.3. SSAs and APSs of LATSP and LATSP+10%.

	SSAs ($m^2 g^{-1}$)	APSs (nm)
LATSP	40	56
LATSP+10%	35	64

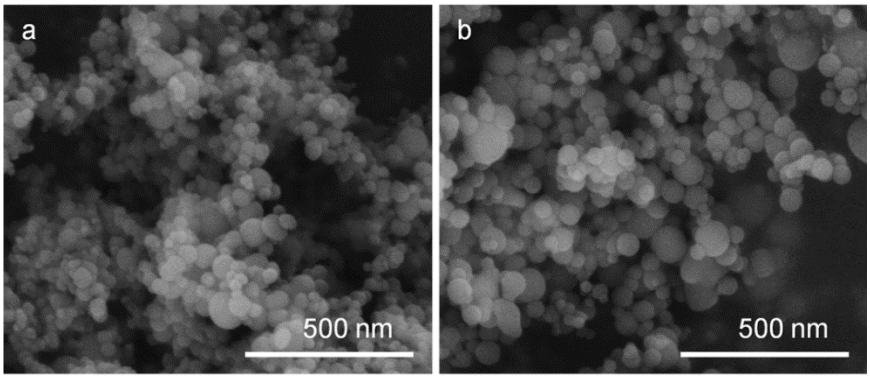

Figure 5.8. SEM micrographs of as-produced a. LATSP and b. LATSP+10% nanopowders.

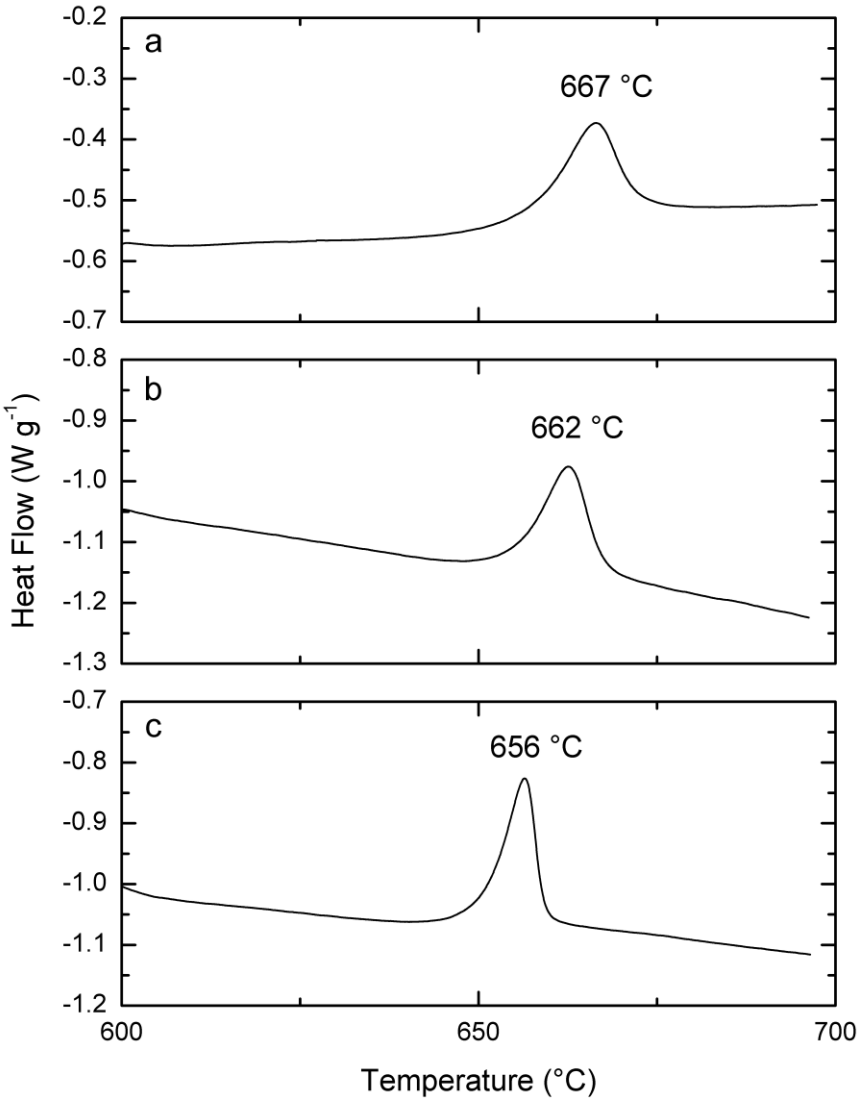

Figure 5.9. DSC scans of a. LATSP, b. LATSP+5%, and c. LATSP+10% powder.

5.3.2.2. Crystallization and sintering

Thereafter, green pellets were first crystallized at selected temperatures to avoid cracking during crystallization. They were subsequently sintered at higher temperatures for densification. Figure **5.10** shows XRD patterns of samples sintered to the highest densities. All peaks correspond to those of $LiTi_2(PO_4)_3$ except two assigned to $AlPO_4$ and TiO_2.

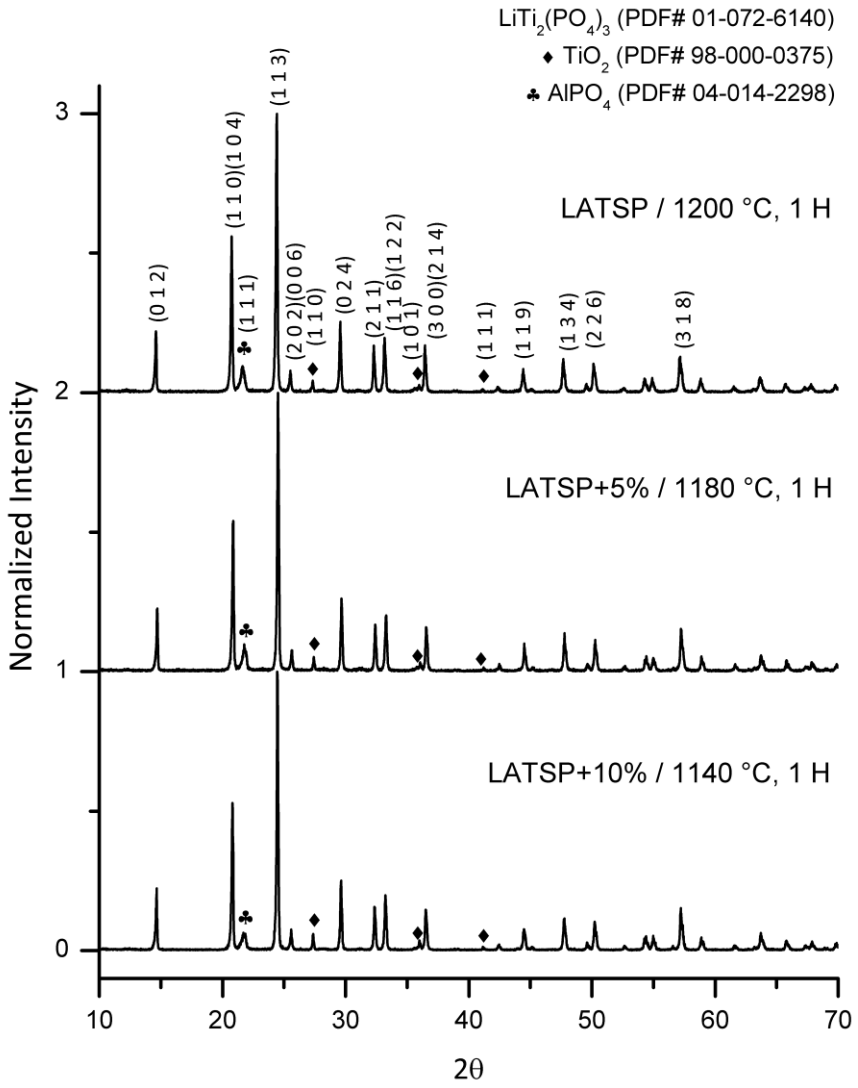

Figure 5.10. XRD patterns of final, sintered pellets with the highest densities.

Table 5.4. Heating conditions, final densities, and phase compositions of sintered pellets.

	Heating Conditions		Final Density	Phase Compositions (wt%)		
	Crystallization	Sintering	(% TD)	$LiTi_2(PO_4)_3$	$AlPO_4$	TiO_2
LATSP	690 °C, 1 h	1200 °C, 1 h	93±1	91±0.5	7±0.2	2±0.5
LATSP+5%	680 °C, 1 h	1180 °C, 1 h	94±1	91±0.7	7±0.5	2±0.4
LATSP+10%	660 °C, 1 h	1140 °C, 1 h	94±1	92±0.4	5±0.9	3±0.6

Table **5.4** summarizes heating conditions, final densities, and phase compositions of the sintered pellets. Phase compositions were determined by Rietveld refinement using reference files listed in Figure **5.10**.

Sintering temperatures were reduced by 20° and 60 °C for LATSP+5% and LATSP+10% pellets respectively, compared to LATSP. The final pellet densities were all ~94 %TD, as measured by the Archimedes method. The presence of secondary phases was ignored in these calculations. Longer dwell times or higher temperatures than listed in Table **5.4** reduced observed densities by 1-3 %. These density decreases may be ascribed to the volatility of Li_2O at higher temperatures which promotes formation of secondary phases such as $AlPO_4$ and TiO_2.[54]

It is rather strange to see similar amounts of $AlPO_4$ and TiO_2 even when excess lithium is introduced since one would expect it to form $LiTi_2(PO_4)_3$ by reacting with $AlPO_4$ and TiO_2, hence reducing secondary phase contents. One possible explanation is that the excess Li_2O resides in grain boundaries such that there is a diffusive path, and more of it is lost at lower temperatures compared to stoichiometric samples. The phase compositions of all samples are quite the same, indicating that most of the excess lithium evaporates during sintering.

Table 5.5. Lattice parameters of LATSP, $LiTi_2(PO_4)_3$, and $Li_{1.3}Al_{0.3}Ti_{1.7}(PO_4)_3$.

Sample	a (Å)	c (Å)
LATSP	8.5137(3)	20.8529(8)
$LiTi_2(PO_4)_3$[a]	8.512	20.858
$Li_{1.3}Al_{0.3}Ti_{1.7}(PO_4)_3$[a]	8.5	20.82

a= ref. 25

The LATSP theoretical density is 2.93 g cm^{-3}, as calculated using the Table **5.5** refined lattice parameters. Refinement was done by whole pattern fitting and Rietveld refinement with Jade software using Si (PDF# 98-000-0396) as an internal standard. Table **5.5** compares the lattice parameters of LATSP with those of $LiTi_2(PO_4)_3$ and $Li_{1.3}Al_{0.3}Ti_{1.7}(PO_4)_3$. The differences in ionic radii of Al^{3+}(0.535 Å), Ti^{4+}(0.605 Å), Si^{4+}(0.26 Å), and P^{5+}(0.17 Å) explain the changes in lattice parameters.[55] The lattice constants for $Li_{1.3}Al_{0.3}Ti_{1.7}(PO_4)_3$ are smaller than for $LiTi_2(PO_4)_3$ since

smaller ionic radius Al^{3+} substitutes for Ti^{4+}, and LATSP has larger lattice parameters compared to $Li_{1.3}Al_{0.3}Ti_{1.7}(PO_4)_3$ due to substitution of P^{5+} by larger ionic radius Si^{4+}.

5.3.2.3. Microstructures

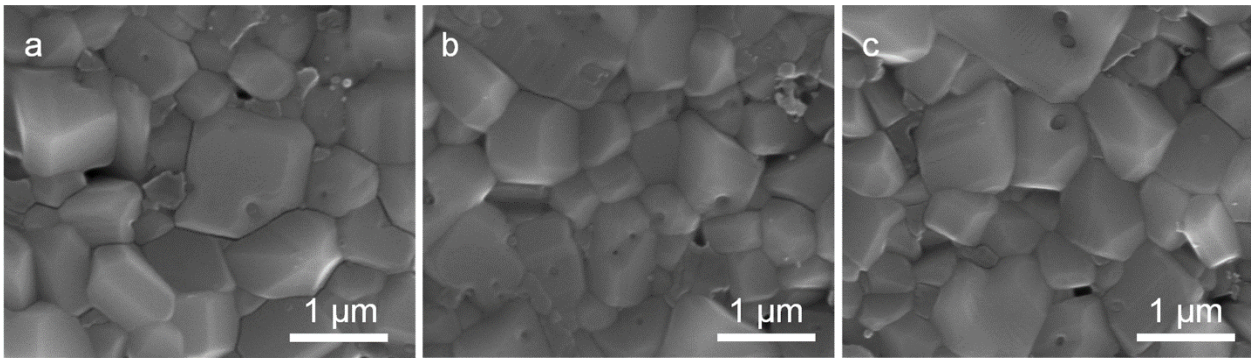

Figure 5.11. Polished and thermally etched pellet surfaces of a. LATSP, b. LATSP+5%, and c. LATSP+10%.

Figure **5.11** provides the microstructures for samples sintered to the highest densities per Table **5.4**. Average grain sizes (AGSs) determined by the linear intercept method are 625±230, 590±180, and 610±210 nm for LATSP, LATSP+5% and LATSP+10%, respectively. All samples have very similar AGSs despite being sintered at different temperatures. This suggests that densification and grain growth are triggered at lower temperatures with the addition of excess Li_2O. Li_2O thus must act as sintering aid for this material as it is the only variable among three powders.

5.3.2.4. Ionic conductivities

Figure **5.12** provides a representative Nyquist plot of sintered LATSP pellets at 25 °C. A depressed semicircle is observed at high frequencies followed by an inclined spike at lower frequencies. The semicircle is due to the sample's ionic conductivity, and inclined spike to polarization of ion blocking electrodes.[56] While it is agreed that the semicircle corresponding to the grain resistance is not identifiable at room temperature for high conductivity materials as only one semicircle is present, some researchers argue that the left intercept of the semicircle with the

real axis (Z') is grain resistance (R_g) and the diameter of the semicircle is the grain boundary resistance (R_{gb}).[26,31,32,35,57-59] In contrast, others claim the left intercept is the circuit resistance external to the sample and the diameter of the semicircle is the total resistance ($R_t = R_g + R_{gb}$).[37,60-63] Although the interpretations conflict, identical equivalent circuits are used for fitting, which was adopted here.

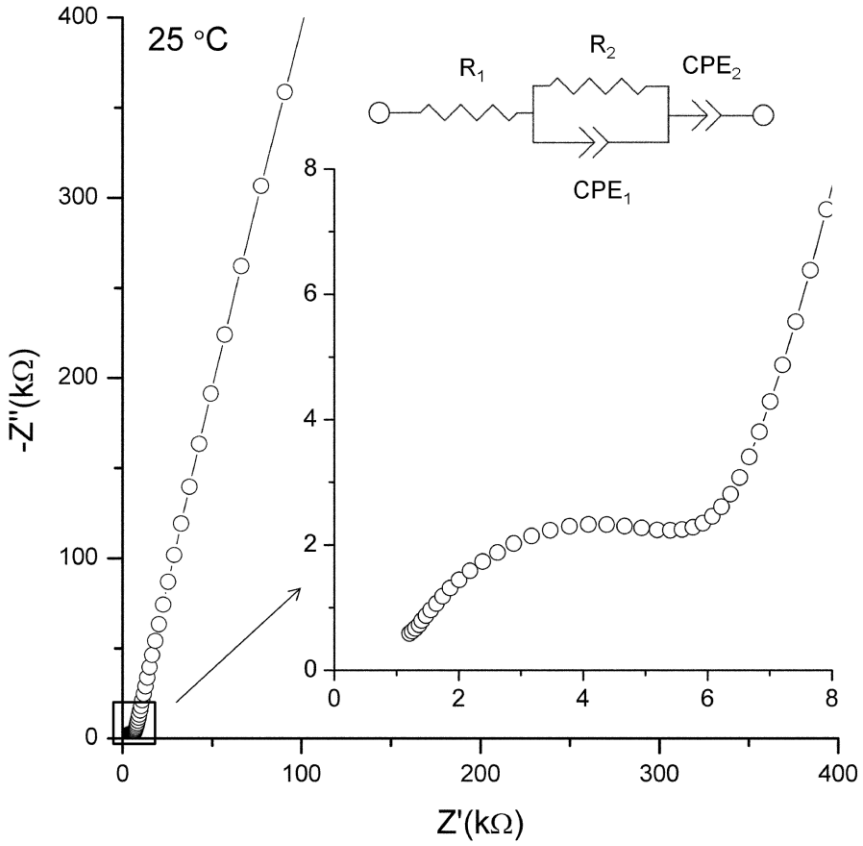

Figure 5.12. Representative Nyquist plot for LATSP at 25 °C. Equivalent circuit used for fitting is presented. Inset shows high frequency region.

For the current study, since the left intercept was fairly small compared to the right intercept, the right intercept was taken as the total resistance as a conservative estimate. The equivalent circuit, presented in Figure **5.12**, was used to estimate total resistances. A single resistor (R_1) was used for the left intercept; a resistor (R_2) in parallel with a constant phase element (CPE_1) for the

diameter of semicircle; and a constant phase element (CPE_2) for electrode polarization[41,56,57,60,64,65] The total resistances were calculated as $R_1 + R_2$.

Figure **5.13** depicts typical Nyquist plots of sintered LATSP pellets at 65° and 125 °C. At 65 °C, the semicircle is still identifiable although the diameter has greatly diminished compared to that at 25 °C. Only a short arc is seen at 125 °C.

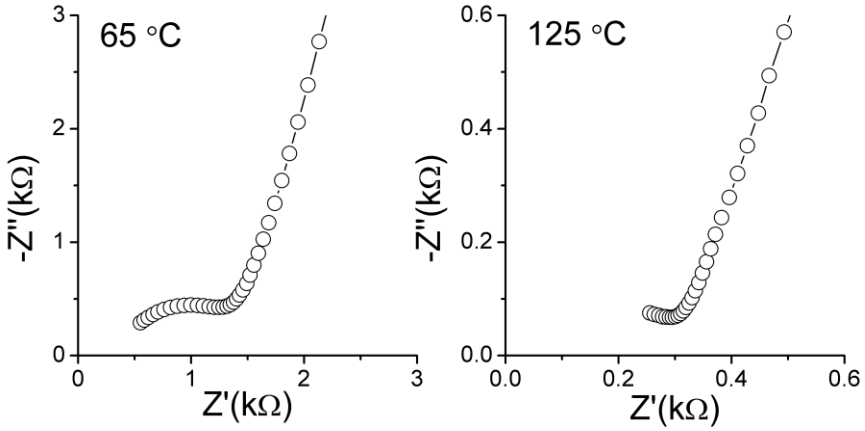

Figure 5.13. Representative Nyquist plots for LATSP at a. 65°, and b. 125 °C. The high frequency regions are shown.

Table **5.6** presents conductivities at 25 °C and above. At 25 °C, all samples show conductivities superior to 1 mS cm^{-1}. The LATSP conductivity reported here, 2.4 ($\pm$0.1) mS cm^{-1}, is about three times 0.77 ($\pm$0.15) mS cm^{-1}, the highest value obtained in the preliminary studies. The major difference is the powder processing and cold isostatic pressing of the green pellets which eventually results in higher sintered densities. As a comparison, LATSP pellets sintered at 1100°C for 1 h in the LATSP focused studies were 88$\pm$1 %TD dense, whereas those sintered under identical heating conditions in the preliminary studies were 80$\pm$1 %TD.

Table 5.6. Total conductivities (σ_t) of LATSP samples at selected temperatures.

T (°C)	σ_t (S cm^{-1})		
	LATSP	LATSP+5%	LATSP+10%
25	2.4×10^{-3}	2.9×10^{-3}	2.1×10^{-3}
45	5.5×10^{-3}	6.6×10^{-3}	4.9×10^{-3}
65	1.1×10^{-2}	1.3×10^{-2}	1.0×10^{-2}
85	2.0×10^{-2}	2.2×10^{-2}	1.9×10^{-2}
105	3.3×10^{-2}	3.4×10^{-2}	3.1×10^{-2}
125	5.1×10^{-2}	5.4×10^{-2}	4.9×10^{-2}

The total conductivities are on the order of 10 mS cm^{-1} at and above 65 °C, higher than the organic electrolyte conductivities at ambient. For example, $LiClO_4$ and $LiPF_6$ dissolved in organic solvents can have conductivities of 8.4 mS cm^{-1} and 11 mS cm^{-1} at 25 °C, respectively.[21] Temperatures near 65 °C are reached easily during battery operations as testified by the numerous built-in safety measures in organic electrolyte lithium batteries designed to limit temperature rises beyond 60 °C, which sometimes fail and result in permanent degradation or thermal runaway caused by electrolyte decomposition and electrode/electrolyte reactions.[12,21]

On another note, one can easily imagine batteries operating at 60-100 °C for HEV/EV/ESS applications due to the large battery volumes, hence, exhibiting lower thermal dissipation compared to small battery packs. Overall, LATSP seems to offer excellent potential for replacing organic electrolytes due to its high conductivities and much improved safety. Also, the low coefficients of thermal expansion (CTE) of LATP materials (7-11 ppm °C^{-1})[35] suggests easier structural design of batteries compared to those using polyethylene oxide based polymer electrolytes (120 ppm °C^{-1})[66] as the volume change during use at a range of temperature becomes less of a concern.

Figure **5.14** shows selected temperature dependent measurements of Li^+ ionic conductivities for all LATSP samples. Each plot exhibits an Arrhenius dependence. Conductivities at each temperature are within the error limits of each other such that no clear argument can be made on

which exhibits higher conductivities. The activation energies derived from the slope of the Arrhenius plots are tabulated in Table **5.7**. The Li^+ diffusion mechanism is the same for all samples as there is no noticeable difference in activation energies. Conductivities and activation energies are comparable to those reported by Fu with similar compositions.[40]

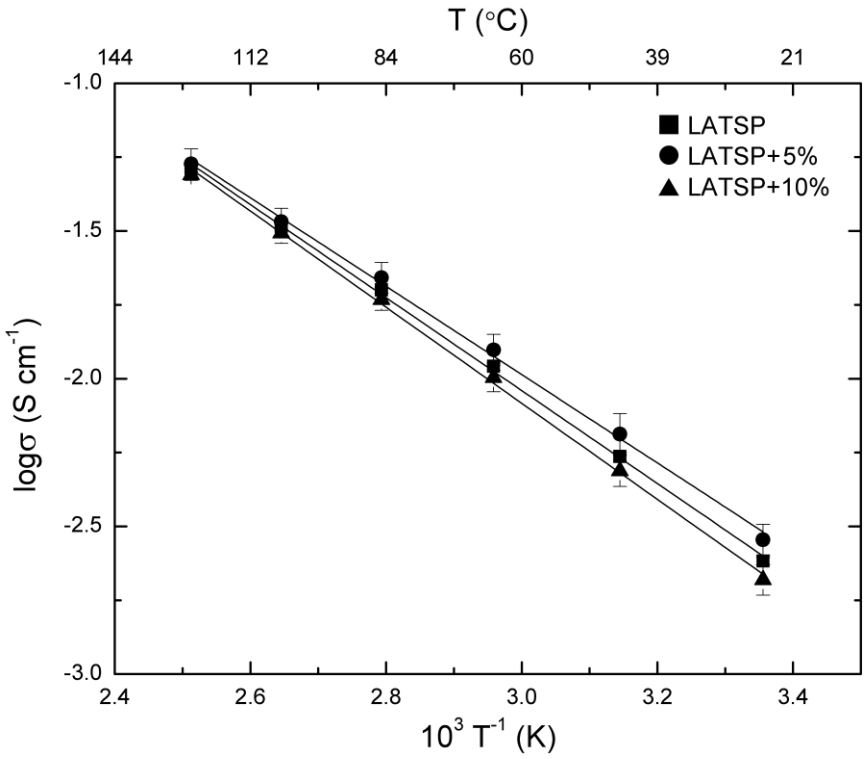

Figure 5.14. Arrhenius plots of LATSP, LATSP+5%, and LATSP+10%.

Table 5.7. Activation energies of LATSP, LATSP+5%, and LATSP+10%.

Sample	E_a (σ_t) (kJ mol^{-1})
LATSP	30.1±0.3
LATSP+5%	28.6±0.3
LATSP+10%	31.1±0.8

5.3.3. Thin film processing

Initial efforts were made to produce thin films that might offer similar properties in real devices given that commercially available solid membranes are 100-300 μm thick.

5.3.3.1. Green film analyses

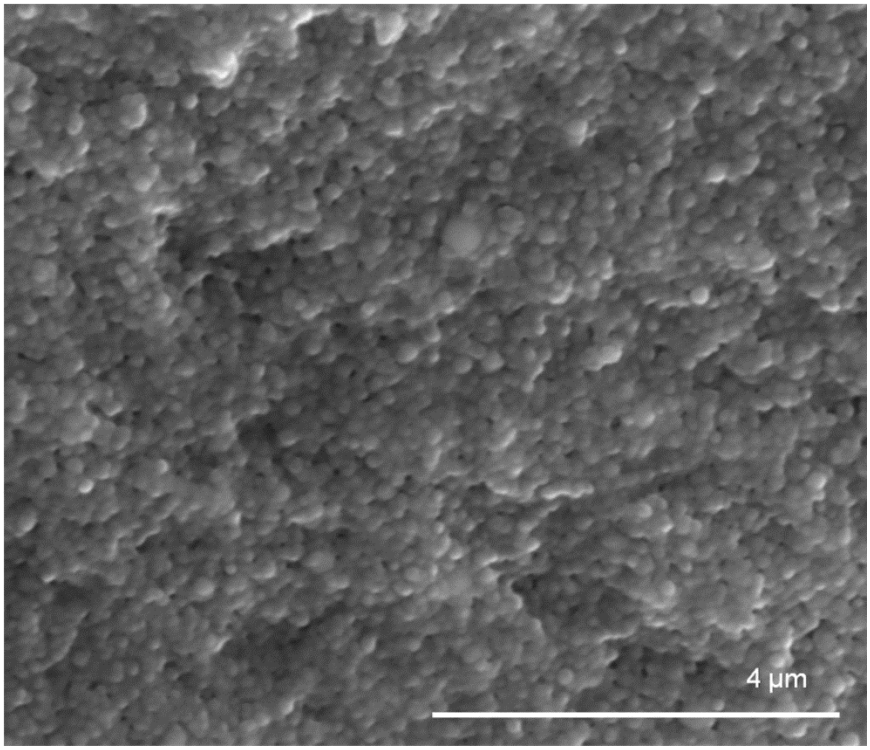

Figure 5.15. SEM fracture surface image of green film.

In the Figure **5.15** SEM fracture surface image of a green film, the LATSP+5% nanopowders seem to be well dispersed in the polymeric host. Obtaining crack free, green films using nanopowders is not an easy task. In general, high solids loadings of suspensions is preferential to minimize defect formation while drying the cast film. However, because nanopowder surfaces interact quite strongly with solvent, excess solvent is needed compared to micron size particles.

One way of improving solids loadings is to start with low viscosity solvents.[67,68] For that matter, mixed solvent systems of ethanol/toluene, ethanol/xylene, and ethanol/methyl ethyl ketone are

commonly used in tape casting. LATSP+5% does not disperse in toluene or xylene. Hence, an ethanol/methylethyl ketone system at a volume ratio of 20/80 was used to obtain crack free, green films on drying.

Another method of reducing viscosity, thereby increasing solids loading for a given suspension, is to add dispersants.[62,63,69,70] Polyacrylic acid at 3 wt % with respect to powder mass, was used in the current studies. Optimal dispersant and solvent volume ratios were determined empirically.

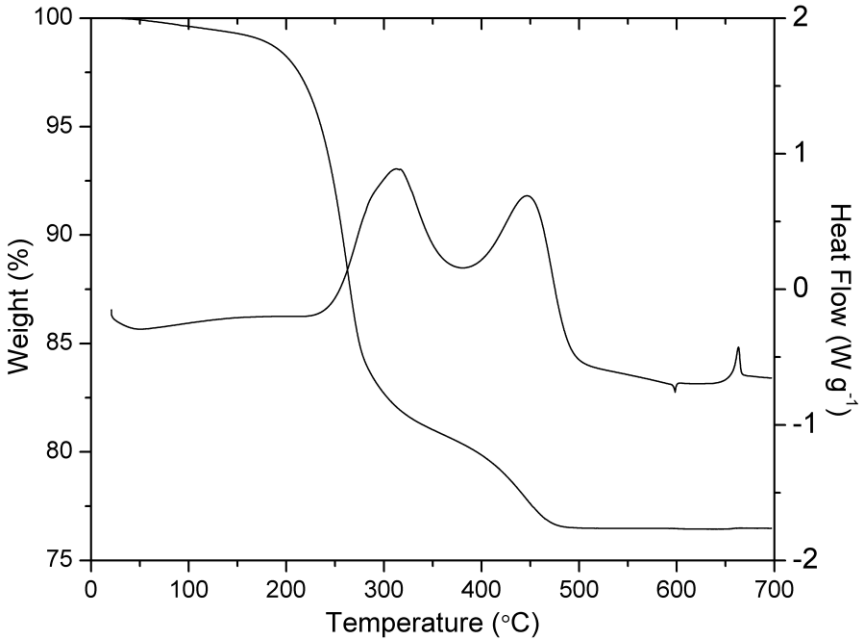

Figure 5.16. TGA/DSC of green film.

From Table **5.1**, the ceramic yields of processed green films is 77 wt% (57 vol%), excluding solvent as it evaporates on drying. The Figure **5.16** TGA/DSC shows the green film to have a ceramic yield identical to theory. Two exotherms are seen accompanied by mass losses at intermediate temperatures from decomposition of polymeric additives: polyacrylic acid, benzylbutyl phthalate, and polyvinyl butyral. The mass loss ceases at ~500 °C and a $LiTi_2(PO_4)_3$

crystallization exotherm is observed at 662 °C, consistent with as-produced powder analyses in Figure **5.9**. The endotherm spike at 600 °C is due to a change in ramp rate.

5.3.3.2. Sintered film analyses

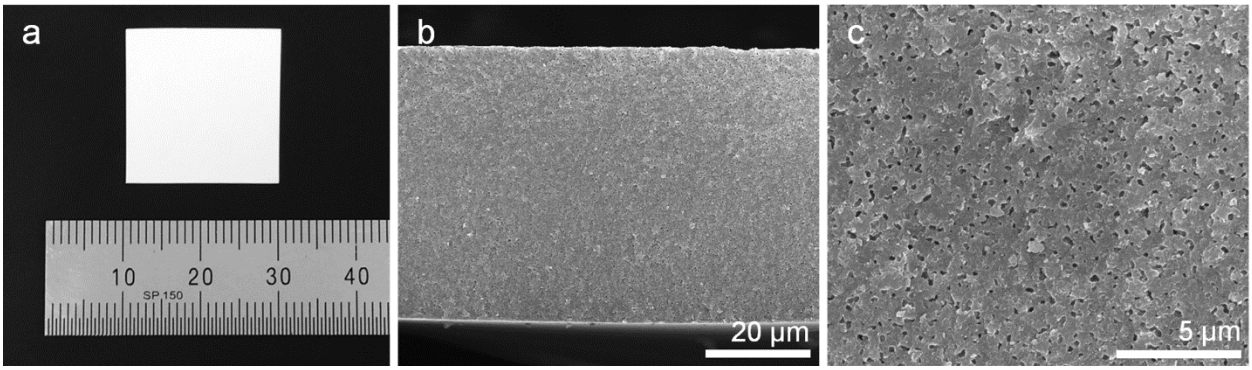

Figure 5.17. a. optical and b./c. SEM fracture surface images of sintered film.

Sintering temperatures were limited to 1000 °C as higher temperatures caused films to sinter onto alumina plates used as substrates. Figure **5.17** shows optical and SEM fracture surface images of a film sintered to 1000 °C / 1 h. The film thickness is 52±1 µm. Pores are observed in the microstructure indicating % TD is lower compared to the above described pellet samples. Sintered films offer densities of 88±1 % of theory, roughly 6 % lower than pellets sintered at optimal sintering schedules per above. This is expected as optimal sintering conditions as specified in Table **5.4** could not be adopted for thin film sintering as a consequence of adhesion to substrates.

Figure **5.18** provides an XRD of a sintered film. All major peaks correspond to $LiTi_2(PO_4)_3$. Small amounts of $AlPO_4$ and TiO_2 secondary phases are present.

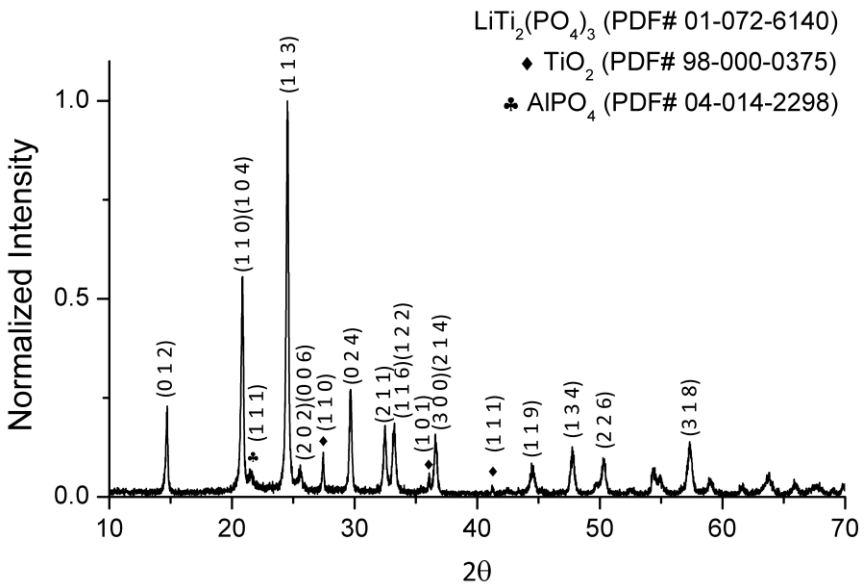

Figure 5.18. XRD pattern of films sintered at 1000 °C/1 h. Peaks with no label correspond to $LiTi_2(PO_4)_3$.

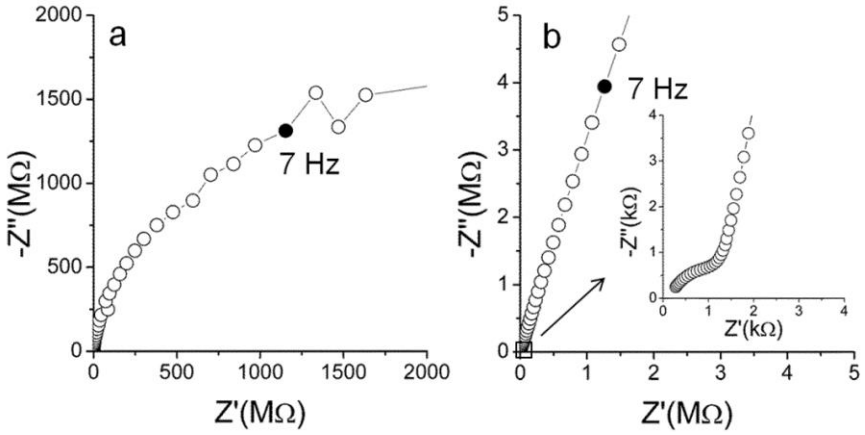

Figure 5.19. Nyquist plots of a. as-sintered, and b. surface ground films.

Figure **5.19** presents a typical Nyquist plot for sintered films at 25 °C. The Nyquist plot of the as-sintered films shows what seems to be a portion of a semicircle. We suspect this is due to mild deposition of alumina onto the film, thereby reducing the effective electrode area when sputter coated. Note that the total resistance is inversely proportional to the electrode area if the total conductivity is fixed. Furthermore, with the film sintering onto the alumina substrate at higher

temperatures, it is reasonable to assume mild deposition at 1000 °C. After gently grinding the surface of the sintered films with 1200 grit SiC paper, the impedance behavior becomes very different per Figure **5.19b**, thereby proving there are unwanted impurities on the as-sintered film surfaces.

Table 5.8. Reported room temperature conductivities for NASICON structured membranes.

	Processing Step	σ_t(S cm^{-1})	Thickness(μm)	Reference
LATSP+5%	LF-FSP/TC	4.3×10^{-4}	52	-
OHARA Inc. LATP	GC/P	1×10^{-4}	150	57,72
$Li_{1.3}Al_{0.3}Ti_{1.7}(PO_4)_3$	GC/BM/TC	1.8×10^{-4}	40	38
$Li_{1.4}Al_{0.4}Ge_{1.6}(PO_4)_3$	SG/C/TC	3.4×10^{-4}	75	59
$Li_{1.4}Al_{0.4}Ge_{1.6}(PO_4)_3$	SG/C/TC	8.4×10^{-4}	200	71
$Li_{1.5}Al_{0.5}Ge_{1.5}(PO_4)_3$	GC/BM/TC	6.4×10^{-4}	200	36

GC = glass-ceramic, SG = sol-gel, C = calcination, BM = ball-milling, TC = tape casting, P = polishing

The obtained total conductivities of surface ground films are 0.43 ($\pm$0.14) mS cm^{-1} at ambient, fairly low compared to pellet conductivities (> 1 mS cm^{-1}). This can mainly be attributed to lower final densities of 88%TD. Table **5.8** compares thicknesses and room temperature conductivities of LATSP films to commercially available products and to what other groups have reported. The total conductivity of LATSP+5% film is comparable to other values listed in Table **5.8**. Note all films below 100 μm were tape cast. Glass-ceramic sheets were ball-milled to obtain feedstock for tape casting.[36,38] A sol-gel processing study required calcination for complete reaction resulting in aggregates that necessitated high energy mechanical milling before or during suspension formulation to break them down.[59,71] Only LF-FSP alone provides nanopowders that can be directly used for tape casting when producing thin films (<100 μm). LAGP materials which Ge is

substituting Ti of LATP show high conductivities but may not be suitable for commercialization due to the high cost of Ge.

The optimization of film processing and sintering conditions to reach conductivities similar to those observed in pellet samples at 1 mS cm^{-1} remains as future work. Increasing the solids loading of green film hence starting with a higher % TD, extending sintering time, sintering in a Li_2O vapor environment or using different substrates during sintering are under exploration. Mechanical strength and cyclic voltammetry of such films will be measured as well.

5.4. Conclusions

$Li_{1.7}Al_{0.3}Ti_{1.7}Si_{0.4}P_{2.6}O_{12}$ pellets showed the highest ionic conductivities of 0.77 ($\pm$0.15) mS cm^{-1} among the $Li_{1+x+y}Al_xTi_{2-x}Si_yP_{3-y}O_{12}$ (x = 0.1, 0.3/y = 0.2, 0.4) compositions in preliminary studies. Improving the green densities resulted in $Li_{1.7}Al_{0.3}Ti_{1.7}Si_{0.4}P_{2.6}O_{12}$ pellets with superionic conductivities of 2.4 ($\pm$0.1) mS cm^{-1} at room temperature when sintered. Adding 5 and 10 wt% of excess lithium lowered both crystallization points and sintering temperatures by 11$\pm$1 °C and 60$\pm$5 °C, respectively. However, no noticeable effects on the conductivities were observed.

Low activation energies (30 $\pm$ 1 kJ mol^{-1}), small grain sizes (600 $\pm$200 nm), high Li concentrations of 1.7, and high final densities (94 $\pm$ 1 %TD) combine to offer superionic conductivities in LATSP/LATSP+5%/LATSP+10% pellets. The obtained room temperature conductivities are comparable to the superionic conductivities reported by glass-ceramic processing method. High room temperature conductivities coupled with conductivities of 10 mS cm^{-1} only at 60 °C suggests LATSP to be an excellent candidate material for replacing organic liquid electrolytes, thereby improving safety as well.

Initial thin film processing studies using LF-FSP nanopowders were successful, proving their direct utility for tape casting, unlike glass-ceramic or sol-gel processing methods. Obtained thin film conductivities of 0.43 ($\pm$0.14) mS cm^{-1} are comparable to what other groups have reported with similar materials per Table **5.8**. The conductivity disparities between the films and the pellets are ascribed to films' lower final densities (88$\pm$1 %TD) vs 94±1 % in the pellets. Future work remains to match the film conductivities seen for pellets.

The work presented here strongly suggests that the materials and thin films made from them offer excellent potential to supplant liquid electrolytes in a wide variety of Li based batteries. Furthermore, ceramics have very high tolerance to heat suggesting safety at higher operating temperatures offering superior charge/discharge rates, as failure mechanisms common to liquid electrolytes are not present.

References

1. P. G. Bruce, B. Scrosati and J.-M. Tarascon, *Angew. Chem. Int. Ed*., 2008, **47**, 2930-2946.

2. J.-M. Tarascon and M. Armand, *Nature*, 2001, **414**, 359-367.

3. M. Armand and J.-M. Tarascon, *Nature*, 2008, **451**, 652-657.

4. K. M. Abraham, *Electrochim. Acta*, 1993, **38**, 1233-1248.

5. B. Scrosati and J. Garche, *J. Power Sources*, 2010, **195**, 2419-2430.

6. M.-K. Song, S. Park, F. M. Alamgir, J. Cho and M. Liu, *Materials Science and Engineering R*, 2011, **72**, 203-252.

7. T.-H. Kim, J.-S. Park, S.-K. Chang, S. Choi, J. H. Ryu and H.-K. Song, *Adv. Energy Mater*., 2012, **2**, 860-872.

8. B. Scrosati, J. Hassoun and Y.-K. Sun, *Energy Environ. Sci*., 2011, **4**, 3287-3295.

9. J. W. Fergus, *J. Power Sources*, 2010, **195**, 4554-4569.

10. U. V. Sacken, E. Nodwell, A. Sundher and J. R. Dahn, *Solid State Ionics*, 1994, **69**, 284-290.

11. S.-I. Tobishima and J.-I. Yamaki, *J. Power Sources*, 1999, **81-82**, 882-886.

12. P. G. Balakrishnan, R. Ramesh and T. P. Kumar, *J. Power Sources*, 2006, **155**, 401-414.

13. S. S. Zhang, *J. Power Sources*, 2007, **164**, 351-364.

14. T. D. Hatchard, D. D. MacNeil, D. A. Stevens, L. Christensen and J. R. Dahn, *Electrochem. Solid-State Lett*., 2000, **3**, 305-308.

15. M. A. Gee and F. C. Laman, *J. Electrochem. Soc*., 1993, **140**, L53-L55.

16. W. H. Meyer, *Adv. Mater*., 1998, **10**, 439-448.

17. F. Groce, G. B. Appetecchi, L. Persi and B. Scrosati, *Nature*, 1998, **394**, 456-458.

18. Y. Sun, *Nano Energy*, 2013, **2**, 801-816.

19. N. Anantharamulu, K. K. Rao, G. Rambabu, B. V. Kumar, V. Radha and M. Vithal, *J. Mater. Sci*., 2011, **46**, 2821-2837.

20. J. T. Dudley, D. P. Wilkinson, G. Thomas, R. LeVae, S. Woo, H. Blom, C. Horvath, M. W. Juzkow, B. Denis, P. Juric, P. Aghakian and J. R. Dahn, *J. Power Sources*, 1991, **35**, 59-82.

21. K. Xu, *Chem. Rev*., 2004, **104**, 4304-4417.

22. G. Nuspl, T. Takeuchi, A. Weiß, H. Kageyama, K. Yoshizawa and T. Yamabe, *J. Appl. Phys*., 1999, **86**, 5484-5491.

23. L.-O. Hagman and P. Kierkegaard, *Acta Chem. Scand*., 1968, **22**, 1822-1832.

24. A. Aatiq, M. Ménétrier, L. Croguennec, E. Suard and C. Delmas, *J. Mater. Chem*., 2002, **12**, 2971-2978.

25. H. Aono, E. Sugimoto, Y. Sadaoka, N. Imanaka and G.-Y. Adachi, *J. Electrochem. Soc*., 1990, **137**, 1023-1027.

26. D. Popovici, H. Nagai, S. Fujishima and J. Akedo, *J. Am. Ceram. Soc*., 2011, **94**, 3847-3850.

27. K. Arbi, S. Mandal, J. M. Rojo and J. Sanz, *Chem. Mater*., 2002, **14**, 1091-1097.

28. J. Fu, *Solid State Ionics*, 1997, **96**, 195-200.

29. C.-M. Chang, Y. I. Lee and S.-H. Hong, *J. Am. Ceram. Soc*., 2005, **88**, 1803-1807.

30. M. Forsyth, S. Wong, K. M. Nairn, A. S. Best, P. J. Newman and D. R. MacFarlane, *Solid State Ionics*, 1999, **124**, 213-219.

31. Z. Wen, X. Xu and J. Li, *J. Electroceram*., 2009, **22**, 342-345.

32. X. Xu, Z. Wen, X. Yang, J. Zhang and Z. Gu, *Solid State Ionics*, 2006, **177**, 2611-2615.

33. S. Wong, P. J. Newman, A. S. Best, K. M. Nairn, D. R. MacFarlane and M. Forsyth, *J. Mater. Chem*., 1998, **8**, 2199-2203.

34. P. Maldonado-Manso, E. R. Losilla, M. Martínez-Lara, M. A. G. Aranda, S. Bruque, F. E. Mouahid and M. Zahir, *Chem. Mater*., 2003, **15**, 1879-1885.

35. S. D. Jackman and R. A. Cutler, *J. Power Sources*, 2012, **218**, 65-72.

36. J. S. Thokchom, N. Gupta and B. Kumar, *J. Electrochem. Soc*., 2008, **155**, A915-A920.

37. B. Kumar, D. Thomas and J. Kumar, *J. Electrochem. Soc*., 2009, **156**, A506-A513.

38. L. Puech, C. Cantau, P. Vinatier, G. Toussaint and P. Stevens, *J. Power Sources*, 2012, **214**, 330-336.

39. J. S. Thokchom and B. Kumar, *J. Electrochem. Soc*., 2007, **154**, A331-A336.

40. J. Fu, *J. Am. Ceram. Soc*., 1997, **80**, 1901-1903.

41. P. Johnson, N. Sammes, N. Imanishi, Y. Takeda and O. Yamamoto, *Solid State Ionics*, 2011, **192**, 326-329.

42. S. Li, C. Xian, K. Yang, C. Sun, Z. Wang and L. Chen, *J. Power Sources*, 2012, **205**, 57-62.

43. J. D. Nicholas and L. C. De Jonghe, *Solid State Ionics*, 2007, **178**, 1187-1194.

44. S. Le, S. Zhu, X. Zhu and K. Sun, *J. Power Sourc*es, 2013, **222**, 367-372.

45. A. C. Sutorik, S. S. Neo, D. R. Treadwell and R. M. Laine, *J. Am. Ceram. Soc*., 1998, **81**, 1477-1486.

46. R. Baranwal, M. P. Villar, R. Garcia and R. M. Laine, *J. Am. Ceram. Soc*., 2001, **84**, 951-961.

47. C. R Bickmore, K. F. Waldner, R. Baranwal, T. Hinklin, D. R. Treadwell and R. M. Laine, *J. Eur. Ceram. Soc*., 1998, **18**, 287-297.

48. J. Marchal, T. John, R. Baranwal, T. Hinklin and R. M. Laine, *Chem. Mater*., 2004, **16**, 822-831.

49. T. Hinklin, B. Toury, C. Gervais, F. Babonneau, J. J. Gislason, R. W. Morton and R. M. Laine, *Chem. Mater*., 2004, **16**, 21-30.

50. A. S. Bondarenko, G. A. Ragoisha in: A. L. Pomerantsev (Eds.), Progress in Chemometrics Research, Nova Science Publishers, New York, 2005, pp. 89–102. (the program is available online at http://www.abc.chemistry.bsu.by/vi/analyser/)

51. J. S. Thokchom and B. Kumar, *Solid State Ionics*, 2006, **177**, 727-732.

52. K. Nagata, T. Nanno, *J. Power Sources*, 2007, **174**, 832-837.

53. B. Key, D. J. Schroeder, B. J. Ingram and J. T. Vaughey, *Chem. Mater*., 2012, **24**, 287-293.

54. C. R. Mariappan, C. Yada, F. Rosciano and B. Roling, *J. Power Sources*, 2011, **196**, 6456-6464.

55. R. D. Shannon, *Acta Crystallogr*., 1976, **A32**, 751-767.

56. P. G. Bruce and A. R. West, *J. Electrochem. Soc*. 1983, **130**, 662-669.

57. N. Imanishi, S. Hasegawa, T. Zhang, A. Hirano, Y. Takeda and O. Yamamoto, *J. Power Sources*, 2008, **185**, 1392-1397.

58. K. Kim, J. Kim, Y. Yoon and D. Shin, *Met. Mater. Int*., 2014, **20**, 189-194.

59. M. Zhang, Z. Huang, J. Cheng, O. Yamamoto, N. Imanishi, B. Chi, J. Pu and J. Li, *J. Alloys Compd*., 2014, **590**, 147-152.

60. H. S. Jadhav, M-S. Cho, R. S. Kalubarme, J.-S. Lee, K.-N. Jung, K.-H. Shin and C-.J. Park, *J. Power Sources*, 2013, **241**, 502-508.

61. C. R. Mariappan, M. Gellert, C. Yada, F. Rosciano and B. Roling, *Electrochem. Commun*., 2012, **14**, 25-28.

62. J. S. Thokchom and B. Kumar, *J. Power Sources*, 2008, **185**, 480-485.

63. J. S. Thokchom and B. Kumar, *J. Power Sources*, 2010, **195**, 2870-2876.

64. Y. Deng, S.-J. Shang, A. Mei, Y.-H. Lin, L.-Y. Liu and C.-W. Nan, *J. Alloys Compd*., 2009, **472**, 456-460.

65. A. Mei, X.-L. Wang, Y.-C. Feng, S.-J. Zhao, G.-J. Li, H.-X. Geng, Y.-H. Lin and C.-W. Nan, *Solid State Ionics*, 2008, **179**, 2255-2259.

66. Y. Rao and T. N. Blanton, *Macromolecules*, 2008, **41**, 935-941.

67. V. Vinothini, P. Singh and M. Balasubramanian, *J. Mater. Sci*., 2006, **41**,7082-7087.

68. S. Bhaskar Reddy, P. Paramanano Singh, N. Raghu and V. Kumar, *J. Mater. Sci*., 2002, **37**, 929-934.

69. A. K. Maiti and B. Rajender, *Mater. Sci. Eng. A*, 2002, **333**, 35-40.

70. E. Yi, J. C. Furgal, J. Azurdia and R. M. Laine, *J. Mater. Chem. A*, 2014, **2**, 3766-3775.

71. M. Zhang, K. Takahashi, I. Uechi, Y. Takeda, O. Yamamoto, D. Im, D.-J. Lee, B. Chi, J. Pu, J. Li and N. Imanishi, *J. Power Sources*, 2013, **235**, 117-221.

72. T. Zhang, N. Imanishi, S. Hasegawa, A. Hirano, J. Xie, Y. Takeda, O. Yamamoto and N. Sammes, *Electrochem. Solid-State Lett.*, 2009, **12**, A132-A135.

Chapter 6

Processing Al:LLZO free standing thin films

6.1. Introduction

Lithium ion batteries (LIBs) continue to power modern society.[1,2] However, newly emerging applications that require bulk battery systems or low temperature operation mandate new battery designs, electrochemistries, and materials to meet target performance specifications.[3,4] Multiple next generation Li battery designs have been proposed that offer 2-10x higher energy storage per mass or volume compared to current LIBs, all using Li anodes due to its high theoretical capacity (3860 mAh g^{-1}).[3,5] In terms of electrolytes, common commercial LIBs use lithium salts dissolved in organic carbonate liquids.[6] However, such electrolytes suffer from multiple drawbacks including narrow operating windows based on thermal and electrochemical stability.[7] They also suffer from poor performance below ambient, and typically degrade at ≥ 60 °C requiring the use of thermal management peripherals to avoid catastrophic failure.[8] Furthermore, the potential utility of different anode and cathode materials in prototypical next generation Li batteries is complicated by compatibility issues with selected cell chemistries resulting in decomposition or reaction.[4,9]

To this end, ceramic electrolytes[10] with ionic conductivities similar to liquid/separator couples[6] (0.1-1 mS cm^{-1}) are proposed to replace liquid electrolytes to further improve and/or stabilize cell

chemistries while also reducing the cell footprint by eliminating the peripherals.[9] Ceramic Li^+ superionic conductors are a class of materials that exhibit high Li^+ ionic conductivities but low electronic conductivities. Surprisingly, ceramics with selected crystal structures show very high ionic conductivities, similar to those of liquid counterparts despite offering a rigid skeletal structure, as they possess low activation energy conduction paths, i.e. an ion conduction highway.[11,12] Oxides with garnet, perovskite, and NASICON structures in particular have been engineered over the past several decades to alter ion conduction properties by partially or fully substituting parent elements with aliovalent ions to modify Li^+ site vacancy concentration, conduction channel width, and crystallographic site occupancy.[13,14] In a broader perspective, grain boundary properties have also been engineered by introducing secondary functional phases or by optimizing processing and sintering conditions to minimize grain boundary resistance arising from polycrystallinity.[13,14] Efforts to optimize grain and grain boundary properties have led to a greater understanding of these materials resulting in high ionic conductivities of 0.1-1 mS cm^{-1}.[15,16] However, additional qualifications surface when these have to be incorporated into a cell, such as Li metal stability, thin film form-ability, and ease of processing.

Immense attention has been given to c-LLZO as it exhibits a combination of desirable characteristics as noted above.[13,17] In particular, due to higher safety standards required for bulk battery systems, recent interest has grown in incorporating c-LLZO in all-solid-state lithium batteries (ASLBs) to construct inherently safe cells, concomitantly obviating safety mechanisms related to LIBs.[8] It may also be useful in assembling aqueous Li cells as it shows structural stability over a wide pH range.[17] Indeed, a recent ARPA-E FOA indicates considerable need for c-LLZO electrolyte films < 20 μm thick.[18] Strangely, despite the interest, most prototype cells use relatively thick Li phosphate membranes (50-200 μm)[9] which require Li stable interfacial buffer layers to

prevent reduction by Li metal.[5,9] Net ionic conductivities at these thicknesses are far from optimal and reduce their potential utility in Li batteries for bulk storage applications.

In order for c-LLZO to be used in actual cells, it must be incorporated in thin film forms preferably < 50 μm.[19] However, no dense, thin c-LLZO films with ionic conductivities equivalent to those found in high density, bulk counterparts (> 0.1 mS cm^{-1}) have been reported to date likely due to the energy intensive and rather problematic sintering processes involved (Table **6.1**, Figure **6.1**).[20-32] Conventional sintering of c-LLZO requires 10-40 h of dwell at temperatures above 1100 °C. However, Li (as Li_2O) volatilizes rapidly at these temperatures presenting exceptional challenges in producing thin films given their much higher surface/volume ratios leading to faster Li loss.

Furthermore, repeated calcination and ball-milling to obtain powders for pellet compaction are also time and energy intensive. Pellets are covered in mother powder during sintering to reduce Li loss. In contrast, hot-pressing shortens the sintering time to 1 h at lower temperatures of 1000-1050 °C to result in near full densities with the aid of pressure. Note the powders used for hot-pressing are also ball-milled and calcined.

New constraints surface on transferring known approaches to forming thin films. First, mother powder cannot be used, since they will sinter to the films which will be difficult to remove without fracturing the film. For hot-press, the film may crack during sintering due to uneven pressure. Also, even if it is possible to sinter thin films in certain condition there are other limits; scalability, utility in shaping, cost.

While there are no reports of successful thin film formulation based on reported approaches so far, paths that would be taken if one were to translate reported methods to sintering films are compared in Figure **6.1**. Direct processing of LF-FSP made nanopowder provides a processing

short-cut while significantly reducing required external energy to reach high densities at the same time.

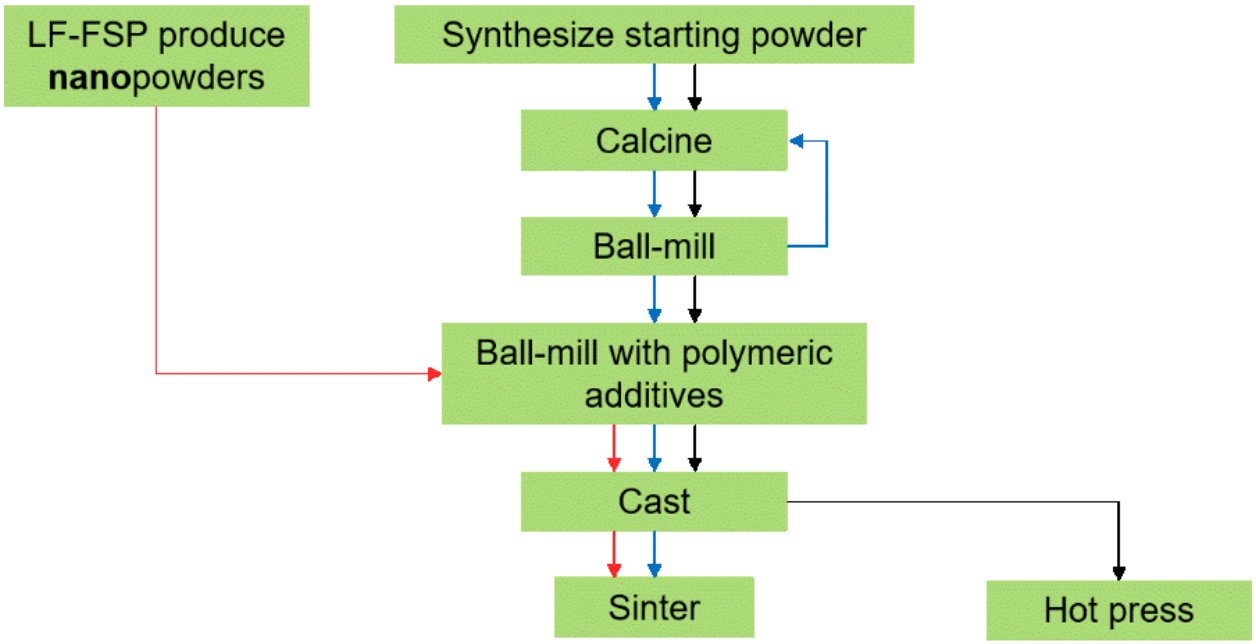

Figure 6.1. Comparison of potential processing routes.

Table 6.1. Reported sintering conditions and properties of c-LLZO {($Li_{7-2x-y}A_xLa_3Zr_{2-y}B_yO_{12}$, ($A^{3+}$, B^{5+})}.

	Dopant(s)	Sintering condition	% den-sity	RT Ionic conductivity (mS cm^{-1})	Remark	Ref.
Solid state reaction	n/a	1230 °C / 36 h / air	92	0.24	Likely Al^{3+} contamination from crucible. Covered in mother powder.	20
	Al^{3+}	1230 °C / 36 h / air	n/a	0.18	Covered in mother powder.	21
	Nb^{5+}	1200 °C / 36 h / air	92	0.8	n/a	22
	Ta^{5+}	1140 °C / 16 h / air	94	1.02	Covered in mother powder.	23
	Al^{3+}/Ta^{5+}	1140 °C / 9 h / O_2	96	0.74		24
	Al^{3+}	1100 °C / 12 h / air	92	0.25	Attrition milled (~1µm powder). Covered in mother powder.	25
Spray pyrolysis	Al^{3+}	1000 °C / 1 h / air	51	0.0044	Fully decomposed starting powder. Covered in mother powder.	26
Sol-gel	Al^{3+}	900 °C / (n/a) / air	n/a	0.0024	Sol-gel dip coating. Li_2CO_3 placed near to retard Li loss.	27
	Al^{3+}	1200 °C / 10 h / air	96	0.61 (33°C)	Li_4SiO_4 sintering additive. Covered in mother powder.	28
Co-precipitation	Nb^{5+}	1100 °C / 36 h / air	87	0.52	Covered in mother powder.	29
Pechini method	Al^{3+}	1200 °C / 6 h / air	92	0.2		30
Hot press	Ta^{5+}	1050 °C / 1 h / Ar / 62 MPa	98	0.82	Co-precipitation derived powder. No mother powder.	16
	Al^{3+}	1000 °C / 1 h / Ar / 40 MPa	96	0.4	Sol-gel derived powder. No mother powder.	31
	Al^{3+}	1000 °C / 1 h / Ar / 40 MPa	98	0.4	Solid state reaction derived powder. No mother powder.	32
Flame Spray Pyrolysis	Al^{3+}	1090 °C / 1 h / N_2	94	0.2	Fully decomposed starting powder. No mother powder.	This work

Multiple reports have assessed the materials' challenges in developing next generation Li batteries in terms of stability and compatibility.[4,33] However, one very important aspect is overlooked, i.e. material processing challenges. Unlike liquids or polymers, oxides require high temperature sintering of powders to reach the high densities needed for optimal performance. Thus,

the selection of starting powder(s), processing chemistries, and sintering conditions are all crucial to obtaining the highest possible densities at the lowest possible energy input (cost). Furthermore, processing becomes even more difficult when producing thin films.

Numerous attempts to minimize processing conditions of c-LLZO by introducing sintering aids[28] or using micron-[34] to nano-particles[26] have met with little success. In contrast, hot-pressing provides access to ≈ fully dense pellets with superior bulk ionic conducti-vities.[16,32,35] However, such an approach may be problematic from a commercialization standpoint. Hence, there remains considerable need to first, develop routes to c-LLZO thin films, and second, in a practical and economical way. Here we show a potential solution to both challenges by adopting two proven methods of mass production; flame spray pyrolysis and conventional casting-sintering.[36] Fumed silica, nano-titania, and carbon black are produced by combustion synthesis at kilotons/year quantities. Casting-sintering is one of the lowest cost processing routes that converts ceramic powders to free standing, dense monoliths. For example, a myriad of ceramic films or plates such as Al_2O_3, ZrO_2, Y:ZrO_2 and even $Li_{1.3}Al_{0.3}Ti_{1.7}(PO_4)_3$ Li^+ conductors are commercially produced. In particular, multi-layered ceramic capacitors are mass-produced by similar methods. Note that deposition[37] or sputter[38] derived c-LLZO films are not considered here as they may find use in 2-D thin film Li batteries but are unlikely to be useful for bulk battery systems.

6.2. Experimental

6.2.1. Precursor synthesis and powder production

Four types of precursors were synthesized in this study to serve as a source of Li, Al, La, and, Zr, respectively. Lithium propionate [$LiO_2CCH_2CH_3$] and alumatrane [$Al(OCH_2CH_2)_3N$] were synthesized as described elsewhere.[36] Lanthanum isobutyrate {$La[O_2CCH(CH_3)_2]_3$} was

synthesized by reacting lanthanum oxide (130 g, 0.4 mole) with isobutyric acid (530 g, 6 mole) in a 1 L round bottom flask equipped with a still head at 140 °C in N_2 atmosphere. Once transparent liquid was obtained, heat was removed and lanthanum isobutyrate crystallized on cooling which was filtered out. Zirconium isobutyrate $\{Zr[O_2CCH(CH_3)_2]_2(OH)_2\}$ was synthesized by reacting zirconium basic carbonate (86 g, 0.28 mole) with isobutyric acid (390 g, 4.4 mole) and isobutyric anhydride (350 g, 2.2 mole) in the same manner with lanthanum isobutyrate synthesis.

Nanopowders of $Li_{6.25}Al_{0.25}La_3Zr_2O_{12}$ composition with 50 wt. % excess lithium were synthesized by liquid-feed flame spray pyrolysis (LF-FSP). Extra lithium is intended to compensate for its loss during sintering. Lithium propionate, alumatrane, lanthanum isobutyrate, and zirconium isobutyrate were dissolved in ethanol at selected molar ratios to give a 3 wt. % ceramic yield solution. The precursor solution was aerosolized with oxygen into a quartz chamber where it was combusted with methane/oxygen pilot torches in an oxygen rich environment. Resulting nanopowders were collected down-stream in rod-in-tube electrostatic precipitators (ESP) operated at 10 kV. The LF-FSP process is detailed in our previous work.[36,39,40]

6.2.2. Powder and film processing

As-produced powders were first dispersed in EtOH (200 proof, Decon Labs) with 2 wt. % polyacrylic acid (M_n=2000, Sigma-Aldrich) dispersant, using an ultrasonic horn (Vibra cell VC-505, Sonics and Materials, Inc.) at 100 W for 15 min. The suspension was let settle for 4 h to allow larger particles to settle. Supernatant was decanted and dried. Collected powder, polyvinyl butyral, benzyl butyl phthalate, acetone, and ethanol at selected wt. ratio (Table **6.2**) were added to a 20 ml vial and ball-milled with 3.0 mm diameter spherical ZrO_2 beads for 12-24 h to homogenize the suspension. Sum of wt. % is not 100 due to rounding off. Suspensions were cast using a wire wound rod coater (Automatic Film Applicator-1137, Sheen Instrument, Ltd). Film thicknesses

were controlled by adjusting the gap between the rod and the substrate. Dried green films were manually peeled off the Mylar substrate, and cut to selected sizes. Green films were uniaxially pressed in between stainless steel dies at 80-100 °C with a pressure of 50-70 Mpa for 5-10 minutes using a bench top press equipped with a heater (Carver, Inc) to improve packing density.

Table 6.2. Starting materials and composition for suspension formulation.

	Role	Wt.%
LLZO with 2 wt.% polyacrylic acid	Powder/dispersant	37
Benzyl butyl phthalate	Plasticizer	3
Polyvinyl butyral	Binder	3
Ethanol	Solvent	29
Acetone	Solvent	29

6.2.3. Film sintering

Green films were placed between graphite foils and heated to selected temperatures and dwell times in N_2 (100 ml min^{-1}). Graphite foil was used to avoid possible contamination or reaction with common ceramic crucibles. The resulting films had carbon deposits that were removed by reheating to 700-800 °C for 1-4 h in O_2. Films were placed on MgO plates during carbon removal.

6.2.4. Thermal etching

Sintered films were manually fractured and heated to 910 °C for 0.2 h in N_2, placed in between graphite foils. Since the fracture yields a fairly two dimensional fracture surface, no grinding/polishing was necessary. Average grain sizes were calculated by the lineal intercept method.

6.2.5. Characterization

X-ray diffraction measurements were carried out using a Rigaku Rotating Anode Goniometer (Rigaku Denki., LTD., Tokyo, Japan). Scans were made from 10 to 70° 2θ, using a scan rate of 5°

min^{-1} in 0.01° increments and Cu Kα radiation (1.541 Å) operating at 40 kV and 100 mA. Scan rate of 1° min^{-1} in 0.01° increments was used for as-produced powder mixed with α-Al_2O_3 internal standard. The Jade program 2010 (Version 1.1.5 from Materials Data, Inc.) was used to determine the presence of crystallographic phases, wt. fraction, and to refine lattice constants. Following reference files were used; c-LLZO (PDF# 04-018-3158), t-LLZO (PDF# 01-080-6140), $La_2Zr_2O_7$ (PDF# 01-070-5602), La_2O_3 (PDF# 04-008-8233), Li_2CO_3 (PDF# 98-000-0473), α-Al_2O_3 (PDF# 98-000-0174).

Specific surface areas (SSA) were obtained using a Micromeritics ASAP 2020 sorption analyzer. Samples (400 mg) were degassed at 300 °C/5 h. Each analysis was run at −196 °C (77 K) with N_2. The SSAs were determined by the BET multipoint method using ten data points at relative pressures of 0.05−0.30. SSA was converted to average particle sizes (APS) using the equation APS = 6/(SSA×ρ). The net density (ρ) of the as-produced powder was approximated by rule of mixture. Density of stoichiometric $La_2Zr_2O_7$ was used as an estimate.

Micrographs were taken using a FEI NOVA Nanolab system (FEI company). Powder samples were used as is, sintered films were fractured for imaging. All samples were sputter coated with gold using a SPI sputter coater (SPI Supplies, Inc.).

Q600 simultaneous TGA/DSC (TA Instruments, Inc.) was used to observe thermal decomposition of as-produced powders and green films. Samples (15–25 mg) were loaded in alumina pans and ramped to 1000 °C at 10 °C min^{-1} under constant air flow at 60 ml min^{-1}.

FTIR (Fourier transform Infrared spectroscopy) spectrum were taken using a Nicolet 6700 Series FTIR spectrometer (Thermo Fisher Scientific, Inc.). Optical grade, random cuttings of KBr (International Crystal Laboratories) were ground, with 1 wt. % of the sample to be analyzed. The

sample chamber was purged with N_2 prior to data acquisition in the range 4000–400 cm^{-1} with a precision of ±4 cm^{-1}.

AC impedance data were collected with broadband spectrometer (Novocontrol technologies) in a frequency range of 10 MHz to 0.1 Hz at -35 to 85 °C in increments of 10 °C. Concentric gold electrodes, 3 mm in diameter, were deposited using a SPI sputter coater on both surfaces of the films using a deposition mask. "EIS spectrum analyser" software was used for extracting total resistance. Equivalent circuit consisting of $(R_{total}Q_{total})(Q_{electrode})$ was used. R and Q denote resistance and constant phase element, respectively. SEM fracture surface images were taken to measure sample thicknesses.

Final sintered film densities were determined by Archimedes method using ethanol as media.

6.3. Results and Discussion

Below, we first discuss the characterization of liquid-feed flame spray pyrolysis (LF-FSP) produced LLZO powders and then the efforts to transform the powders into dense LLZO films.

Nanopowders of $Li_{6.25}Al_{0.25}La_3Zr_2O_{12}$ composition with 50 wt. % excess Li were produced using LF-FSP. Al^{3+} doping stabilizes the high ionic conductivity cubic phase,[32] and excess Li is used to balance losses incurred during sintering. Literature indicates that sintering 1-2 mm thick pellets requires 10-15 wt. % excess Li,[26,29] 50 wt. % was chosen for our studies.

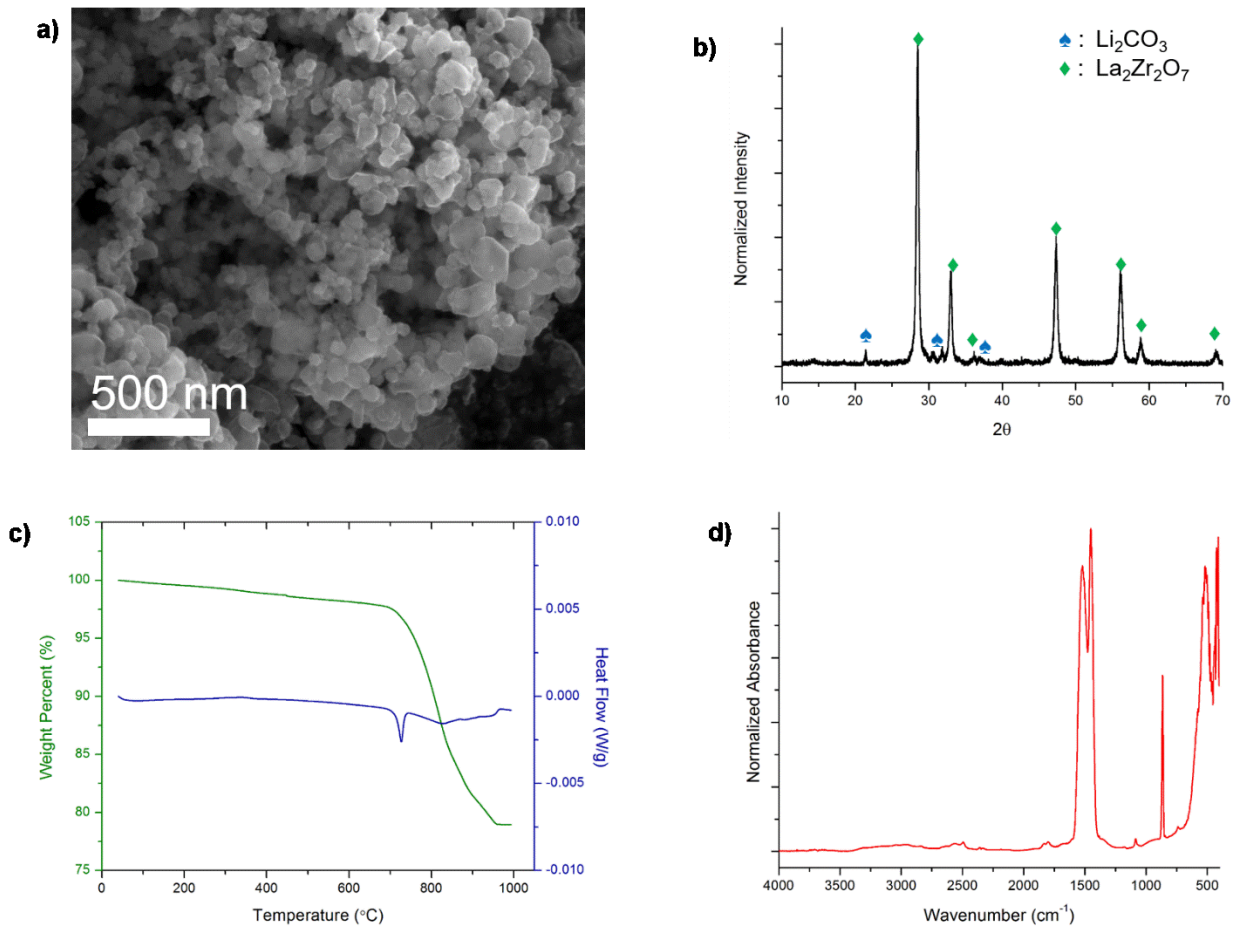

Figure 6.2. (a) SEM (b) XRD (c) TGA (d) FTIR of the as-produced nanopowders.

The resulting spherical nanoparticles offer a narrow size distribution (Figure **6.2a**). The BET N_2 adsorption derived specific surface area was 16 m^2 g^{-1} with corresponding average particle sizes of ≈ 90 nm.

While LF-FSP normally generates pure oxides, a mixture of Li_2CO_3 and off-stoichiometric $La_2Zr_2O_7$ was detected by XRD (Figure **6.2b**). The combustion byproducts H_2O and CO_2 and high flame temperatures (>1500 °C), either accelerate decomposition or prevent LLZO from forming.[41] For off-stoichiometric $La_2Zr_2O_7$, LF-FSP provides access to phases or compositions stable at high temperatures due to rapid quenching.[39] XRD peak shifts were confirmed and new lattice constants were refined using α-Al_2O_3 as an internal standard corroborating off-stoichiometry (Figure **6.3**).

Observed off-stoichiometric $La_2Zr_2O_7$ peaks are shifted left with respect to stoichiometric $La_2Zr_2O_7$ (red drop lines), indicating larger lattice constants. New lattice constant of 10.87882 Å was refined using the whole pattern fitting of Jade software. This is larger than the stoichiometric lattice constant, 10.7997 Å. Hence, the off-stoichiometric composition is $0.43La_2O_3$-$0.57ZrO_2$ ($La_3Zr_2O_{8.5}$) which is stable at temperatures of >1550 °C based on the ZrO_2-La_2O_3 binary phase diagram.[42] Rapid quenching of LF-FSP gives access to high temperature phases.

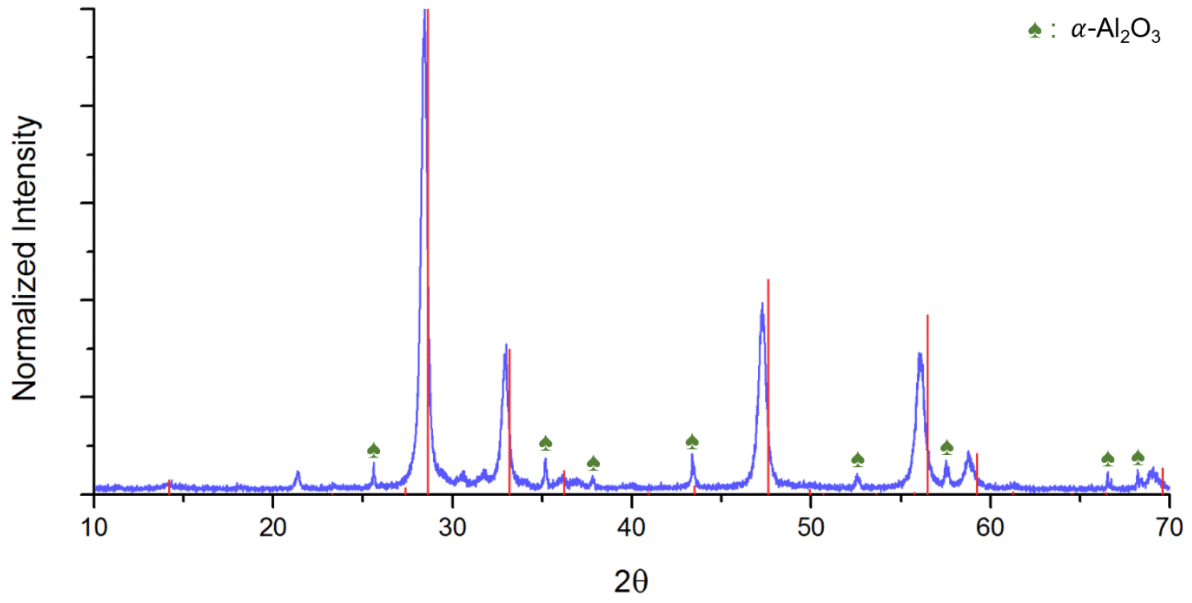

Figure 6.3. XRD scan of as-produced LLZO with α-Al_2O_3 internal standard. An internal standard, α-Al_2O_3, was mixed with as-produced LLZO using a mortar and pestle. Peak shifts are noted.

TGA and FTIR further confirm the product is fully decomposed LLZO. TGA shows an endothermic mass loss starting at ~700 °C, ascribed to Li_2CO_3 melting with a loss of CO_2 ending at ~950 °C (Figure **6.2c**). Mass loss matches theory for heating fully decomposed LLZO incorporating excess lithium. FTIR shows νC=O for carbonates (865, 1400-1600 cm^{-1}) as well as νM-O (< 600 cm^{-1}) (Figure **6.2d**).

Previous attempts to produce nano-LLZO also resulted in decomposed products likely due to its instability under the synthesis condition.[26,43] Powders showed non-uniform sizes and shapes which were aggregated, or lost nano-scale on calcination. These morphological features are all detrimental to sintering, hindering uniform packing of the green body, likely limiting access to target ceramic shapes with optimal properties.

In contrast, in this study spherical nanoparticles with narrow size distributions can be processed directly to green films using chemical reaction and uniform packing to drive densification at lower temperatures. For convenience, the initial nanopowder is labeled LLZO although it is a decomposed mixture.

Green films were produced by conventional ball-milling and casting. LLZO nanopowders were ball-milled with dispersant, binder, plasticizer, and solvents per Table **6.2**. After 12-24 h of ball-milling, the homogenized suspension was bar cast on Mylar sheets. Compared to common pellet compaction studies wherein nanoparticle agglomerates result in pores after sintering, wet processing breaks down agglomerates during ball-milling and gives uniform particle packing within the polymeric matrix, beneficial to sintering.[44] It is important to formulate a stable system such that particles do not flocculate during drying.

TGAs of green films were run to confirm the solids loading prior to sintering (Figure **6.4**). Initial 2 wt. % mass loss at < 200 °C is ascribed to removal of residual solvent and/or physi-/chemi-sorbed water. Following mass losses with exotherms are due to oxidative decomposition of polymeric additives; dispersant, binder, and plasticizer. Most polymeric additives are oxidatively removed at ~450 °C and the mass remains stable to ~680 °C. An endotherm attributed to melting of Li_2CO_3 is observed near 720 °C accompanied by mass loss as CO_2 evolves, in accordance with the TGA-DSC of the as-produced powder (Figure **6.2c**). Final ceramic yield is ~66 wt. %, in good

agreement with theoretically expected based on Table **6.2**. Note the ceramic yield of LLZO with 2 wt. % PAA dispersant itself is ~77 wt.%.

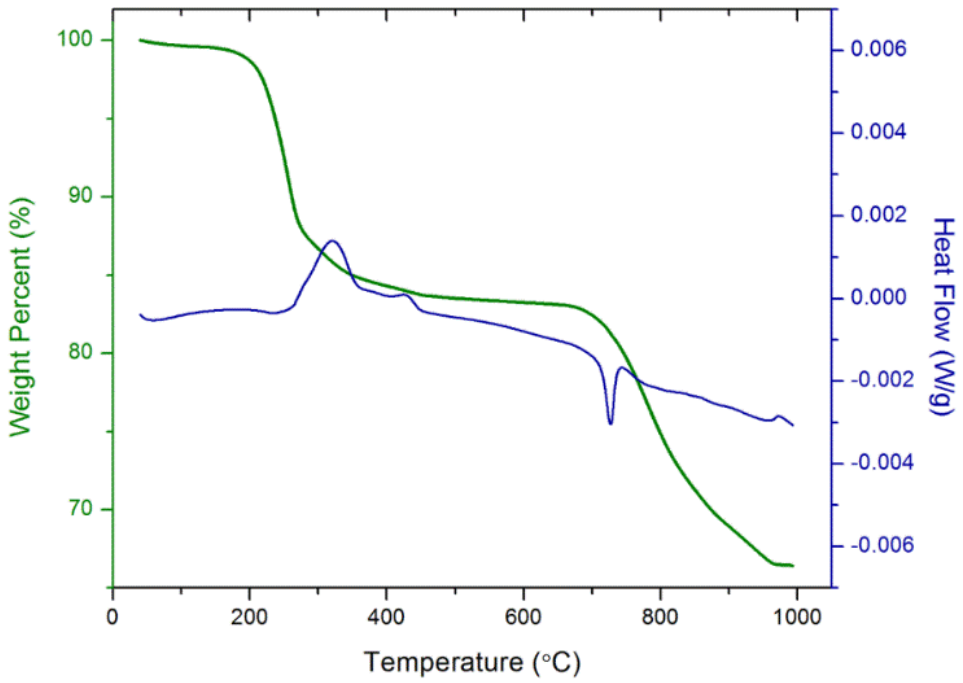

Figure 6.4. TGA-DSC of LLZO green film.

Given there is a limited reservoir of Li in the starting LLZO nanopowder (50 wt. % excess), densification must be complete before it volatilizes completely, preferably resulting in single-phase c-LLZO. Hence, a short dwell time of 1 h was selected, targeting optimal densification. Indeed, extended dwell below the sintering temperature generated c-LLZO but with low relative densities. Green film thicknesses were fixed at 45±2 µm for this set of experiments since it is also a variable (see below). Tetragonal-LLZO (t-LLZO) was first observed at 800 °C as expected due to excess Li (Figure **6.5**), known to drive formation of t-LLZO even with Al^{3+} doping.[32] Further increases in temperature drive Li loss and transform t-LLZO to c-LLZO.

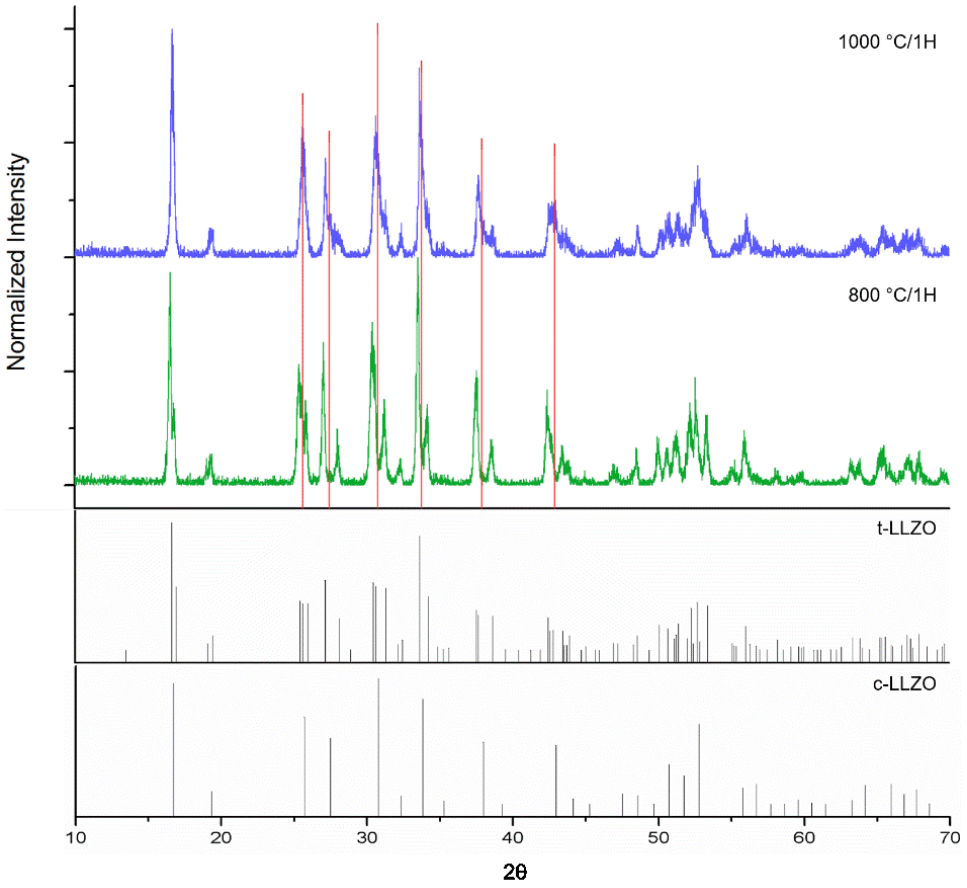

Figure 6.5. XRD scans of LLZO films heated to 800 and 1000 °C for 1 h. Film heated to 800 °C/1 h shows mostly t-LLZO whereas on heating to 1000 °C/1 h a mixture of c-LLZO and t-LLZO forms, indicating Li_2O is volatilized at or near 1000 °C. Selected major c-LLZO peaks are marked as red drop lines to mark the difference.

Single-phase c-LLZO was observed at 1080 °C/1 h (Figure **6.7**) with some closed porosity per the SEM fracture surface image (Figure **6.6a,b**). On heating to 1090 °C/1 h, traces of $La_2Zr_2O_7$ form (Figure **6.7**). Trans-granular fracture surfaces reveal very high relative densities (Figure **6.6c,d**) and suggest good-to-excellent grain boundary contact. Trans-granular fracture dominates mechanical behavior with increasing relative densities.[35] 1100 °C/1 h sintered samples exhibit noticeable secondary phase peaks corresponding to $La_2Zr_2O_7$ and La_2O_3 (Figure **6.7**). The overall microstructures look similar other than distinct microstructural features appearing near the surface, likely initiation of secondary phase formation as Li volatilizes (Figure **6.6e,f**, Figure **6.8**). Single

phase c-LLZO thin films (< 30 μm) with high relative densities (94±1 %) form on sintering at 1090 °C/1 h. These films are the very first examples that meet the challenges cited above.

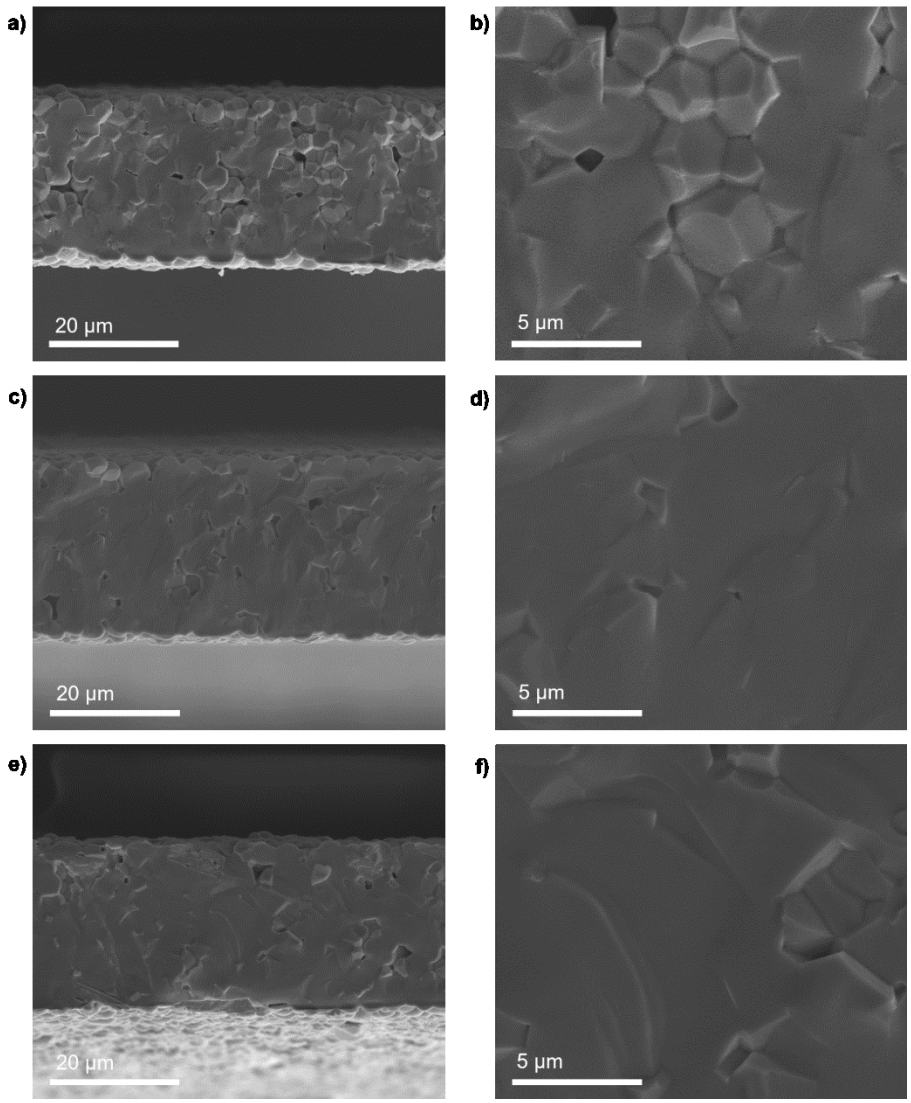

Figure 6.6. SEM fracture surface images of films sintered at (a),(b) 1080 °C/1 h (c),(d) 1090 °C/1 h and (e),(f) 1100 °C/1 h.

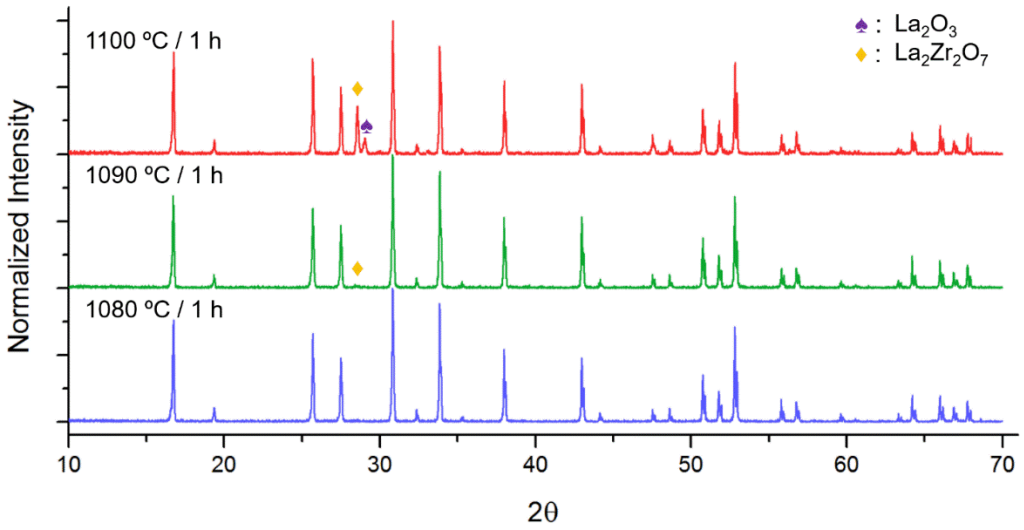

Figure 6.7. XRD of films sintered at (a),(b) 1080 °C/1 h (c),(d) 1090 °C/1 h and (e),(f) 1100 °C/1 h.

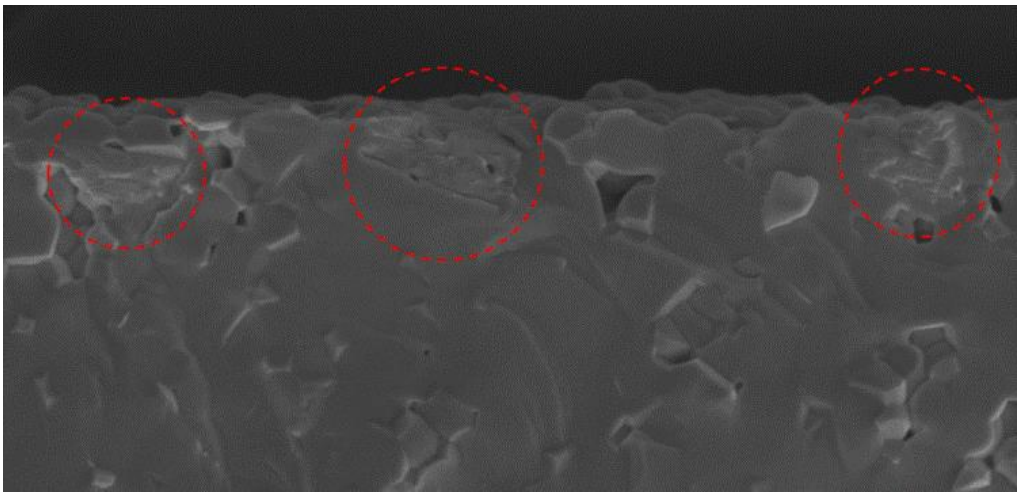

Figure 6.8. SEM fracture surface image of c-LLZO film sintered at 1100 °C for 1 h. Circled area show distinctly different microstructural features. It is likely these are the initiation point of secondary phases $La_2Zr_2O_7$ and La_2O_3 as Li_2O is lost at the surface on over-exposure of heat.

Sintering times are greatly reduced from 10-40 h to 1 h, and at lower temperatures compared to common solid-state reaction methods.[13,20] This result likely arises from combined effects of uniform particle packing, nanoparticles' high surface energies, and chemical reactions of the constituent materials including liquid phase sintering promoted by Li_2CO_3. Off-stoichiometric

$La_2Zr_2O_7$ does not seem to be a determining factor since similar starting powders form in sol-gel syntheses and do not dramatically enhance sintering behavior.[43]

Based on Figure **6.6** and **6.7** we conclude that c-LLZO thin films' microstructures and phase compositions are very sensitive to sintering temperature; correlated to Li loss rates. Hence another set of experiments was run with the sintering temperature fixed at 1090 °C/1 h but with different green film thicknesses. Given Li is lost at the surface, the surface/volume ratio becomes an important parameter. Surface/volume ratio dictates lithium loss rate and drastically changes at film thicknesses below 50 µm, indicating final sintered product properties are sensitive to green film thicknesses (Figure **6.9a**). For simplicity sake, it is assumed there is no porosity. Note that 40 µm thick film's surface/volume ratio is ~20x greater than for 1 mm thick pellet. As such, different sintering conditions are required for samples with different thicknesses. Changes in surface/volume ratio exist with varying lateral dimensions for thick samples but converge to the same values as thickness is reduced.

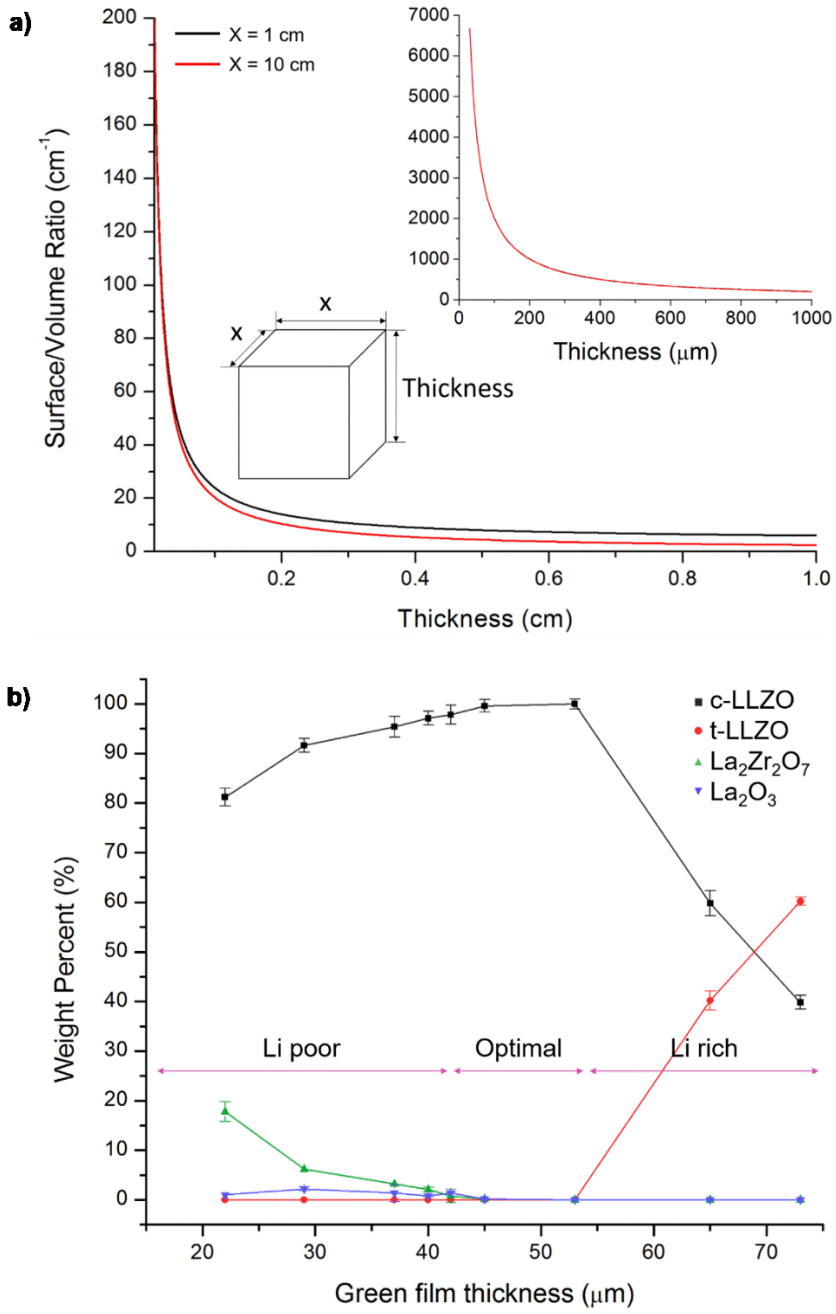

Figure 6.9. (a) Surface/volume ratio plot. (b) Phase composition changes with film thicknesses although all of them were heated to the same condition of 1090 °C / 1 h.

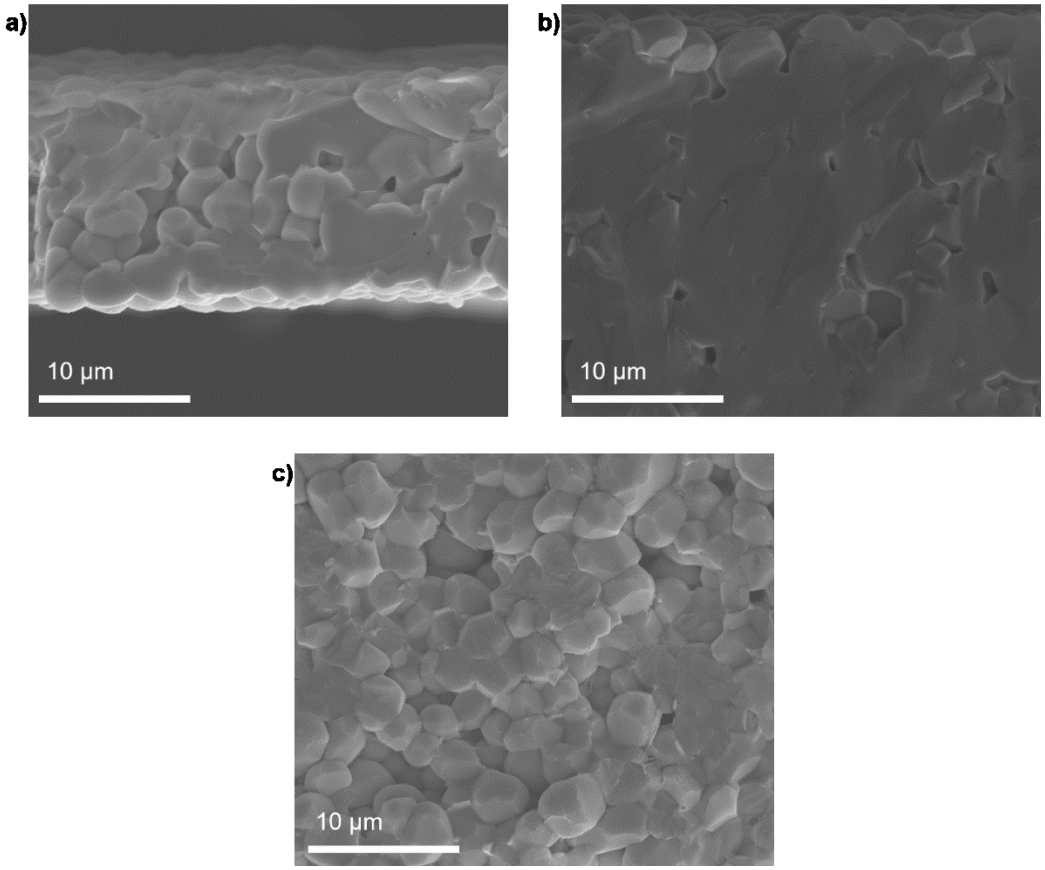

Figure 6.10. SEM fracture surface images of sintered (a) 22 µm (b) 45 µm and (c) 73 µm thick green film.

As hypothesized, thicker green films showed t-LLZO and thinner green films $La_2Zr_2O_7$ and La_2O_3 secondary phases when sintered (Figure **6.9b**) using the same schedule. Li poor, optimal, and Li rich ranges in terms of green film thicknesses were determined based on the phase composition and microstructure (Figure **6.9**, **6.10** and **6.11**). Li poor films show low relative densities as secondary phases $La_2Zr_2O_7$ (6.04 g cm^{-3}) and La_2O_3 (5.98 g cm^{-3}) have higher densities compared to c-LLZO (5.10 g cm^{-3}) and $La_2Zr_2O_7$ has high sintering resistance.[45] Thicker films also gave low relative densities suggesting that t-LLZO does not sinter at this temperature whereas c-LLZO does.

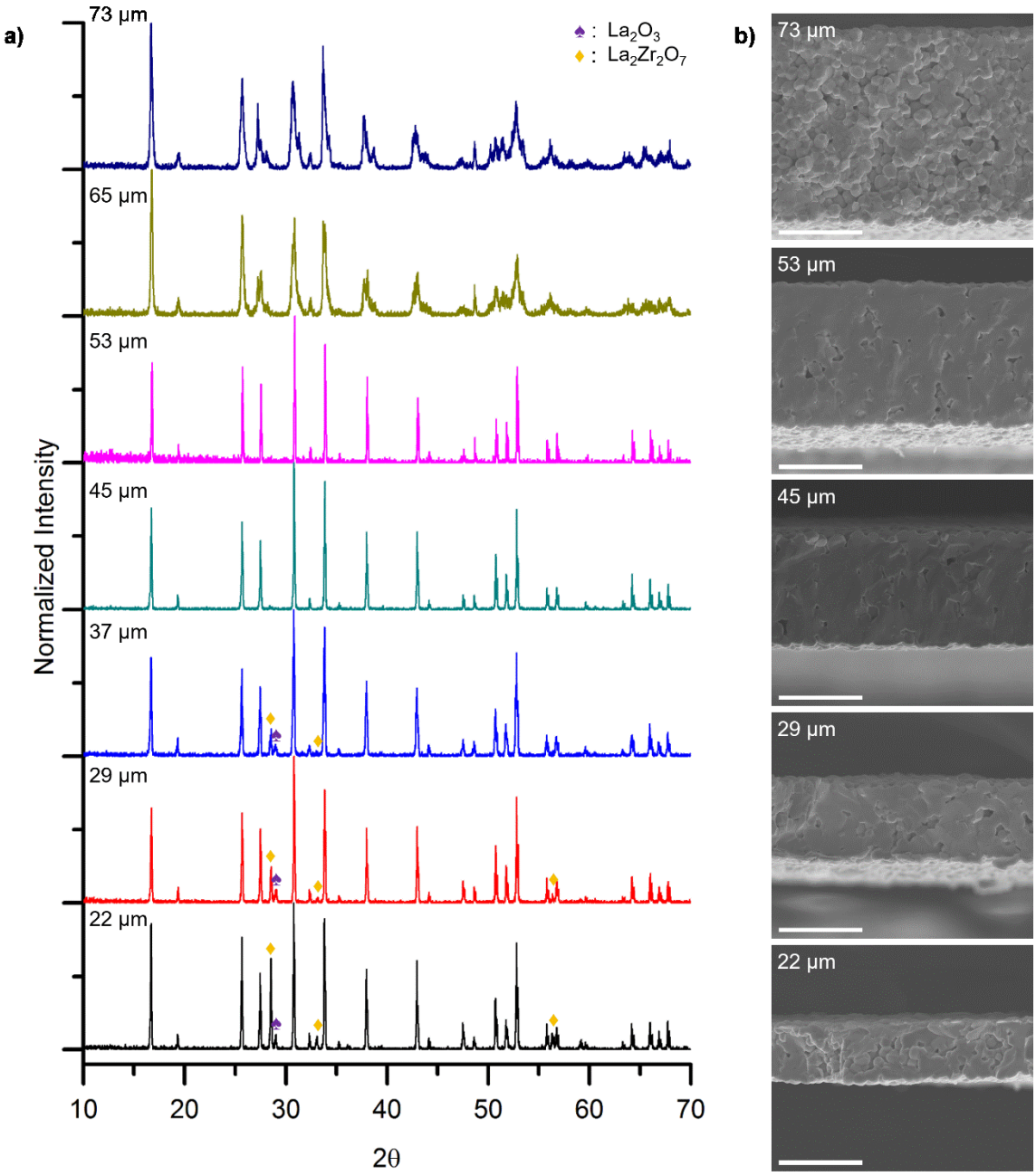

Figure 6.11. (a) XRD scans and (b) SEM micrographs of LLZO films with different green film thicknesses heated to 1090 °C for 1 h. Note the thicknesses labelled are green film thicknesses, not sintered film thicknesses. La_2O_3 and $La_2Zr_2O_7$ peak intensities rise with decreasing thickness. Films too thick result in t-LLZO as observed by peak splitting for 65 and 73 µm thick film. Microstructures of sintered films are affected by lithium content as secondary phases, including t-LLZO, have different sintering temperatures compared to c-LLZO. Scale bar, 20 µm for (b).

The sintered films' (in optimal range) electrochemical properties were measured. Nyquist plots show semi-circles at high frequencies followed by a spike at low frequencies, typical of ion conductors with blocking electrodes (Figure **6.12**). Room temperature conductivities of 0.2±0.03 mS cm^{-1} and activation energies of 0.35±0.01 eV (33.8±0.7 kJ mol^{-1}) were obtained (Figure **6.12**), in good agreement with high density pellet counterparts.[20,28,32] No noticeable grain boundary resistance was observed due to high relative density and superior grain boundary contact. In comparison, c-LLZO films with low relative densities showed grain boundary resistance and lower ionic conductivities (Figure **6.13**).

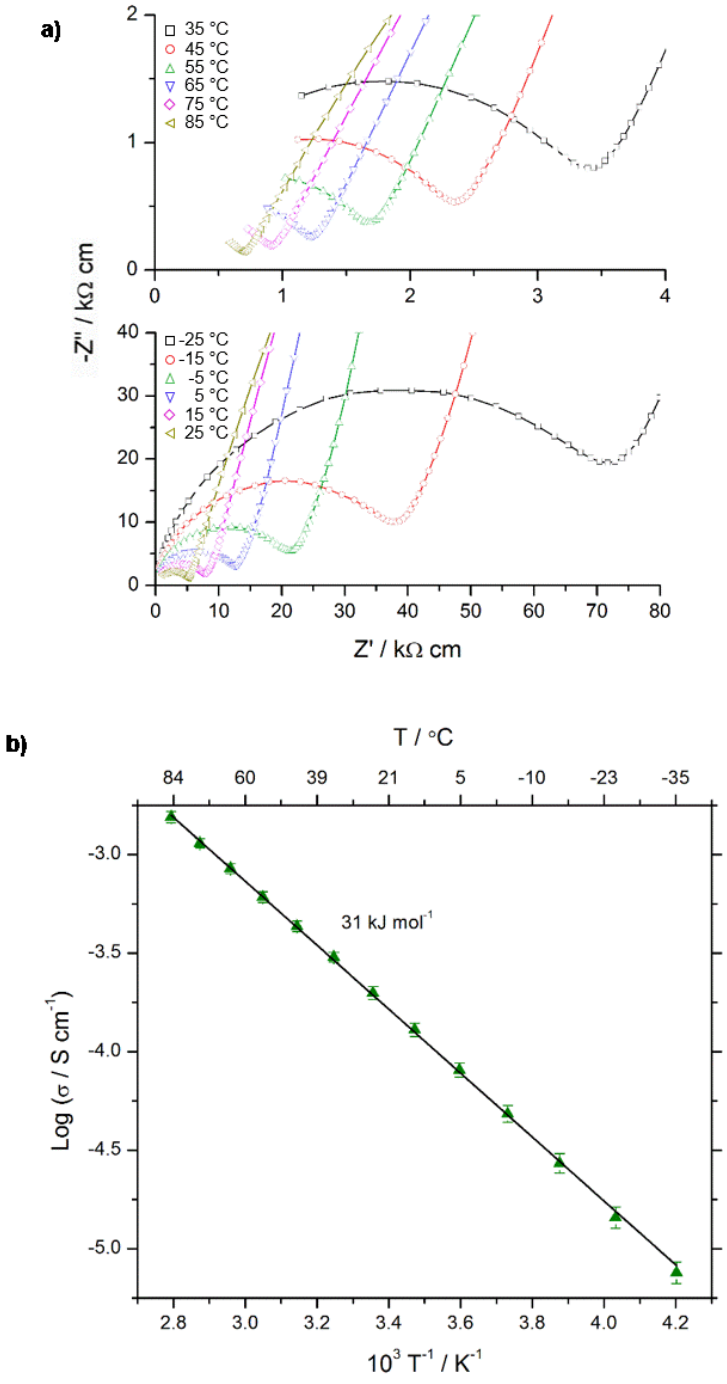

Figure 6.12. Electrochemical properties of sintered LLZO films. (a) Nyquist plots of sintered films. Thickness and electrode area are taken into account. Note the units are kΩ cm. (b) Ionic conductivities of c-LLZO rises with temperature showing Arrhenius trend.

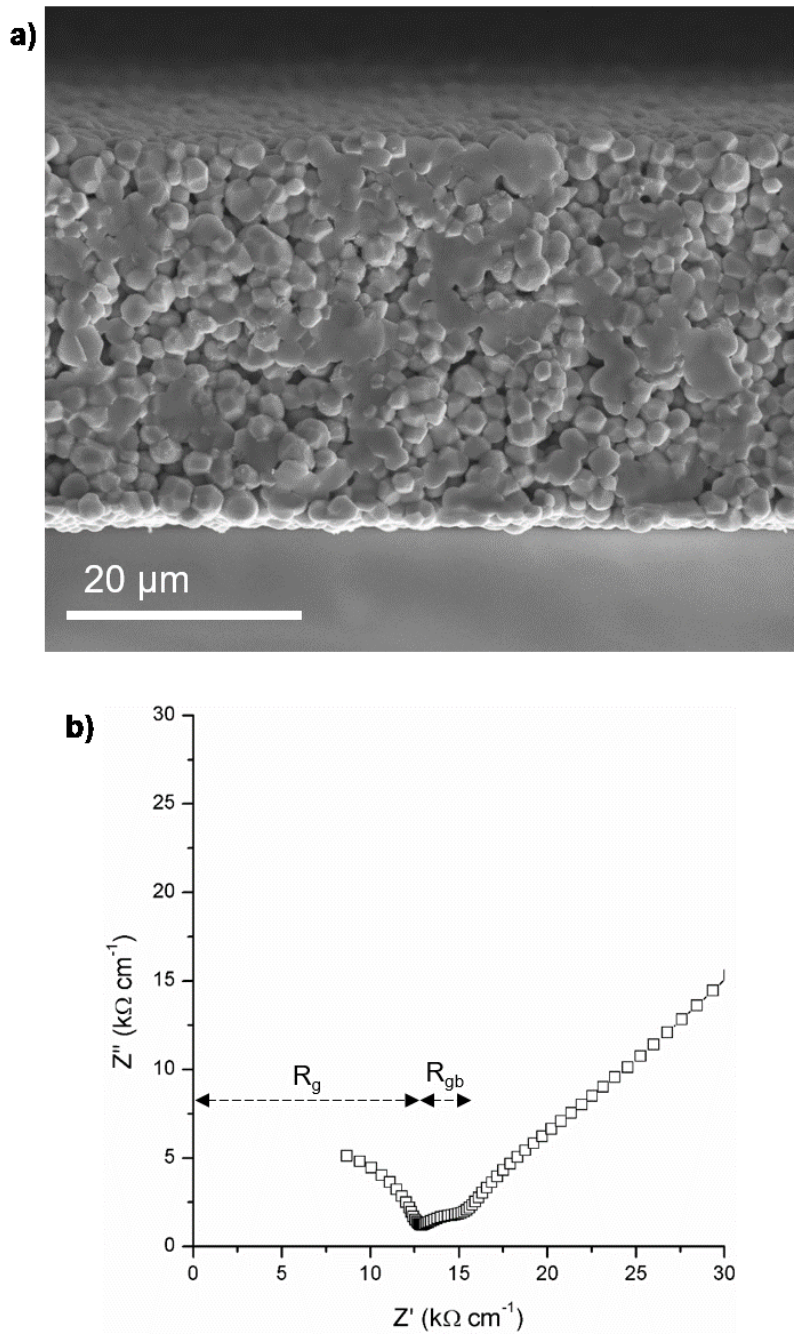

Figure 6.13. (a) SEM fracture surface image and (b) Nyquist plot of c-LLZO films heated to below sintering temperature. Films sintered at 1070 °C for 2 h did not fully densify, showing porosity. Mixed inter- and trans-granular fracture modes are observed. XRD confirmed single phase c-LLZO. Nyquist plot shows both grain and grain boundary resistance component. Total ionic conductivity is calculated as 0.07±0.01 mS cm^{-1}.

Ionic conductivities of 0.008±0.001 to 1.5±0.1 mS cm^{-1} were measured at -35 to 85 °C (Figure **6.12**) demonstrating a wide operating temperature window, including temperatures inaccessible using common liquid electrolytes due to decomposition,[8] flammability,[8] or freezing.[46] We anticipate that still higher operating temperatures leading to faster charge/discharge rates will be accessible in Li batteries using ceramic electrolytes.

Sintered < 30 μm thick films with 2×2 cm^2 lateral dimensions were produced that are translucent at high relative densities, and flexible (Figure **6.14a**). With decreasing thicknesses, the strain accompanying bending reduces such that even ceramics become flexible below certain thicknesses.[47] Average grain sizes (AGSs) are 2.4±0.4 μm, which translates to films 10–15 grains thick (Figure **6.14b,c**). AGSs are 40-80 times smaller compared to solid state reaction[34] derived c-LLZO but similar to hot pressed.[32,35]

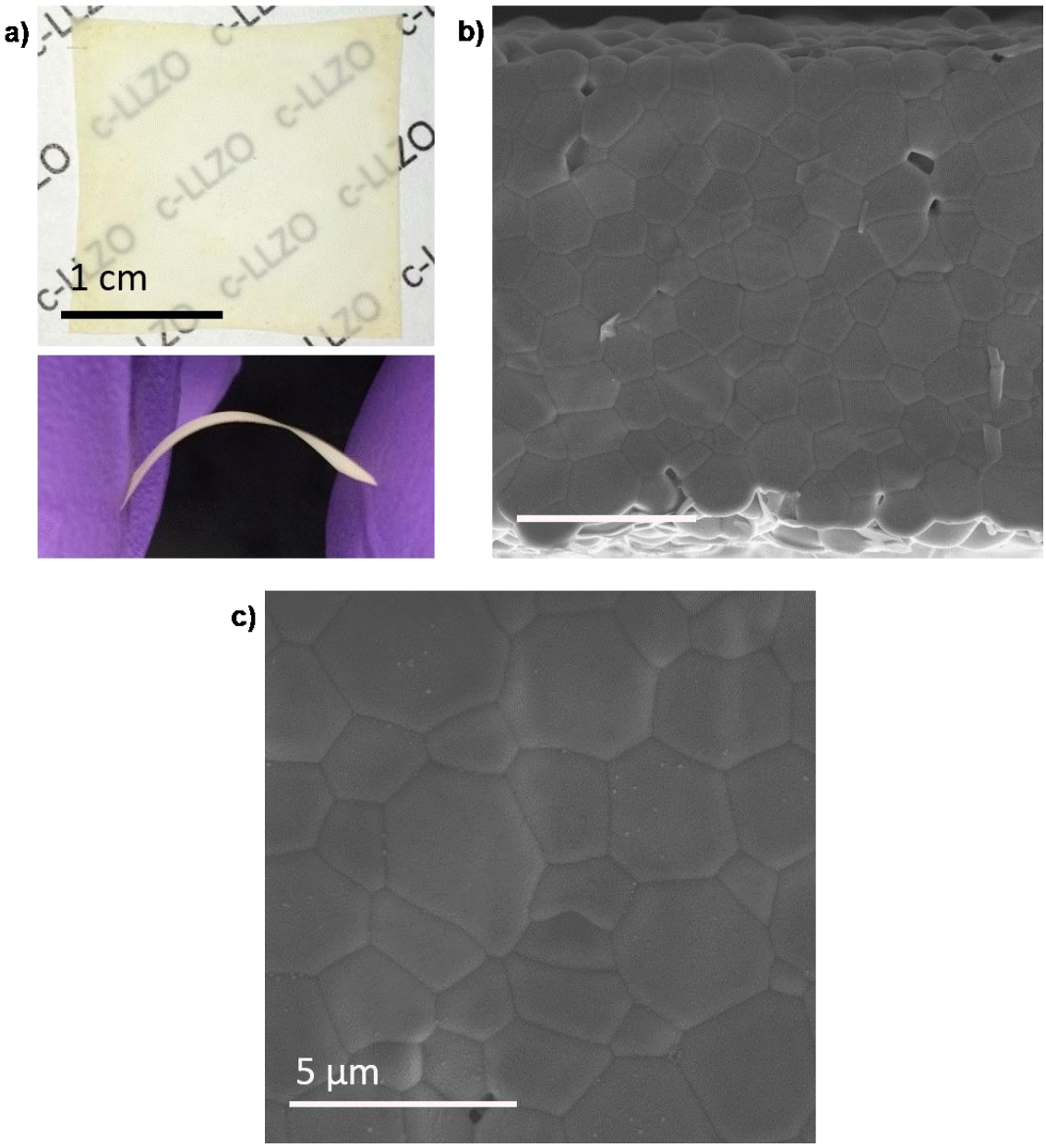

Figure 6.14. Translucent, flexible sintered c-LLZO films. (a) Photograph of c-LLZO film sintered within the optimal range. "c-LLZO" printed on the background is visible due to low thicknesses (<30 µm). Films show decent flexibility, property inherent to thin ceramics. The sintered film is roughly 2 × 2 cm^2. (b),(c) Thermally etched fracture surfaces of sintered films.

A further comment is necessary. Additional benefits from these Li^+ conducting thin films is that they offer mechanical properties that allow them to flex such that roll-to-roll processing and easier handling are permitted.[18] Flexibility in ceramics extends from two attributes: (1) the need to have

dense, fine grained materials in the final film to ensure that any cracks must propagate via a tortuous path that absorbs the energy driving propagation and (2) the absence of surface flaws that initiate cracking.[48] A more rigorous definition based on Griffith micro-crack theory states that insufficient mechanical force can be imparted to the film or fiber to initiate crack formation. Such constraints mandate the use of nanopowders to access fine grained, flexible, thin and yet dense < 30 μm films as demonstrated in this work.

6.4. Conclusions

In conclusion, we have overcome processing difficulties involved in c-LLZO by reactive sintering carbonate and oxide nanoparticle mixtures and wet processing to minimize agglomerate formation. The first examples of c-LLZO thin films (20-30 μm thick, similar to commercial polymer separators[6]) with properties similar to bulk materials are demonstrated. Surface/volume ratios were determined to be a critical factor in sintering due to Li_2O volatility. Cell assembly and testing can now be done at prototype levels, and the film thicknesses achieved here potentially enable higher energy storage densities in assembled cells. Subsequent goals will be to reduce final thicknesses, sintering temperatures, and to reduce excess Li contents. Reduced sintering temperatures will retard Li_2O loss rates, widening the optimal processing window.

Films processed here show good flexibility, suggesting casting-sintering of nanoparticles may be an alternate route to process batteries requiring mild flexibility. Reduction in film thicknesses would be necessary to further improve flexibility, to incorporate active material layers, as well as to improve attainable energy densities. On the other hand, it is easy to envision the use of the films produced here in aqueous Li cells or solid state Li-air cells to replace the commonly used thick,

commercial Li metal phosphate membranes (50-200 μm) which has narrower pH stability window (7-10 vs. 7-11.5).[9,17]

References

1. M. Armand and J.-M. Tarascon, *Nature*, 2008, **451**, 652-657.

2. B. Dunn, H. Kamath and J.-M. Tarascon, *Science*, 2011, **334**, 928-935.

3. P. G. Bruce, S. A. Freunberger, L. J. Hardwick and J.-M. Tarascon, *Nat. Mater.*, 2012, **11**, 19-29.

4. Y. Shao, F. Ding, J. Xiao, J. Zhang, W. Xu, S. Park, J.-G. Zhang, Y. Wang and J. Liu, *Adv. Funct. Mater.*, 2013, **23**, 987-1004.

5. W. Xu, J. Wang, F. Ding, X. Chen, E. Nasybulin, Y. Zhang and J.-G. Zhang, *Energy Environ. Sci.*, 2014, **7**, 513-537.

6. H. Lee, M. Yanilmaz, O. Toprakci, K. Fu and X. Zhang, *Energy Environ. Sci.*, 2014, **7**, 3857-3886.

7. B. Scrosati and J. Garche, *J. Power Sources*, 2010, **195**, 2419-2430.

8. P. G. Balakrishnan, R. Ramesh and T. Prem Kumar, *J. Power Sources*, 2006, **155**, 401-414.

9. F. Li, H. Kitaura and H. Zhou, *Energy Environ. Sci.*, 2013, **6**, 2302-2311.

10. P. Knauth, *Solid State Ionics*, 2009, **180**, 911-916.

11. N. Kamaya, K. Homma, Y. Yamakawa, M. Hirayama, R. Kanno, M. Yonemura, T. Kamiyama, Y. Kato, S. Hama, K. Kawamoto and A. Mitsui, *Nat. Mater.*, 2011, **10**, 682-686.

12. L. J. Miara, S. P. Ong, Y. Mo, W. D. Richards, Y. Park, J.-M. Lee, H. S. Lee and G. Ceder, *Chem. Mater.*, 2013, **25**, 3048-3055.

13. V. Thangadurai, S. Narayanan and D. Pinzaru, *Chem. Soc. Rev.*, 2014, **43**, 4714-4727.

14. Y. Ren, K. Chen, R. Chen, T. Liu, Y. Zhang, C.-W. Nan and B. Vyas, *J. Am. Ceram. Soc.*, 2015, **98**, 3603-3623.

15. J. C. Bachman, S. Muy, A. Grimaud, H. H. Chang, N. Pour, S. F. Lux, O. Paschos, F. Maglia, S. Lupart, P. Lamp, L. Giordano and Y. Shao-Horn, *Chem. Rev.*, 2016, **116**, 140-162.

16. T. Thompson, A. Sharafi, M. D. Johannes, A. Huq, J. L. Allen, J. Wolfenstine and J. Sakamoto, *Adv. Energy Mater.*, 2015, **5**, 1500096.

17. C. Ma, E. Rangasamy, C. Liang, J. Sakamoto, K. L. More and M. Chi, *Angew. Chem. Int. Ed.*, 2015, **54**, 129-133.

18. Advanced Research Projects Agency - Energy (ARPA-E), U.S. Department of Energy. DE-FOA-0001478. Integration and optimization of novel ion conducting solids (IONICS). 2016, (https://arpa-e-foa.energy.gov/).

19. B. D. McCloskey, *J. Phys. Chem. Lett.*, 2015, **6**, 4581-4588.

20. R. Murugan, V. Thangadurai and W. Weppner, *Angew. Chem. Int. Ed.*, 2007, **46**, 7778-7781.

21. M. Kotobuki, H. Munakata, K. Kanamura, Y. Sato and T. Yoshida, *J. Electrochem. Soc.*, 2010, **157**, A1076-A1079.

22. S. Ohta, T. Kobayashi and T. Asaoka, *J. Power Sources*, 2011, **196**, 3342-3345.

23. K. Liu and C.-A. Wang, *Electrochem. Commun.*, 2014, **48**, 147-150.

24. Y. Li, Z. Wang, C. Li, Y. Cao and X. Guo, *J. Power Sources*, 2014, **248**, 642-646.

25. L. Cheng, W. Chen, M. Kunz, K. Persson, N. Tamura, G. Chen and M. Doeff, *ACS Appl. Mater. Interfaces*, 2015, **7**, 2073-2081.

26. R. Djenadic, M. Botros, C. Benel, O. Clemens, S. Indris, A. Choudhary, T. Bergfeldt and H. Hahn, *Solid State Ionics*, 2014, **263**, 49-56.

27. K. Tadanaga, H. Egawa, A. Hayashi, M. Tatsumisago, J. Mosa, M. Aparicio and A. Duran, *J. Power Sources*, 2015, **273**, 844-847.

28. N. Janani, C. Deviannapoorani, L. Dhivya and R. Murugan, *RSC Adv.*, 2014, **4**, 51228-51238.

29. H. Imagawa, S. Ohta, Y. Kihira and T. Asaoka, *Solid State Ionics*, 2014, **262**, 609-612.

30. Y. Jin and P. J. McGinn, *J. Power Sources*, 2011, **196**, 8683-8687.

31. J. Sakamoto, E. Rangasamy, H. Kim, Y. Kim and J. Wolfenstine, *Nanotechnology*, 2013, **24**, 424005.

32. E. Rangasamy, J. Wolfenstine and J. Sakamoto, *Solid State Ionics*, 2012, **206**, 28-32.

33. J.-M. Tarascon and M. Armand, *Nature*, 2001, **414**, 359-367.

34. L. Cheng, J. S. Park, H. Hou, V. Zorba, G. Chen, T. Richardson, J. Cabana, R. Russo and M. Doeff, *J. Mater. Chem. A*, 2014, **2**, 172-181.

35. Y. Kim, H. Jo, J. L. Allen, H. Choe, J. Wolfenstine, J. Sakamoto and G. Pharr, *J. Am. Ceram. Soc.*, 2016, **99**, 1367-1374.

36. E. Yi, W. Wang, S. Mohanty, J. Kieffer, R. Tamaki and R. M. Laine, *J. Power Sources*, 2014, **269**, 577-588.

37. J. Tan and A. Tiwari, *ECS Solid State Let.*, 2012, **1**, Q57-Q60.

38. D. J. Kalita, S. H. Lee, K. S. Lee, D. H. Ko and Y. S. Yoon, *Solid State Ionics*, 2012, **229**, 14-19.

39. T. R. Hinklin, J. Azurdia, M. Kim, J. C. Marchal, S. Kumar and R. M. Laine, *Adv. Mater.*, 2008, **20**, 1373-1375.

40. C. R. Bickmore, K. F. Waldner, R. Baranwal, T. Hinklin, D. R. Treadwell and R. M. Laine, *J. Eur. Ceram. Soc.*, 1998, **18**, 287-297.

41. C. Galven, J. Dittmer, E. Suard, F. Le Berre and M.-P. Crosnier-Lopez, *Chem. Mater.*, 2012, **24**, 3335-3345.

42. R. S. Roth, *J. Res. Natl. Bur. Stand.*, 1956, **56**, 17-25.

43. I. Kokal, M. Somer, P. H. L. Notten and H. T. Hintzen, *Solid State Ionics*, 2011, **185**, 42-46.

44. D. Hotza and P. Greil, *Mater. Sci. Eng., A*, 1995, **202**, 206-217.

45. R. Vassen, X. Cao, F. Tietz, D. Basu and D. Stover, *J. Am. Ceram. Soc.*, 2000, **83**, 2023-2028.

46. Y. Ji, Y. Zhang and C. Y. Wang, *J. Electrochem. Soc.*, 2013, **160**, A636-A649.

47. L. J. Bonderer, P. W. Chen, P. Kocher and L. J. Gauckler, *J. Am. Ceram. Soc.*, 2010, **93**, 3624-3631.

48. Y. Liu, Z.-F. Zhang, J. Halloran and R. M. Laine, *J. Am. Ceram. Soc.*, 1998, **81**, 629-645.

Chapter 7

Key variables dictating the densification of cubic-LLZO, and processing Ga:LLZO free standing thin films

7.1. Introduction

Pursuit of all-solid-state Li batteries that offer overall performance equal to or superior to current commercial batteries, especially with respect to safety, remains an important research objective.[1,2] Ceramic electrolytes that possess ionic conductivities similar to liquid counterparts yet with wider electrochemical and thermal stability windows are key to realizing such batteries.[3,4] Decades of study on doping and processing of ceramic electrolytes to identify Li^+ conduction channels and mechanisms provides target ceramic electrolytes for further study.[3,5] At present, cubic-$Li_7La_3Zr_2O_{12}$ (c-LLZO) is of utmost interest as it satisfies multiple performance metrics and also offers chemical stability to Li metal,[3,6] an optimal anode material for its high theoretical capacity (3860 mAh g^{-1}).[7] Although recent reports suggest c-LLZO suffers electrochemical instability to Li as the result of Li dendrite propagation during cycling,[8,9] critical current densities can be improved by interface conditioning,[10] surface microstructural control,[11] or in-situ intermediate anode alloy layer formation.[12,13] Efforts are made to further understand and engineer c-LLZO/Li interfacial properties to raise permissible current densities to practical levels.

At a component level, the compositions and microstructures of c-LLZO with optimal electrochemical properties are well identified.[3] Al^{3+}, Ga^{3+}, Nb^{5+} and Ta^{5+} are commonly used high ionic conductivity cubic phase stabilizing dopants that provide ambient conductivities of 0.2-1.3 mS cm^{-1} when sintered to high densities (≥ 94 %).[3,14] In contrast, un-doped LLZO presents a tetragonal crystal structure with ionic conductivities of 10^{-3} mS cm^{-1}.[3] Supervalent cations at selected concentrations are introduced to generate Li^+ vacancies which dramatically enhance ion conducting properties by promoting ion hopping.[15,16] Critical vacancy concentration of 0.5 has been determined, where t-LLZO is fully converted to c-LLZO.[17] From a microstructural perspective, higher relative densities provide higher ionic conductivities,[18] and small grains (20-40 μm) appear to offer improved cycling performance as well as lower c-LLZO/Li interfacial resistance compared to large grains (100-200 μm).[11] This has been ascribed to distribution of Li^+ current along the LLZO grain boundaries at the c-LLZO/Li interface.[11]

As addressed in recent review articles, the next phase of study should focus on processing LLZO in the correct form factor, films < 40 μm, while replicating bulk form properties, using a low-cost mass-producible method.[1,2,19] To date, achieving high density c-LLZO at such fine thicknesses has been deemed extremely difficult. Typical LLZO sintering conditions involve heating powder compacts to temperatures > 1100 °C for 10-40 h.[20,21] Ga^{3+} doped LLZO reaches high densities at shorter sintering times of 5-8 h as $LiGaO_2$ promotes sintering.[22,23] At this temperature, Li_2O volatilizes rapidly, and thus samples must be covered in the same powder to mitigate evaporation.[21,24] Yet, even the properties of the cover powder affect the final microstructure, complicating the process.[24] Therefore, efforts has been made to reduce sintering times or temperatures such that fractional excess Li intentionally introduced in the starting powder can balance Li_2O loss without relying on a bed of powder. Successful approaches introduce a

secondary driving force for densification; e.g. induction hot-pressing,[17,18,25] field assisted[26] or spark plasma sintering.[27] Sintering times are shortened to ≤ 1h at 1000-1100 °C. However, these methods are cost prohibitive for mass-production and as yet no examples of thin film formability have been forthcoming.

The majority of published sintering studies are limited to mm thick pellets whereas thin film processing work is scarce. The higher surface/volume ratios of thin films increase Li_2O loss rates, posing additional challenges.[28,29] For example, sol-gel coating efforts to produce LLZO thin films resulted in low ionic conductivities (10^{-3} mS cm^{-1}) due to low relative densities and crystallinity imposed by the need to use sintering temperatures (≤ 900 °C) that restricted Li_2O loss.[29,30] Hence, a novel processing route that leads to consistent sintered bodies at fine thicknesses must still be developed.

As discussed in Chapter 6, we reported the very first examples of processing Al^{3+} doped, dense and flexible LLZO thin film membranes (< 30 μm) by pressureless sintering at 1090 °C/1 h, using flame made nanoparticles, overcoming the above listed challenges.[28] The origin of rapid densification observed in these studies requires further elucidation, as pinpointing the mechanisms extant allows one to control them to further improve processing conditions and final properties. In this chapter, flame made Al^{3+} doped LLZO powders were calcined and ball-milled using conditions similar to most commonly reported methods.[24,31,32] We monitored compositional and structural changes by TGA, DSC, XRD, BET, SEM, and dilatometry for the individual processing steps as well as on heating. Our findings are linked to a combination of events identified in the individual steps arising from these multiple different characterization methods. Using our improved understanding, Ga^{3+} doped LLZO powders were made by liquid-feed flame spray

pyrolysis and processed to free standing thin films with superior control of compositional, microstructural, and electrochemical properties.

7.2. Experimental

7.2.1. Precursor synthesis and powder production

Lithium propionate [$LiO_2CCH_2CH_3$], lanthanum isobutyrate {$La[O_2CCH(CH_3)_2]_3$}, zirconium isobutyrate {$Zr[O_2CCH(CH_3)_2]_2(OH)_2$}, and alumatrane [$Al(OCH_2CH_2)_3N$] were synthesized as described in our previous work.[28] Gallium-atrane [$Ga(OCH_2CH_2)_3N$] was synthesized by reacting gallium hydroxide [$Ga(OH)_3$, 7 g, 0.06 mole] with triethanolamine [$(HOCH_2CH_2)_3N$, 10 g, 0.07 mole] using ethylene glycol [$HOCH_2CH_2OH$, 40 ml] as a solvent in a 250 ml round bottom flask equipped with a still head at 190 °C in N_2 atmosphere. Once transparent orange liquid was obtained, most of the ethylene glycol was distilled off, and the reactor was cooled down. Gallium hydroxide was prepared by adding aqueous ammonia to aqueous solution of gallium nitrate. Lithium propionate, lanthanum isobutyrate, zirconium isobutyrate, and gallium-atrane were dissolved in ethanol at a selected molar ratio to result in $Li_{6.25}Ga_{0.25}La_3Zr_2O_{12}$ (Ga:LLZO) composition with 50 wt. % excess lithium. $Li_{6.25}Al_{0.25}La_3Zr_2O_{12}$ (Al:LLZO) with 15 wt. % excess lithium was also produced by substituting gallium-atrane with alumatrane. The precursor solution with 3 wt. % ceramic loading was aerosolized and combusted to generate nanoparticles using the liquid-feed flame spray pyrolysis (LF-FSP) apparatus.[28] Details of LF-FSP synthesis can be found in our previous work.[28,33,34]

7.2.2. Powder and film processing

As-produced Al:LLZO nanopowders were dispersed in EtOH (200 proof, Decon Labs) with 2 wt. % polyacrylic acid (M_n=2000, Sigma-Aldrich) dispersant, using an ultrasonic horn (Vibra cell

VC-505, Sonics and Materials, Inc.) at 100 W for 15 min. After 4 h of settlement to let larger particles to settle, supernatant was decanted and dried. Powders were then manually dry compacted to pellets and heated to 750 °C for 20 h. Resulting pellets were pulverized and subsequently ball-milled in 2-propanol for 40 and 80 h using 3.0 mm diameter spherical ZrO_2 beads, and then dried in air. Calcined and ball-milled powders were heated to 400, 600, and 800 °C for 1 h at a ramp rate of 10 °C min^{-1}.

As-produced Ga:LLZO nanopowders were subject to the same cleaning process of dispersion, decantation, and drying. Suspensions were formulated per Table **7.1** by adding all components to a 20 ml vial and ball-milling with 3.0 mm diameter spherical ZrO_2 beads for 12-24 h to homogenize the suspension. Suspensions were cast using a wire wound rod coater (Automatic Film Applicator-1137, Sheen Instrument, Ltd.) to result in green films with thicknesses of 45±2 μm. Dried green films were manually peeled off the Mylar substrate, cut to selected sizes, and thermo-compressed at 80-100 °C with a pressure of 50-70 Mpa for 5-10 min using a heated bench top press (Carver, Inc.) to improve packing density.

Green films of Ga:LLZO were heated to selected temperatures and dwell times in N_2 (100 ml min^{-1}), placed in between graphite foils to avoid possible contamination or reaction with common ceramic crucibles. Sintered films were subsequently heat treated to 700-800 °C for 1-4 h in O_2 to remove surface carbon deposits.

Table 7.1. Suspension formulation.

	Role	Wt. ratio
LLZO powder	Ceramic	37
Polyvinyl Butyral	Binder	3
Benzyl Butyl Phthalate	Plasticizer	3
Polyacrylic Acid	Dispersant	1
Ethanol	Solvent	28
Acetone	Solvent	28

7.2.3. Characterization

X-ray diffraction measurements were carried out using a Rigaku Rotating Anode Goniometer (Rigaku Denki., LTD.). Scans were made from 10 to 70° 2θ, using Cu Kα radiation (1.541 Å) operating at 40 kV and 100 mA. The Jade program 2010 (Materials Data, Inc.) was used for analysis.

Specific surface areas (SSAs) were obtained using a Micromeritics ASAP 2020 sorption analyser. Samples (300 mg) were degassed at 150 °C/5 h. Each analysis was run at −196 °C (77 K) with N_2. The SSAs were determined by the BET multipoint method using ten data points at relative pressures of 0.05−0.30. SSA was converted to average particle sizes (APS) using the equation APS = 6/(SSA×ρ). The net density (ρ) of the as-produced powder was approximated by rule of mixture.

Micrographs were taken using a FEI NOVA Nanolab system (FEI company). Powder samples were used as is, sintered films were fractured for imaging. All samples were sputter coated with gold using a SPI sputter coater (SPI Supplies, Inc.). For grain size measurements, sintered films were fractured and thermally etched at 930 °C for 0.2 h in N_2 prior to sputter coating. Lineal intercept method was used to calculate the average grain sizes.

Q600 simultaneous TGA/DSC (TA Instruments, Inc.) was used to observe thermal decomposition of as-produced powders and green films. Samples (15–25 mg) were loaded in alumina pans and ramped to 1000 °C at 10 °C min^{-1} under constant air flow at 60 ml min^{-1}.

Dilatometry studies were conducting using a Dilatronic II single pushrod dilatometer (Theta Industries). Linear displacement was traced by a linear variable differential transformer (LVDT). Constant heating rate experiments were conducted from room temperature to 1050 °C at a ramp

rate of 10 °C min^{-1}. Temperature was limited to 1050 °C to prevent excessive equipment damage from Li_2O volatilization.

AC impedance data were collected with broadband dielectric spectrometer (Novocontrol technologies) in a frequency range of 10 MHz to 0.1 Hz at -35 to 55 °C in increments of 10 °C. Concentric gold electrodes, 3 mm in diameter, were deposited using a SPI sputter coater on both surfaces of the films using a deposition mask. "EIS spectrum analyser" software was used for extracting total resistance. Equivalent circuit consisting of $(R_{total}Q_{total})(Q_{electrode})$ was used. R and Q denote resistance and constant phase element, respectively. SEM fracture surface images were taken to measure sample thicknesses.

Final sintered film densities were determined by Archimedes method using ethanol.

7.3. Results and Discussion

7.3.1. Interplay of particle size, ion (Li^+/H^+) exchange, and densification

Solid state reaction is commonly used to produce LLZO powders which are subsequently ball-milled to reduce average particle sizes (APSs) prior to compaction.[24,31,32] Calcination and ball-milling conditions determine the final APSs which in turn strongly affect densification behavior. In fact, Cheng et al., report an almost three fold higher densification rate with attrition milled, 1 µm LLZO particles compared to un-milled 10 µm counterparts.[24] However, it is likely that smaller particle sizes, that is, higher specific surface areas (SSAs), accelerate the protonation reaction during and/or after processing. It is common knowledge that LLZO readily reacts with H_2O, forming proton doped LLZO and LiOH, which soon converts to Li_2CO_3.[35,36] This implies ball-milling introduces more processing variables, as discussed below, in addition to reductions in

particle sizes. Reports on optimizing densification behavior and probing the role of hydration are available, yet the two aspects have never been coupled.

To simulate commonly used conditions yet access micron to sub-micron APSs, we calcined and ball-milled $Li_{6.25}Al_{0.25}La_3Zr_2O_{12}$ (Al:LLZO) nanopowders with 15 wt. % excess Li (SSA = 16 $m^2\ g^{-1}$) synthesized by liquid-feed flame spray pyrolysis (LF-FSP) method. Calcined powders (750 °C/20 h) were ball-milled in 2-propanol followed by air drying. Extended ball-milling of 40 and 80 h was selected to emphasize the degree as well as effect of protonation. Flame made nanoparticles were used because solid-state reaction derived powders generally require high-energy ball-milling to access sub-micron particles due to the higher temperatures required to calcine powders of target compositions.[3,24,31]

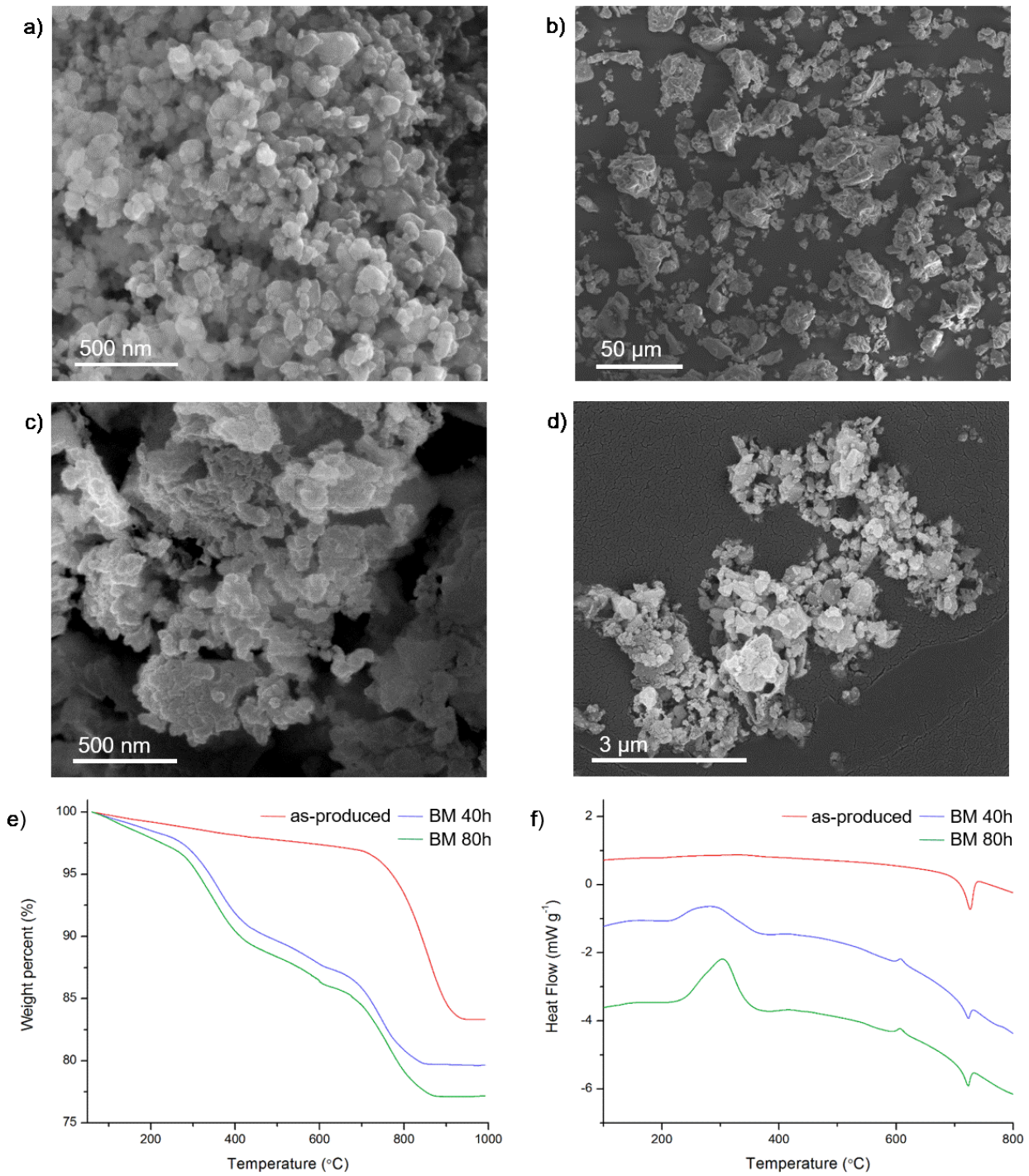

Figure 7.1. SEM of (a) LF-FSP synthesized Al:LLZO nanopowders, (b) calcined and crushed Al:LLZO powders, (c) and (d) 40 h ball-milled powders. (e) TGA and (f) DSC of as-produced and ball-milled (BM) powders. DSC curves are off-set for differentiation.

Figure **7.1** compares the morphologies, thermal stabilities and activities of the as-produced, calcined, and ball-milled Al:LLZO powders. As-produced nanopowders are a mixture of Li_2CO_3 and off-stoichiometric $La_2Zr_2O_7$ ($La_3Zr_2O_{8.5}$).[28] The rationale for producing fully decomposed LLZO is discussed just below. Calcination of these powders result in granules of 10-70 µm (Figure **7.1b**). After ball-milling, 0.5-1 µm primary particles decorated with nanoparticles < 50 nm result (Figure **7.1c** and **7.1d**). No noticeable difference between 40 and 80 h ball-milled powders were observed by SEM. The surface nano-architecture is assumed to be Li_2CO_3 as it is impossible to mill micron size oxides to nanopowders (< 100 nm) by planetary ball-milling. In support of this statement, is the observation that ion (Li^+/H^+) exchange of LLZO results in Li_2CO_3 surface coatings.[37] XRD patterns of ball-milled powders also show diffraction peaks corresponding to Li_2CO_3 (Figure **7.2b** and **7.2c**). SSAs of the 40 and 80 h ball-milled powders were 17 and 19 m^2 g^{-1}, slightly higher than for as-produced nanopowders, 16 m^2 g^{-1}. However, as evidenced in Figure **7.1a**, **7.1b**, and **7.1c**, this is likely due primarily to nanoscale surface roughness arising from Li_2CO_3 formation and does not imply smaller overall APSs.

TGAs of ball-milled powders show mass losses at temperatures below the calcination temperature, suggesting H_2O and CO_2 uptake of LLZO during processing (Figure **7.1e**). Mass loss at < 400 °C is attributed to H_2O, whereas > 400 °C is due to CO_2 evolutoin.[35,36] In addition to the Li_2CO_3 melting endotherm at 720 °C, two distinct thermal processes, exotherms at 250-350 °C and near 610 °C, are observed on heating (Figure **7.1f**). The origins of these exotherms were identified by XRD of powders heated to selected temperatures.

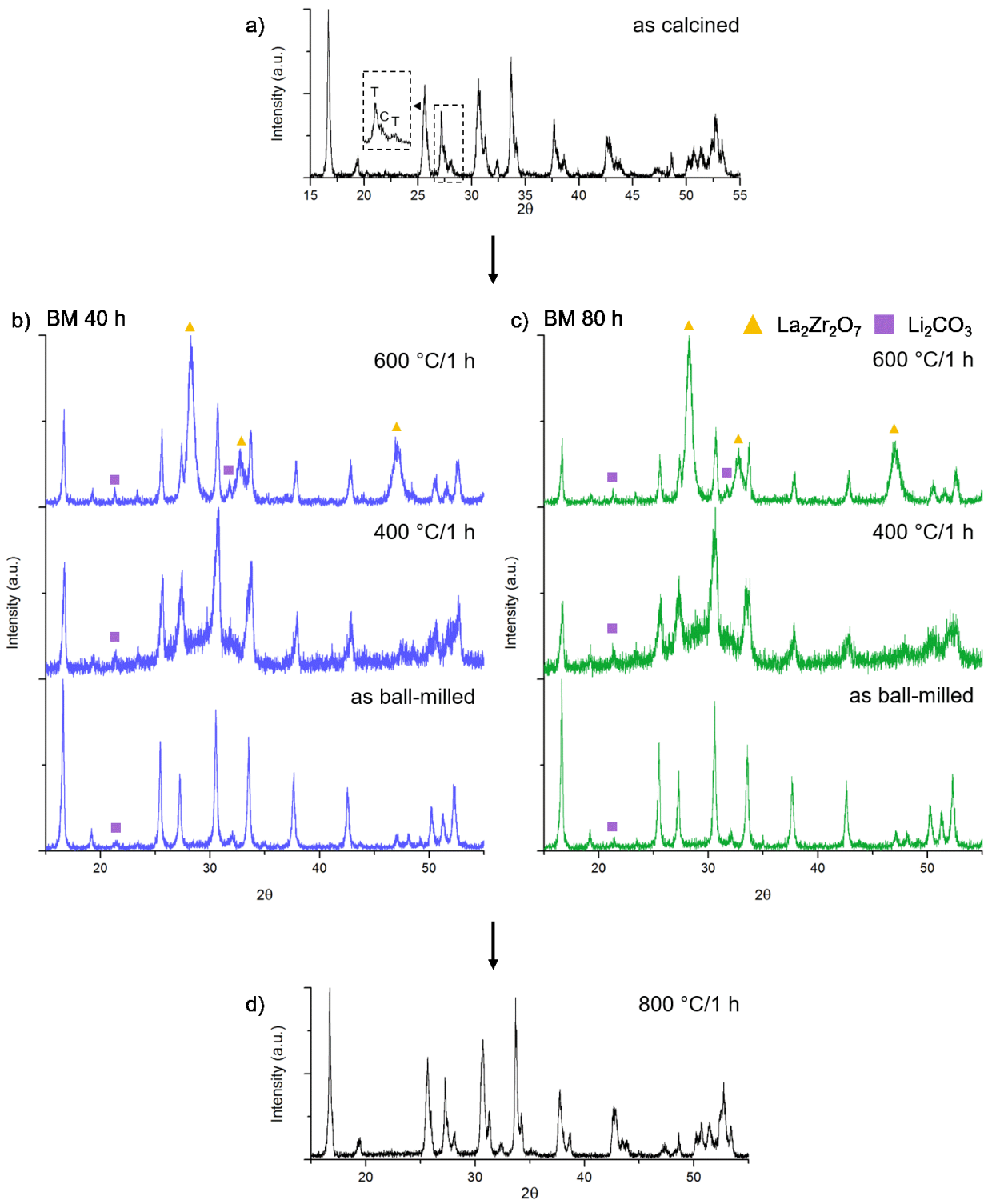

Figure 7.2. XRD patterns of the samples along the processing flow chart at selected stages. Initial and final stages show the same pattern yet intermediate temperatures show different phase fractions based on degree of protonation which leads to lattice collapse followed by crystallization. In Figure **7.2b** and **7.2c**, unlabled peaks are from c-LLZO.

Figure **7.2** shows XRDs of calcined, ball-milled, and heated Al:LLZO powders. A mixture of t-LLZO and c-LLZO are observed in the as-calcined state due to excess Li, known to stabilize t-LLZO even when c-LLZO stabilizing dopants are present (Figure **7.2a**).[25] Traces of Li_2ZrO_3 and $LaAlO_3$ intermediate phases were also present but disappear on heating to higher temperatures. On ball-milling, t-LLZO disappears and peaks corresponding to c-LLZO and Li_2CO_3 are observed (Figure **7.2b** and **7.2c**). The presence of Li_2CO_3 suggests that LiOH forms due to protonation during and/or after ball-milling. Similar results have been previously reported.[36] Compared to the highly crystalline, as ball-milled XRD patterns, an amorphous hump appears at 400 °C/1 h (Figure **7.2b** and **7.2c**). The high noise level also implies a high fraction of amorphous phase. Hence, the initial DSC exotherm is attributed to the collapse of the protonated LLZO lattices (Figure **7.1f**). This has never been reported as little attention is given to ball-milled powders heated to low temperatures as the final target of most studies is to reach high densities by sintering. Furthermore, larger particle sizes of solid state reaction derived ball-milled powders likely have less proton doped LLZO due to lower SSAs, making it difficult to notice. XRD patterns of powders heated to 600 °C/1 h show c-LLZO with broad peaks corresponding to $La_2Zr_2O_7$ (Figure **7.2b** and **7.2c**). La_2O_3 is also likely present based on the molar ratio but is unidentifiable due to peak overlap. This suggests the second DSC exotherm originates from crystallization of the amorphous phase (Figure **7.1f**). Ion exchange (Li^+/H^+) has been reported to commonly occur for Li garnets with more than three Li ions per formula unit.[38] In particular, Galven et al. also reports decomposition of protonated $Li_7La_3Sn_2O_{12}$ (LLSO) Li garnet to Li_2SnO_3, $La_2Sn_2O_7$, and La_2O_3 on heating, while no XRD data is presented.[39] In their study, decomposed mixtures are Li short compared to LLSO as the ion exchange reaction was conducted in benzoic acid/ethanol solution where Li^+ likely dissolved. On heating to 800 °C/1 h, a mixture of t-LLZO and c-LLZO is recovered (Figure **7.2d**).

Based on lower ceramic yields, stronger initial exotherm, and stronger $La_2Zr_2O_7$ relative peak intensities, 80 h ball-milled powders seem to have a higher degree of protonation (Figure **7.1e**, **7.1f**, **7.2b**, and **7.2c**). Higher SSAs also suggests more Li_2CO_3 decorates the primary particle surfaces. It can be concluded that ball-milling times, that is, APSs, dictate degree of protonation which leads to different degrees of decomposition on heating, in turn affecting densification as discussed below.

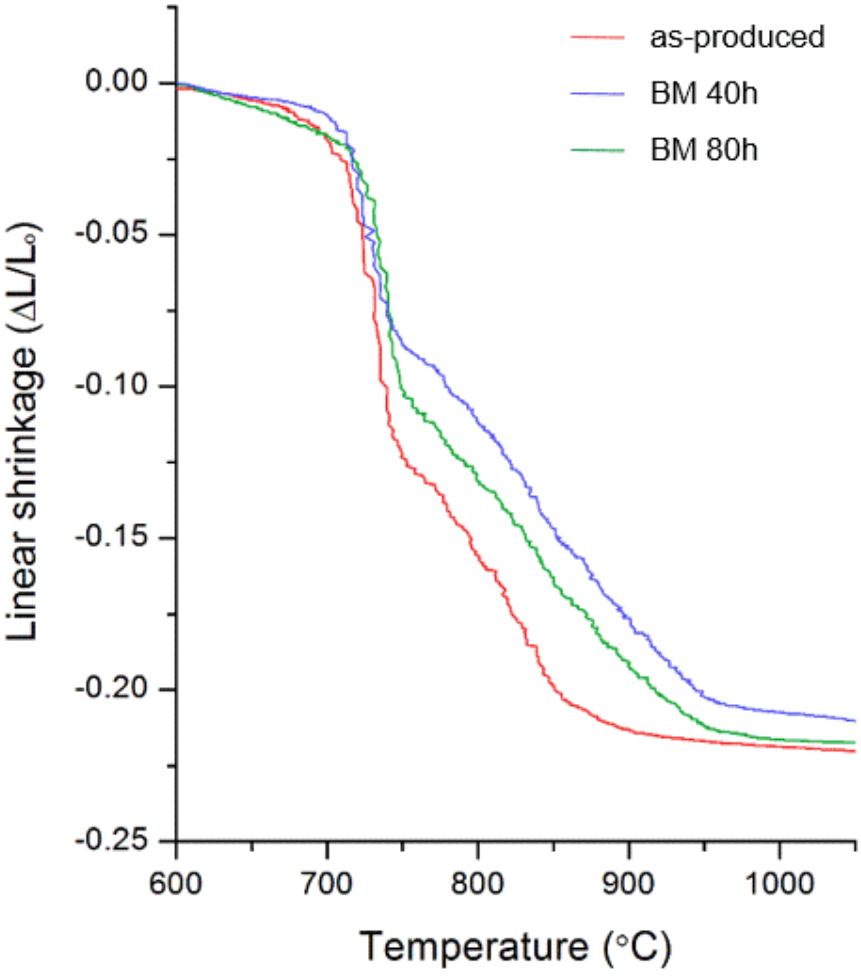

Figure 7.3. Comparison of the linear shrinkage of the as-produced and ball-milled powders. Maximum temperature was limited to 1050 °C to prevent excessive equipment damage from Li_2O volatilization.

Dilatometry studies were conducted to observe the effect of decomposition on densification behavior. Figure **7.3** compares linear shrinkages of powder compacts on heating. Densification takes place in two distinct stages in the observed temperature range. We assign the first steep linear shrinkage near the Li_2CO_3 melting point (720 °C) to liquid phase wetting the solid oxide particles thereby exerting compressive capillary force, one of the densification mechanisms prevalent in the liquid phase sintering.[40] The shrinkage rate of the first stage also indirectly supports longer ball-milling time leading to higher degrees of protonation as evidenced by greater shrinkage of the 80 h vs 40 h ball-milled powder compacts. As-produced powder shows the highest first stage shrinkage rate as it is fully decomposed, possessing the highest fraction of Li_2CO_3. The second, slower densification is likely from reaction of molten Li_2CO_3 and oxide components, gradually forming LLZO (Figure **7.2d**). Reaction driven densification is completed the fastest for the as-produced powder due to mixing at finer length scales (Figure **7.1a**). We conclude LLZO decomposition gives rise to reaction driven densification at lower temperatures which provides a superior platform for further densification of LLZO at higher temperatures.

Ion (Li^+/H^+) exchange, contrary to having negative effects on sintered LLZO,[41,42] acts advantageously in processing terms by introducing additional densification mechanisms. It appears others who performed calcination and ball-milling of LLZO powders benefitted from this phenomena without noticing.[21,24,31,43]

As a representative example, Cheng et al. also reports densification near the Li_2CO_3 melting point followed by densification of LLZO grains at higher temperatures when heating attrition milled 1 μm LLZO powder compacts using dilatometry.[24] They claim ball-milling only affected the particle sizes based on XRD. However, reaction driven densification near and slightly above the Li_2CO_3 melting point is evident in their study. The corresponding densification rate is ~5 %,

indicating lower degree of protonation, making it difficult to detect Li_2CO_3 solely by XRD due to low relative intensity ratios.

Combining the findings of Cheng et al. where they report higher sintered densities of Al:LLZO pellets at shorter sintering times when attrition milled powders were used, with results shown above as well as our recent success in pressureless sintering Al:LLZO using flame made fully decomposed LLZO nanopowders at heating schedules similar to when hot-pressed, we conclude decomposed LLZO with small APSs is an ideal starting point to minimize required external energy for reaching high densities. Therefore, aerosol combustion synthesis is well-suited for this purpose as it continuously produces fully decomposed LLZO nanoparticles.

Calcined and ball-milled powders may also lead to results similar to flame made nanoparticles when sintered. However, no further efforts were made to convert the ball-milled powders to films as excess Li content has to be adjusted to accommodate higher surface/volume ratios.[28] Furthermore, flame made nanopowders readily reach high density sintered bodies without additional intermediate processing, making calcination and ball-milling processes unnecessary.

7.3.2. Achieving thin film membranes with properties equal to bulk

First examples of continuous production of fully decomposed LLZO powders were demonstrated by Djenadic et al. using spray pyrolysis (SP) in which metal nitrate precursors dissolved in deionized water were sprayed into a hot tube (900 °C).[44] In SP, droplets undergo solvent evaporation, metal salt decomposition, and oxide formation typically producing aggregated large particles.[45,46] As-produced powders were a mixture of Li_2CO_3, $La_2Zr_2O_7$, and La_2O_3. The particles showed a broad size distribution ranging from nano to several microns with several morphologies; nano-aggregates, spheres, and broken shell, hollow spheres. The non-uniform size distribution and morphologies of the as-synthesized powders are attributed to the

non-uniformity of the initially sprayed precursor solution droplets, one of the key parameters affecting the final particle morphologies in SP synthesis.[45,46] Based on the phase composition, reaction driven densification must have taken place, yet the final densities reached were just 56 %. This can be ascribed to the poor morphological features of the starting powder interrupting uniform packing. On another note, La_2O_3 is hygroscopic, requiring storage of SP synthesized powders in a dry atmosphere.

Liquid-feed flame spray pyrolysis (LF-FSP) can be used to overcome the shortcomings found with SP derived powders. In LF-FSP, precursor droplets gasify on combustion generating a cloud of ions that subsequently undergo nucleation, growth, and quenching, resulting in un-aggregated nanoparticles of kinetic phases.[33,45] Uniform particles are obtained in LF-FSP as the precursors are gasified on combustion, and hence the aerosolized droplet size does not affect the final particle characteristics. Furthermore, La_2O_3 can be incorporated into $La_2Zr_2O_7$ phase, forming La rich pyrochlore, providing air stable starting powders. Details are discussed below.

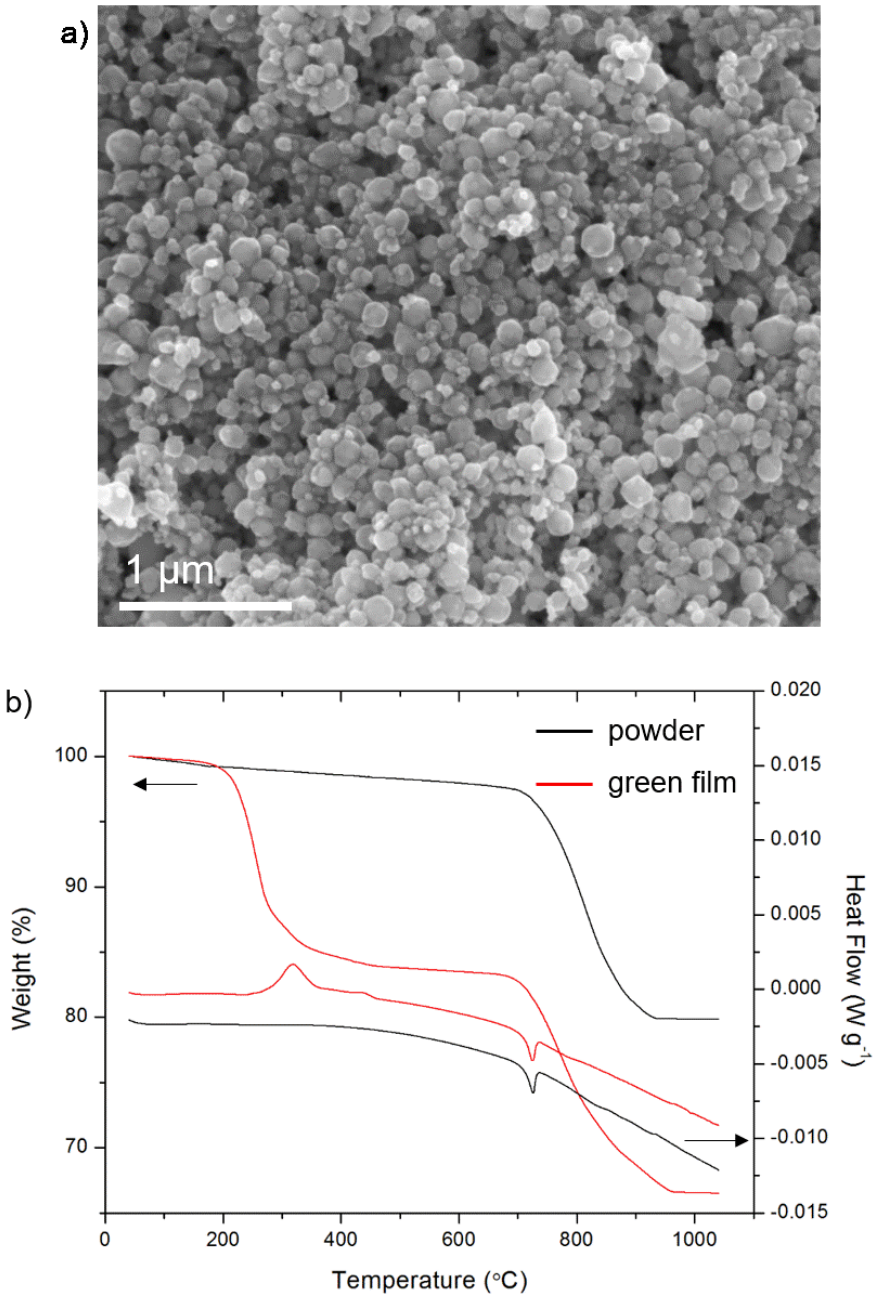

Figure 7.4. (a) SEM image of the as-produced Ga:LLZO nanopowder. (b) TGA-DSC curve of the as-produced nanopowder and green film. DSC curves are off-set for differentiation.

Figure **7.4** shows nanopowders of $Li_{6.25}Ga_{0.25}La_3Zr_2O_{12}$ (Ga:LLZO) composition with 50 wt. % excess lithium produced by LF-FSP. As-produced nanopowders show spherical morphologies with a narrow size distribution with SSAs of 15 $m^2\ g^{-1}$, corresponding to APSs ≈ 100 nm (Figure **7.4a**). XRD confirms the as-produced nanopowders are a mixture of Li_2CO_3 and off-stoichiometric

$La_2Zr_2O_7$ ($La_3Zr_2O_{8.5}$), not LLZO, due to the instability of LLZO in the LF-FSP synthesis atmosphere (Figure **7.5a-1**). Ga_2O_3 is non-detectable due to small fraction. The primary byproducts of combustion, H_2O and CO_2, coupled with high flame temperatures (>1500 °C) make formation of LLZO nanopowders unfavorable.[39] However, such materials provide excellent starting points for reasons discussed above.

The Ga^{3+} dopant stabilizes the high conductivity cubic phase and the excess lithium balances its loss during sintering. Excess lithium content is also a design parameter that may be optimized as residual excess lithium after sintering results in partial stabilization of low conductivity t-LLZO.[25] However, given that t-LLZO can be annealed to result in c-LLZO when cubic stabilizing dopants are present, no special care was given, see below.

TGA of the as-produced nanopowder shows an endotherm due to Li_2CO_3 melting (720 °C), with concomitant CO_2 mass loss as Li_2CO_3 and constituent oxides react to form LLZO. Off-stoichiometric $La_2Zr_2O_7$ phase in the composition of $La_3Zr_2O_{8.5}$ is formed, as confirmed by XRD peak shifts using α-Al_2O_3 internal standard, instead of a mixture of $La_2Zr_2O_7$ and La_2O_3, contrary to what one might expect based on the La_2O_3-ZrO_2 binary phase diagram. This is due to quenching from the high flame temperatures, resulting in kinetics phases. That is, phases normally stable only at high temperatures can be accessed with LF-FSP.[47] In comparison, in Djenadic et al.'s work, since the particle formation temperature equals that of the hot tube (900 °C), a mixture of Li_2CO_3, stoichiometric $La_2Zr_2O_7$, and La_2O_3 are formed. As a reference, the La rich $La_2Zr_2O_7$ phase is stable at temperatures above 1550 °C.[48]

In the current work, suspensions were formulated per Table **7.1**, and after 12-24 h of ball-milling they were cast onto a Mylar substrate and allowed to dry. The TGA-DSC curve of the green film shows mass loss with a corresponding exotherm at intermediate temperatures (200-

400 °C) due to oxidative removal of polymeric additives including dispersant, plasticizer, and binder (Figure **7.4b**). A Li_2CO_3 melting endotherm is noted at 720 °C with concomitant mass loss, consistent with that of as-produced powder. This suggests that there were no reactions during ball-milling and the original powder composition is maintained as the powder is fully decomposed to begin with.

Colloidal processing of ceramic powders has numerous advantages over dry compaction. First, given the green tape can be simply cut to any desired shape prior to sintering, it has excellent shape formability in any flat geometry. In comparison, shapes of the dry compacted bodies are limited to the die shape. Even slight modification of the lateral dimensions requires different dies. Second, no pressure is needed in the shape forming step for colloidal processed green bodies, whereas dry compaction requires uniaxial-pressing. Third, continuous, low cost-production is possible through a casting-sintering approach, used industrially for producing films and plates of $BaTiO_3$, ZrO_2, Al_2O_3, etc., since as early as during World War II.[49] Most importantly, agglomerates are broken down during ball-milling thereby eliminating large pores in the green body and promoting uniform particle packing, resulting in higher relative densities when sintered, compared to dry compacted counterpart.[50,51]

Despite the known benefits of colloidal processing listed above, only recently, we have demonstrated the first examples of c-LLZO film processing based on casting-sintering of flame made nanoparticles. The exceptional challenge in obtaining high density c-LLZO sintered bodies based on previously reported methods likely prohibited colloidal processing of such materials at low thicknesses.

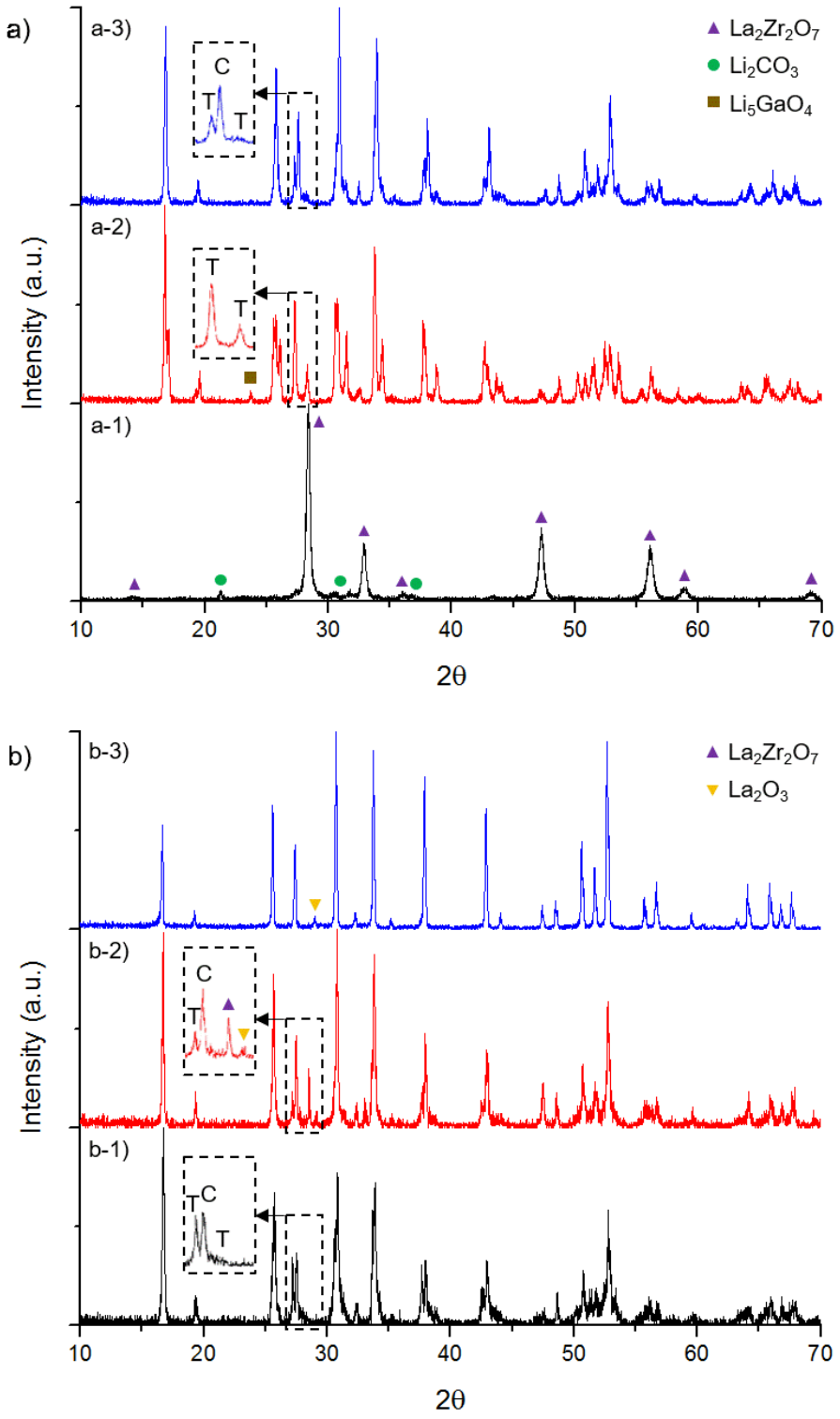

Figure 7.5. (a) XRD patterns of (a-1) as-produced Ga:LLZO nanopowders, and green films sintered to (a-2) 800 °C/1 h, and (a-3) 1000 °C/1 h. (b) XRD patterns of green films sintered to (b-1) 1130 °C/0.3 h, (b-2) 1140 °C/0.3 h, and (b-3) 1130 °C/0.3 h followed by 900 °C/2 h annealing.

Green films heated to 800 °C/1 h show t-LLZO as the main crystalline phase with traces of Li_5GaO_4 (Figure **7.5a-2**). Extra lithium filling the interstitial sites of LLZO likely distorts the crystal structure, stabilizing the tetragonal phase despite the presence of a cubic stabilizing dopant. Similar effects have been reported in Al^{3+} doped LLZO with excess Li.[25] Li_5GaO_4 also suggests the presence of excess lithium as both Li^+ and Ga^{3+} occupy the same crystallographic sites.[52] At 1000 °C/1 h, a mixture of c-LLZO and t-LLZO are present as Li_2O is partially lost (Figure **7.5a-3**). Li_2O loss has been reported at temperatures as low as 900 °C.[29] A new peak ascribed to c-LLZO in between two t-LLZO peaks as shown in the inset (27-29° 2θ) appears (Figure **7.5a-3**). The overall broad base for all peaks indicates the presence of t-LLZO as tetragonal peaks split around the cubic phase peaks on lattice distortion appearing as shoulders.

Unlike common sintering of refractory ceramics, where higher temperatures and longer duration generally result in higher relative densities, the same approach cannot be applied to LLZO sintering due to rapid Li_2O loss at high temperatures. Furthermore, densification must be complete before all excess Li is lost calling for fine control of all processing parameters. Through iterative sintering studies modifying the dwell temperatures and dwell times, we find these films to sinter to high densities at 1130 °C/0.3 h (Figure **7.5b-1**, and **7.6a**), an extremely short dwell compared to solid state reaction derived approaches (10-40 h).[3,20,21] However, XRD shows these films are a mixture of c-LLZO and t-LLZO (Figure **7.5b-1**).

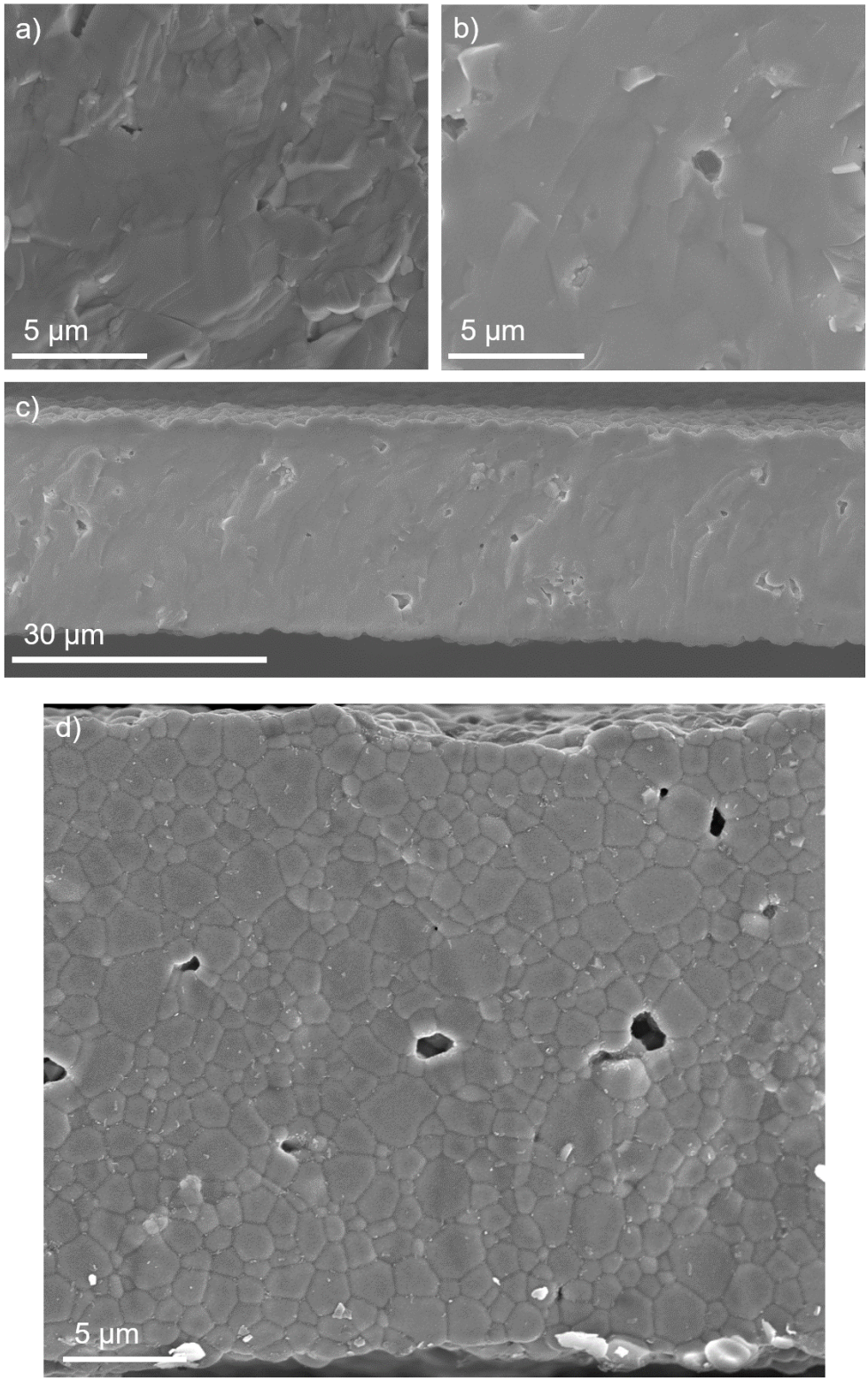

Figure 7.6. (a) SEM fracture surface image of Ga:LLZO films sintered to 1130 °C/0.3 h. (b) and (c) SEM fracture surface image of films sintered to 1130 °C/0.3 h → 900 °C/2 h. (d) Thermally etched fracture surface of films sintered to 1130 °C/0.3 h → 900 °C/2 h.

Twin boundary fringes inherent to t-LLZO are also observed in the SEM fracture surface image (Figure **7.6a**).[53] Extending the dwell time results in $La_2Zr_2O_7$ and La_2O_3 secondary phase formation (Figure **7.5b-2**). Note that t-LLZO co-exists with secondary phases when heated to 1140 °C/0.3 h, as it is odd Li deficient phases form when the Li rich phase is present (Figure **7.5b-2**). We assume the Li_2O loss at the surface is faster than re-distribution of Li^+ within the bulk. Given the former is gasification whereas the latter is diffusion within a crystalline solid, they must happen at different rates. Hence, the temperatures were lowered to < 1000 °C where the two rates could balance empirically. By annealing the 1130 °C/0.3 h sintered films at 900 °C/2 h, c-LLZO was obtained with traces of La_2O_3 (Figure **7.5b-3**). Microstructural features due to twin boundaries also disappeared (Figure **7.6b** and **7.6c**). Figure **7.6c** shows the surface smoothness and thickness uniformity of the sintered films. It appears 50 % excess Li is overkill, and processing studies of Ga:LLZO with lower excess Li content are underway. The smallest ever reported average grain sizes of 1.2±0.2 μm in the LLZO family is obtained which translates to films 20-27 grain thick, providing superior mechanical properties compared to larger AGS films (Figure **7.6d**). As a comparison Al:LLZO films in our previous work are 10-15 grains thick due to larger AGS (2.4 μm).[28] It is possible to achieve such fine, final grain sizes because we start with nanopowders.

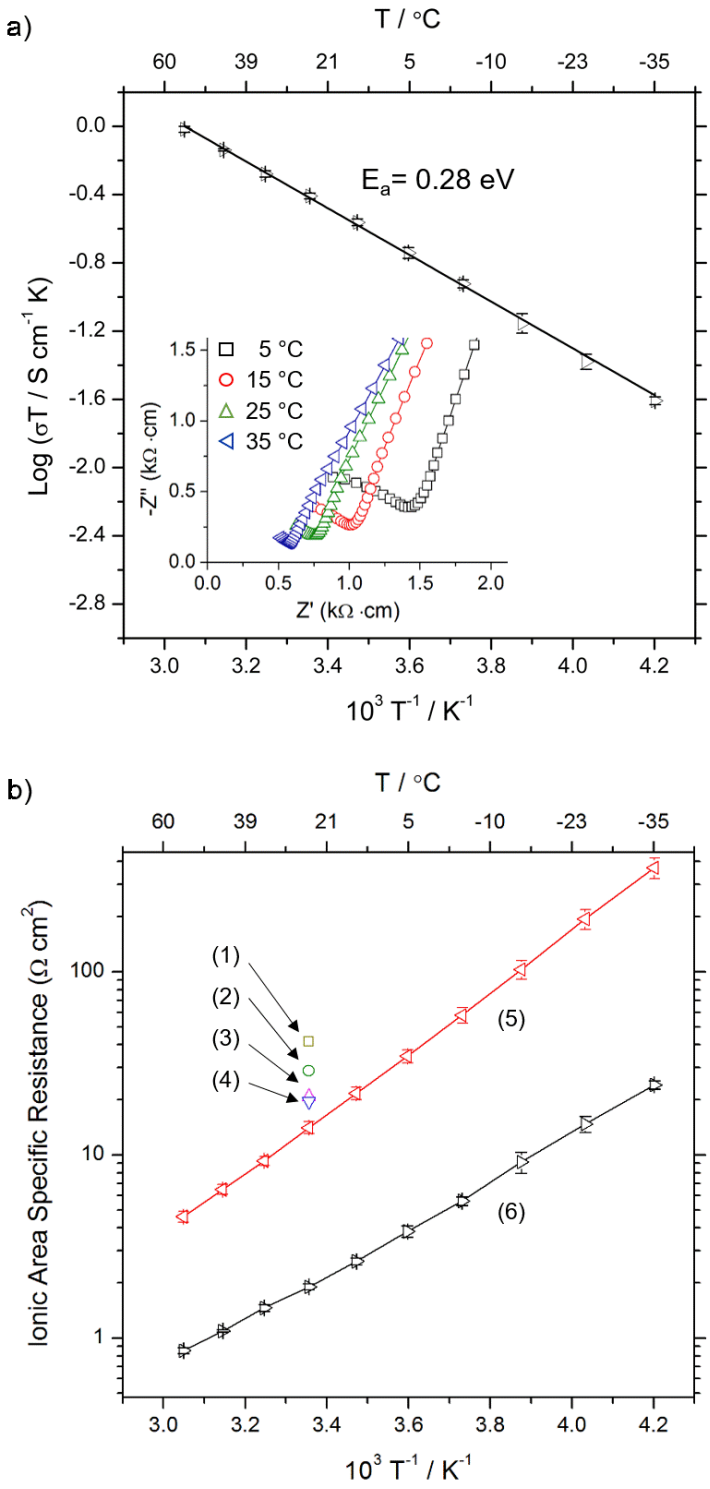

Figure 7.7. (a) Arrhenius plot of Ga:LLZO sintered to optimal conditions. Inset shows Nyquist plots at selected temperatures. Note the electrode area and sample thickness are factored in (unit : kΩ·cm) (b) Comparison of reported ionic area specific resistance of LLZO electrolytes. Detailed information of the labels are in Table **7.2**.

Table 7.2. Reported properties of LLZO membranes produced by methods suitable for mass production.

	Dopant(s)	Method	d (μm)	$\sigma_{tot.}$ (mS cm^{-1})	IASR (Ω·cm^2)	Ref.
(1)	Al^{3+}	sol-gel dip coating	1	0.0024	42	29
(2)	Al^{3+}	compact/sinter	150	0.52	29	24
(3)	Al^{3+}	sol-gel spin coating	0.39	0.0019	21	30
(4)	Al^{3+}/Ta^{5+}	compact/sinter/saw cut	200	1.02	20	54
(5)	Al^{3+}	cast/sinter	28	0.2	14	28
(6)	Ga^{3+}	cast/sinter	25	1.3	2	This work

Films sintered under optimal conditions provide Nyquist plots showing semi-circles at high frequencies and spikes at low frequencies, due to ion conduction and blocking effects, respectively (Figure **7.7a** inset). The right intercept of the semi-circle with the real axis reduces with temperature suggesting faster conduction as Li^+ diffusion is thermally activated. No secondary arc arising from grain boundary resistance is noticeable due to high relative densities and superior grain boundary contact as revealed by low porosity, trans-granular fracture surfaces (Figure **7.6b** and **7.6c**). Samples with lower relative densities with the inter-granular fracture mode have been reported to show two semi-circles arising from grain and grain boundary resistance.[28] An Arrhenius trend is found as Li^+ conduction is a diffusional process where Li^+ migrates through hopping between interstitial sites (Figure **7.7a**).[15,16] Ionic conductivities range from 0.1 to 3 mS cm^{-1} in the measured temperature span (-35 to 55 °C), with 1.3±0.1 mS cm^{-1} room temperature conductivity. Activation energy (E_a) of 0.28±0.01 eV is obtained from the Arrhenius plot, similar to what is reported for Ga^{3+} doped LLZO pellets.[23] E_a is lower compared to Al^{3+} doped LLZO films processed in our previous studies, 0.35 eV, suggesting less energy is needed for the hopping, and hence faster Li^+ conduction.

Several properties of the LLZO films produced by methods applicable to mass-production are compared in Table **7.2**. Sol-gel coating can access thicknesses ≤1 μm but suffer from low ionic

conductivities (~ 10^{-3} mS cm^{-1}) due to low relative densities and crystallinity, resulting in high ionic area specific resistance (IASR).[29,30] Low relative densities also suggest open porosities where Li dendrites can easily propagate through over cycle. Compaction derived routes generally result in high densities but are limited to high thicknesses leading to high IASR. Such samples may be diamond saw cut but still cannot access thicknesses < 40 μm.[54] IASR can be minimized by decreasing the ion conduction layer thickness and increasing the ionic conductivity (IASR = d/σ_{tot}).

Casting-sintering is the optimal selection for the low-cost, mass-production of sintered bodies with flat geometry. We demonstrate that through careful processing of flame-made nanoparticles, c-LLZO films at thicknesses < 30 μm that show same conducting properties with thick pellet counterparts can be produced, at a short sintering time and at smaller grain sizes. Record low IASR of 2 $\Omega \cdot cm^2$ is reached in this study.

Most reports regarding Li^+ conductors focus on improving ionic conductivities by selective doping to engineer the ion conduction paths, commonly conducted via sintering of powder compacts.

However, it appears the Li^+ conducting ceramics have reached or are near their maximum conductivities through numerous experimental and computational studies. Therefore, more attention should be given to reducing the sample thicknesses for practical use as a next phase.

7.4. Conclusions

In summary, we show that ion (Li^+/H^+) exchange cannot be decoupled with small particle sized LLZO, and it actually acts as an advantage in processing terms by introducing additional densification mechanisms. Reaction driven densification at intermediate temperatures (700-900 °C) as a result of Li_2CO_3 melting and its reaction with constituent oxide components provide a superior

platform for further sintering of LLZO grains at higher temperatures. Based on earlier observations and what is reported here, we conclude that fully decomposed LLZO nanoparticles are an ideal starting point in processing LLZO films. Indeed, using flame made nanopowders of fully decomposed Ga:LLZO as an example, we achieve extremely short sintering times (1130 °C/0.3 h) and low final film thicknesses (25 μm), while replicating the bulk form properties (1.3±0.1 mS cm^{-1}, 95±1% density) via simple pressureless sintering. The resulting ionic area specific resistance is the lowest ever reported in the garnet family (2 $\Omega \cdot cm^2$).

To date, LLZO sintering has been considered energy and/or equipment intensive, relying on extended sintering times (10-40 h) or specialized equipment, limiting its practical application. Here we show a paradigm shifting approach by identifying the governing densification mechanisms of LLZO, and fully utilizing those variables to minimize the external energy required for densification.

By demonstrating a facile processing route to ceramic ion conductors at fine thicknesses (< 30 μm), we overcome one of the shared major hurdles in the realization of next generation Li batteries.[1,19] These membranes not only permit assembly of all-solid-state batteries at practical level but also play a major role in realizing high energy density Li-air as well as Li-S batteries by providing a Li stable intermediate layer and by preventing parasitic reactions caused by polysulfide migration, respectively.[19,55]

References

1. B. Wu, S. Wang, W. J. Evans Iv, D. Z. Deng, J. Yang and J. Xiao, *J. Mater. Chem. A*, 2016, **4**, 17251-17259.

2. R. Chen, W. Qu, X. Guo, L. Li and F. Wu, *Mater. Horiz.*, 2016, **3**, 487-516.

3. V. Thangadurai, S. Narayanan and D. Pinzaru, *Chem. Soc. Rev.*, 2014, **43**, 4714-4727.

4. Y. Ren, K. Chen, R. Chen, T. Liu, Y. Zhang, C.-W. Nan and B. Vyas, *J. Am. Ceram. Soc.*, 2015, **98**, 3603-3623.

5. J. C. Bachman, S. Muy, A. Grimaud, H. H. Chang, N. Pour, S. F. Lux, O. Paschos, F. Maglia, S. Lupart, P. Lamp, L. Giordano and Y. Shao-Horn, *Chem. Rev.*, 2016, **116**, 140-162.

6. M. Kotobuki, K. Kanamura, Y. Sato and T. Yoshida, *J. Power Sources*, 2011, **196**, 7750-7754.

7. W. Xu, J. Wang, F. Ding, X. Chen, E. Nasybulin, Y. Zhang and J.-G. Zhang, *Energy Environ. Sci.*, 2014, **7**, 513-537.

8. R. Sudo, Y. Nakata, K. Ishiguro, M. Matsui, A. Hirano, Y. Takeda, O. Yamamoto and N. Imanishi, *Solid State Ionics*, 2014, **262**, 151-154.

9. Y. Ren, Y. Shen, Y. Lin and C.-W. Nan, *Electrochem. Commun.*, 2015, **57**, 27-30.

10. A. Sharafi, H. M. Meyer, J. Nanda, J. Wolfenstine and J. Sakamoto, *J. Power Sources*, 2016, **302**, 135-139.

11. L. Cheng, W. Chen, M. Kunz, K. Persson, N. Tamura, G. Chen and M. Doeff, *ACS Appl. Mater. Interfaces*, 2015, **7**, 2073-2081.

12. W. Luo, Y. Gong, Y. Zhu, K. K. Fu, J. Dai, S. D. Lacey, C. Wang, B. Liu, X. Han, Y. Mo, E. D. Wachsman and L. Hu, *J. Am. Chem. Soc.*, 2016, **138**, 12258-12262.

13. C. L. Tsai, V. Roddatis, C. V. Chandran, Q. Ma, S. Uhlenbruck, M. Bram, P. Heitjans and O. Guillon, *ACS Appl. Mater. Interfaces*, 2016, **8**, 10617-10626.

14. D. Rettenwander, G. Redhammer, F. Preishuber-Pflugl, L. Cheng, L. Miara, R. Wagner, A. Welzl, E. Suard, M. M. Doeff, M. Wilkening, J. Fleig and G. Amthauer, *Chem. Mater.*, 2016, **28**, 2384-2392.

15. R. Jalem, Y. Yamamoto, H. Shiiba, M. Nakayama, H. Munakata, T. Kasuga and K. Kanamura, *Chem. Mater.*, 2013, **25**, 425-430.

16. K. Meier, T. Laino and A. Curioni, *J. Phys. Chem. C*, 2014, **118**, 6668-6679.

17. T. Thompson, A. Sharafi, M. D. Johannes, A. Huq, J. L. Allen, J. Wolfenstine and J. Sakamoto, *Adv. Energy Mater.*, 2015, **5**, 1500096.

18. Y. Kim, H. Jo, J. L. Allen, H. Choe, J. Wolfenstine, J. Sakamoto and G. Pharr, *J. Am. Ceram. Soc.*, 2016, **99**, 1367-1374.

19. B. D. McCloskey, *J. Phys. Chem. Lett.*, 2015, **6**, 4581-4588.

20. R. Murugan, V. Thangadurai and W. Weppner, *Angew. Chem. Int. Ed.*, 2007, **46**, 7778-7781.

21. H. Imagawa, S. Ohta, Y. Kihira and T. Asaoka, *Solid State Ionics*, 2014, **262**, 609-612.

22. H. El Shinawi and J. Janek, *J. Power Sources*, 2013, **225**, 13-19.

23. C. Bernuy-Lopez, W. Manalastas, J. M. Lopez del Amo, A. Aguadero, F. Aguesse and J. A. Kilner, *Chem. Mater.*, 2014, **26**, 3610-3617.

24. L. Cheng, J. S. Park, H. Hou, V. Zorba, G. Chen, T. Richardson, J. Cabana, R. Russo and M. Doeff, *J. Mater. Chem. A*, 2014, **2**, 172-181.

25. E. Rangasamy, J. Wolfenstine and J. Sakamoto, *Solid State Ionics*, 2012, **206**, 28-32.

26. Y. Zhang, F. Chen, R. Tu, Q. Shen and L. Zhang, *J. Power Sources*, 2014, **268**, 960-964.

27. S.-W. Baek, J.-M. Lee, T. Y. Kim, M.-S. Song and Y. Park, *J. Power Sources*, 2014, **249**, 197-206.

28. E. Yi, W. Wang, J. Kieffer and R. M. Laine, *J. Mater. Chem. A.*, 2016, **4**, 12947-12954.

29. K. Tadanaga, H. Egawa, A. Hayashi, M. Tatsumisago, J. Mosa, M. Aparicio and A. Duran, *J. Power Sources*, 2015, **273**, 844-847.

30. R.-J. Chen, M. Huang, W.-Z. Huang, Y. Shen, Y.-H. Lin and C.-W. Nan, *J. Mater. Chem. A*, 2014, **2**, 13277.

31. N. Janani, S. Ramakumar, S. Kannan, R. Murugan and B. Dunn, *J. Am. Ceram. Soc.*, 2015, **98**, 2039-2046.

32. M. Kotobuki, H. Munakata, K. Kanamura, Y. Sato and T. Yoshida, *J. Electrochem. Soc.*, 2010, **157**, A1076-A1079.

33. C. R. Bickmore, K. F. Waldner, R. Baranwal, T. Hinklin, D. R. Treadwell and R. M. Laine, *J. Eur. Ceram. Soc.*, 1998, **18**, 287-297.

34. E. Yi, W. Wang, S. Mohanty, J. Kieffer, R. Tamaki and R. M. Laine, *J. Power Sources*, 2014, **269**, 577-588.

35. G. Larraz, A. Orera and M. L. Sanjuan, *J. Mater. Chem. A*, 2013, **1**, 11419-11428.

36. Y. Wang and L. Wei, *J. Power Sources*, 2015, **275**, 612-620.

37. L. Cheng, C. H. Wu, A. Jarry, W. Chen, Y. Ye, J. Zhu, R. Kostecki, K. Persson, J. Guo, M. Salmeron, G. Chen and M. Doeff, *ACS Appl. Mater. Interfaces*, 2015, **7**, 17649-17655.

38. C. Galven, J. Dittmer, E. Suard, F. Le Berre and M.-P. Crosnier-Lopez, *Chem. Mater.*, 2012, **24**, 3335-3345.

39. C. Galven, J.-L. Fourquet, M.-P. Crosnier-Lopez and F. o. Le Berre, *Chem. Mater.*, 2011, **23**, 1892-1900.

40. W. D. Kingery, *J. Appl. Phys.*, 1959, **30**, 301.

41. L. Cheng, E. J. Crumlin, W. Chen, R. Qiao, H. Hou, S. Franz Lux, V. Zorba, R. Russo, R. Kostecki, Z. Liu, K. Persson, W. Yang, J. Cabana, T. Richardson, G. Chen and M. Doeff, *Phys. Chem. Chem. Phys.*, 2014, **16**, 18294-18300.

42. Y. Jin and P. J. McGinn, *J. Power Sources*, 2013, **239**, 326-331.

43. Y. Ren, H. Deng, R. Chen, Y. Shen, Y. Lin and C.-W. Nan, *J. Eur. Ceram. Soc.*, 2015, **35**, 561-572.

44. R. Djenadic, M. Botros, C. Benel, O. Clemens, S. Indris, A. Choudhary, T. Bergfeldt and H. Hahn, *Solid State Ionics*, 2014, **263**, 49-56.

45. S. Li, Y. Ren, P. Biswas and S. D. Tse, *Prog. Energy Combust.*, 2016, **55**, 1-59.

46. G. L. Messing, S.-C. Zhang and G. V. Jayanthi, *J. Am. Ceram. Soc.*, 1993, **76**, 2707-2726.

47. T. R. Hinklin, J. Azurdia, M. Kim, J. C. Marchal, S. Kumar and R. M. Laine, *Adv. Mater.*, 2008, **20**, 1373-1375.

48. R. S. Roth, *J. Res. Natl. Bur. Stand.*, 1956, **56**, 17-25.

49. G. N. Howatt, R. G. Breckenridge and J. M. Brownlow, *J. Am. Ceram. Soc.*, 1947, **30**, 237-242.

50. D. Hotza and P. Greil, *Mater. Sci. Eng., A*, 1995, **202**, 206-217.

51. K. P. Plucknett, C. H. Caceres, C. Hughes and D. S. Wilkinson, *J. Am. Ceram. Soc.*, 1994, **77**, 2145-2153.

52. R. Wagner, G. J. Redhammer, D. Rettenwander, A. Senyshyn, W. Schmidt, M. Wilkening and G. Amthauer, *Chem Mater*, 2016, **28**, 1861-1871.

53. J. Wolfenstine, E. Rangasamy, J. L. Allen and J. Sakamoto, *J. Power Sources*, 2012, **208**, 193-196.

54. K. Liu and C.-A. Wang, *Electrochem. Commun.*, 2014, **48**, 147-150.

55. X. B. Zhu, T. S. Zhao, Z. H. Wei, P. Tan and G. Zhao, *Energy Environ. Sci.*, 2015, **8**, 2782-2790.

Chapter 8

Conclusions and future work

8.1. Nanocomposite wound capacitors

In Chapter 4, the feasibility of fabricating wound nanocomposite capacitors is demonstrated. The advantages of nanocomposites compared to commercial, neat polymer capacitors, as well as the wound configuration instead of a flat geometry are validated. Several approaches can be taken to further improve the overall capacitance of the wound nanocomposite capacitors.

The net dielectric constant of the nanocomposites will increase if powders stay well dispersed at higher solids loadings. This can be done by using suitable surface modifiers or dispersants such as phosphonic acid ligands[1] and trialkoxysilanes.[2] Furthermore, the solvent system can be changed to improve dispersion of nanopowders. Solvents other than ethanol, such as acetone, propanol, toluene, or mixtures of such can be tested for dispersion.

The nanocomposite layer or Al foil thicknesses can be reduced to increase energy/powder densities. As discussed in Chapter 4, capacitance is inversely proportional to the dielectric layer thickness. Also, by decreasing the volume fraction of passive components, such as Al foil (electrodes), energy/power stored per unit volume will increase.

Finally, the cast films may be thermo-compressed to reduce the thicknesses of the dielectric and electrode layers. In Chapters 6 and 7, thermo-compression of the green films resulted in 20-30 % thickness reduction. Similar effects are expected to take place with the nanocomposites.

Voids within the composite layers are likely reduced or removed during the process which will improve the overall performance.

8.2. Li^+ conducting oxide membranes

Chapters 5-7 explore a novel processing route that leads to free-standing, flexible, thin film Li^+ conducting membranes (20-50 μm). Flame made NPs provide a processing short-cut as well as access to sintered films with thicknesses not easily obtained by other methods when micron size powders are used. One of the challenges in realizing all-solid-state batteries is resolved through these studies. The next phase in this research topic includes further optimization of Li^+ conducting oxides, bonding of active components (cathode and anode materials) to complete a working cell, and reducing interfacial resistance between active components and electrolyte as further discussed below.

To maximize the energy/powder densities for a given cell, volume/mass occupied by the passive components, such as the electrolyte must be minimized. Hence, electrolyte thicknesses < 10 μm should be targeted with further processing studies, monitoring densification and Li_2O loss. Sintering aids may be added and heating schedules further optimized to target single phase, fully dense films with thicknesses < 10 μm. Micron to submicron AGSs are likely required for such films to allow easy handling.

To complete a working cell, anode and cathode layers must be bonded on each side of the electrolyte. Compared to conventional Li batteries using liquid electrolytes where high quality liquid-solid interfaces are easily obtained, it has proven difficult to process solid-solid interfaces with each solid maintaining their respective properties, resulting in high interfacial resistance and rapid capacity fade during cycling.[3-6] Cathode layers have been cast/deposited onto electrolyte

(pellets) surfaces and subsequently heated to 700-900 °C where reaction byproducts form, interrupting electrochemical reactions when cycled. For example, La_2CoO_4 reaction layer has been reported for LLZO/$LiCoO_2$ pair due to cross-diffusion while processing.[6] Less attention is given to LLZO/$LiFePO_4$ and LLZO/$LiMn_2O_4$ pairs as they react at temperatures as low as 500-600 °C where original phases no longer exist and only reaction byproducts such as Li_3PO_4, $La_2Zr_2O_7$, $Li_2Mn_2O_3$ and etc. remain.[5] It is likely that an interface layer forms for any given electrolyte/active material pair, such that the focus should be on identifying pairs or processing routes, including interfacial coatings, that lead to electrochemically active interfaces with minimal performance loss. The interface integrity can be analyzed via in-situ microscopic characterization,[7] or by analyzing sintered bulk batteries by electrochemical testing.[8] For example, Nb and Al_2O_3 coatings on LLZO have been reported to greatly reduce the interfacial resistances of LLZO/$LiCoO_2$ and LLZO/Li metal, respectively.[9,10] However, the coatings were applied by pulsed laser and atomic layer depositions in these studies. Hence, exploring easily scalable, low cost coating methods based on wet chemistries (e.g. sol-gel coating) would be of great interest as well.

8.3. General directions

The rising price and fairly fixed production rate of Li mandates development of alternative energy storage devices such as Mg and Na batteries.[11] Solid electrolytes for these systems, such as $Mg_{0.5}Zr_2(PO_4)_3$, β''-Al_2O_3, or $Na_3Zr_2Si_2PO_{12}$, can be processed into free standing, dense, flexible thin films starting from flame made nanopowders. Sintering behavior, ionic conductivities, AGSs and etc. can be compared with other studies using micron size powders.

β''-Al_2O_3, in particular, has been produced in the Laine group in the past, but was limited to pellet sintering studies.[12] Compared to well established Na^+ conductors which have a long history,

reports on Mg conducting oxides are rare, mandating a series of compositional doping studies to identify a high ionic conductivity composition. For example, Nb^{5+}/Y^{3+} doping on Zr^{4+} sites of $Mg_{0.5}Zr_2(PO_4)_3$ can be explored to analyze the effects on sintering, lattice constants, ionic conductivities, and etc.

Either Li, Mg, or Na batteries, the focus will gradually shift from component (individual material) to system level (battery) as the research progresses. Hence, collaboration with research groups well equipped with battery testing equipment must be established to characterize and understand the effects of electrolyte/active material pairings and interfacial coatings on the overall performance. Thermodynamic and electrochemical stabilities of cathode/electrolyte and anode/electrolyte interfaces with or without interfacial coatings must be thoroughly studied to construct cells with superior capacity, capacity retention, energy density, and etc.

The thin film processing of flame made nanopowders can be extended to other functional thin films. For instance, luminescent thin films can be processed by doping rare earth (RE) elements to $Y_3Al_5O_{12}$ (YAG). Advantages of reactive sintering Y_2O_3 and Al_2O_3 nanopowders to produce YAG tubes has been demonstrated in the Laine group.[13] RE doping studies can be a continuation of the research topic, by reactive sintering RE, Al_2O_3, and Y_2O_3 to produce RE doped YAG. Selection and concentration of RE in YAG host can be changed to monitor their effects on the optical properties. For example, Ce doped YAG produces white light, in combination with blue LED.[14] Figure **8.1** presents preliminary results of Ce:YAG thin film sintering studies.

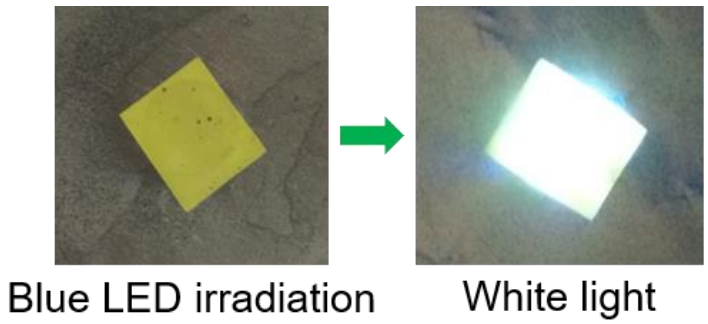

Figure 8.1. Illuminating sintered $Ce_{0.05}Y_{2.95}Al_5O_{12}$ thin film with blue LED produces white light.

Transparent electron conducting films can also be produced by selected heat treatments of sintered $12CaO{\cdot}7Al_2O_3$ (C12A7) films.[15,16] Heat treating (1300 °C/2-12 h) the sintered films in H_2 followed by UV irradiation,[15] or in reducing atmosphere (carbon crucible)[16,17] converts C12A7 from insulators to conductors by generating color center defects, resulting in RT electrical conductivities of 0.3-1500 S cm^{-1}. Figure **8.2** shows preliminary results of C12A7 thin film sintering studies.

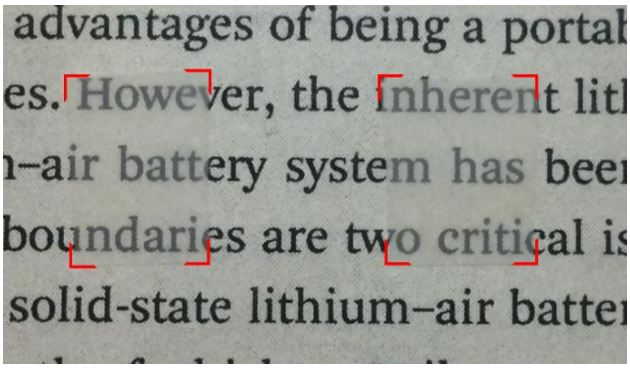
advantages of being a portal
es. However, the inherent lith
n–air battery system has beer
boundaries are two critical is
solid-state lithium–air batter

Figure 8.2. Sintered, transparent C12A7 films.

References

1. P. Kim, S. C. Jones, P. J. Hotchkiss, J. N. Haddock, B. Kippelen, S. R. Marder and J. W. Perry, *Adv. Mater.*, 2007, **19**, 1001-1005.

2. S. Ramesh, B. A. Shutzberg, C. C. Huang, J. Gao and E. P. Giannelis, *IEEE Trans. Adv. Packaging*., 2003, **26**, 17-24.

3. V. Thangadurai and W. Weppner, *J. Power Sources*, 2005, **142**, 339-344.

4. K. Park, B.-C. Yu, J.-W. Jung, Y. Li, W. Zhou, H. Gao, S. Son and J. B. Goodneough, *Chem. Mater*., 2016, **28**, 8051-8059.

5. Y. Ren, T. Liu, Y. Shen, Y. Lin, C.-W. Nan, *J. Materiomics*, 2016, **2**, 256-264.

6. K. H. Kim, Y. Iriyama, K. Yamamoto, S. Kumazaki, T. Asaka, K. Tanabe, C. A. J. Fisher, T. Hirayama, R. Murugan and Z. Ogumi, *J. Power Sources*, 2011, **196**, 764-767.

7. C. Ma, Y. Chen, K. Yin, J. Luo, A. Sharafi, J. Sakamoto, J. Li, K. L. More, N. J. Dudney and M. Chi, *Nano. Lett*., 2016, **16**, 7030-7036.

8. S. Ohta, T. Kobayahi, J. Seki and T. Asaoka, *J. Power Sources*, 2012, **202**, 332-335.

9. T. Kato, T. Hamanaka, K. Yamamoto, T. Hirayama, F. Sagane, M. Motoyama and Y. Iriyama, *J. Power Sources*, 2014, **260**, 292-298.

10. X. Han, Y. Gong, K. Fu, X. He, G. T. Hitz, J. Dai, A. Pearse, B. Liu, H. Wang, G. Rubloff, Y. Mo, V. Thangadurai, E. D. Wachsman and L. Hu, *Nat. Mater*, 2016

11. A. Yaksic and J. E. Tilton, *Resour. Policy*, 2009, **34**, 185-194.

12. A. C. Sutorik, S. S. Neo, D. R. Treadwell and R. M. Laine, *J. Am. Ceram. Soc*., 1998, **81**, 1477-1486.

13. N. J. Taylor and R. M. Laine, *Adv. Funct. Mater*., 2014, **24**, 1125-1132.

14. S. Nishiura, S. Tanabe, K. Fujioka and Y. Fujimoto, *Opt. Mater*., 2011, **33**, 688-691.

15. K. Hayashi, S. Matsuishi, T. Kamiya, M. Hirano and H. Hosono, *Nature*, 2002, **419**, 462-465.

16. S.-W. Kim, K. Hayashi, M. Hirano and H. Hosono, J. Am. Ceram. Soc., 2006, 89, 3294-3298.

17. H. Hosono, S. W. Kim, M. Miyakawa, S. Matsuishi and T. Kamiya, J. Non-Cryst. Solids, 2008, 354, 2772-2776.